Imperfect Fabry-Perot resonators

Klaassen, T.

Citation

Klaassen, T. (2006, November 23). *Imperfect Fabry-Perot resonators. Casimir PhD Series*. Retrieved from https://hdl.handle.net/1887/4988

Imperfect Fabry-Perot resonators

Thijs Klaassen

Imperfect Fabry-Perot resonators

PROEFSCHRIFT

ter verkrijging van
de graad van Doctor aan de Universiteit Leiden,
op gezag van de Rector Magnificus Dr. D. D. Breimer,
hoogleraar in de faculteit der Wiskunde en
Natuurwetenschappen en die der Geneeskunde,
volgens besluit van het College voor Promoties
te verdedigen op donderdag 23 november 2006
klokke 16.15 uur

door

Thijs Klaassen

geboren te Grave
op 3 mei 1978

Promotiecommissie:

Promotor:	Prof. dr. J. P. Woerdman	
Copromotor:	Dr. M. P. van Exter	
Referent:	Prof. dr. ir. J.J.M. Braat	(TU Delft/Philips Research)
Leden:	Prof. dr. G. Nienhuis	
	Prof. dr. G. W. 't Hooft	(Universiteit Leiden/Philips Research)
	Prof. dr. P. H. Kes	
	Prof. dr. W. M. G. Ubachs	(Vrije Universiteit Amsterdam)
	Prof. dr. H. P. Urbach	(TU Delft/Philips Research)
	Dr. E. R. Eliel	

Aan mijn ouders en broer(tje)

Vers twee

Bij herlezing klinkt het als
een postcoïtaal gevoel van droefenis
tohoe wa bohoe, tohoe wa bohoe

Als je het hardop herhaalt
zie je landschappen zich ontvouwen
een novemberse zandplaat in de Waddenzee
de desolate vlaktes ten zuidoosten van Glen Coe
en ga je turf ruiken, leisteen
twee adelende hazen in de schuur

Vijf loeizware lettergrepen
met meer gewicht dan alle elementen tezamen
tohoe wa bohoe, de aarde woest en ledig
in de Hebreeuwse tekst van Genesis een vers twee

Wat ze moeten aanduiden is onvoorstelbaar
het begin voor het begin, een toestand zo oer
dat mijn buitenwijkverbeelding slechts
tekortschietende vergelijkingen voorhanden heeft

Ook Hollywoodiaanse aardbevingen
vloedgolven, orkanen en vulkaanuitbarstingen
moeten peanuts zijn vergeleken met de horror van toen

Misschien is de plotse stuiptrekking die
vlak voor je in slaap valt door je lichaam schrikt
een verre naschok van dat oorspronkelijke geweld

Een stuip die zegt:
er is slaap, er zijn dromen
loom drijvende, onder water wiegende
maar gedragen worden wij door geen grond

Contents

CHAPTER 1

Introduction

In 1899, the first Fabry-Perot interferometer (or resonator) was built by Fabry and Perot [1] by placing two planar mirrors parallel to each other. Be it more than 100 years old, it nevertheless presents a challenging topic in the optics course, comprising a number of interesting facets, like the theory of multiple interferences (first analyzed by Airy in 1831) and the presence of circular fringes (first observed by Haidinger in 1855). The high spectral resolution that can be achieved with a Fabry-Perot makes it essential for many (modern) applications; like lasers, laser gyroscopes (more than two mirrors needed), and cavity ring-down spectroscopy [2, 3]. The Fabry-Perot also forms the heart of many state-of-the-art experiments; in cavity QED [4], in experiments with micro-resonators [5, 6], in gravitational wave detectors [7–9], and in even more exotic experiments aimed at superimposing two quantum states of a macroscopic mirror [10]. The first Fabry-Perot interferometers were composed of two planar mirrors; later designs often use two spherical mirrors.

A Fabry-Perot interferometer can be operated in both the angular and spectral domain. In the angular domain, a pattern of "fringes of equal inclination", or so-called Haidinger-fringes, is observed behind a planar Fabry-Perot that is illuminated with a wide-angle beam at a fixed wavelength; fringes formed by illumination with a slightly different wavelength are observed under a slightly different angle. In the spectral domain, different wavelengths show resonances in the spectrum at different cavity lengths, while scanning the cavity length over at least half a wavelength.

The width of a fringe dictates the resolution of a Fabry-Perot and is determined by the cavity finesse $F = \Delta\nu_{\text{FSR}}/\Delta\nu$, where $\Delta\nu_{\text{FSR}}$ is the free spectral range or separation of adjacent maxima and $\Delta\nu$ the width (FWHM) of the individual fringes. Ignoring diffraction, the finesse of a resonator, comprising ideal and lossless mirrors is determined by the reflectivity of the mirrors only. The finesse of practical planar Fabry-Perot resonators, however, is often limited by the losses introduced by both diffraction [11, 12] and mirror imperfections, *e.g.*, surface

roughness and aberrations. Diffraction losses in a planar Fabry-Perot can be neglected for short cavities or wide-beam illumination. In planar cavities with wide-beam illumination, imperfections that introduce a height variation of λ/m over the full mirror aperture, limit the finesse to $F \sim m/2$ [1, 11, 13, 14]. In practice, this means that even for state-of-the-art substrates with a 0.1 nm (RMS) roughness, the finesse of a planar Fabry-Perot is limited to only $F = 5400$ for a wavelength of $\lambda = 1064$ nm [15] and even less for visible wavelengths. This is a real drawback in many applications.

Stable resonators with *spherical* mirrors (first proposed in 1956) are much less affected by these limitations and can achieve a much higher finesse, up to $F = 1 \times 10^6$ [16]. For completeness we note that unstable resonators, which also comprise spherical mirrors, are lossy by their geometry and can never achieve a high finesse. The spherical shape of the mirrors (in a stable resonator) compensates for diffraction [17] and the resonator is less sensitive to spatially extended imperfections as the modes on the mirrors are more compact. For resonators with state-of-the-art spherical mirrors, the finesse is eventually limited (if not by transmission of the mirrors) by the power loss per round-trip due to the area-integrated roughness-induced scatter. This so-called total integrated scatter (TIS) of the resonator scales inversely with m^2 [18], so that the finesse scales as m^2. This is obviously a significantly more relaxed requirement than that for a planar cavity, where the finesse scales linearly with m. Another advantage that favors spherical resonators over planar ones is that spherical mirrors can be manufactured more precisely than planar ones.

Just as their planar counterpart, resonators comprising spherical mirrors can be operated in both the angular and the spectral domain. Again, fringes appear for illumination with a wide beam, addressing many transverse modes in the cavity. Spherical aberration of the mirrors makes a description of the fringes more complicated than for a planar resonator [19] and reduces the finesse for the higher-order fringes [20]. The "quadratic" influence of imperfections is also observed for a resonator with spherical mirrors operated in the spectral domain.

The initial goal of this Thesis was to demonstrate chaos in an open two-mirror resonator. Two requirements have to be fulfilled to obtain chaos within the context of geometrical (*i.e.* ray) optics. Firstly, exponential sensitivity of the evolution of the intra-cavity ray to the initial conditions is required, and, secondly, the ray has to remain confined inside the resonator for a sufficient time to produce mixing. We have designed a bifocal mirror that, in combination with a conventional concave mirror, forms a resonator with an unstable inner and a stable outer part ("inner" and "outer" refer here to the transverse coordinate). The unstable part provides for the exponential sensitivity, whereas the stable part provides for the mixing. We note that although the resonator comprises an unstable part, the resonator is stable in an overall sense. In order to achieve chaos in this overall stable cavity, we need, as mentioned above, a long residence time of the light in the cavity. This implies that the finesse must be as large as possible and thus requires a solid understanding of the imperfections of a Fabry-Perot. In fact, this has become the main theme of this thesis.

Another motivation for a thorough understanding of imperfections is that the unstable part of the bifocal resonator acts as a sort of "macro"-imperfection and produces, in combination with the stable part, a challenging and complex physical system. For full appreciation and understanding of this system, it is necessary to be able to distinguish phenomena unique for this configuration from effects also present in conventional resonators, comprising two

standard spherical mirrors. We decided to investigate first the effect of imperfect mirrors, *i.e.*, roughness-induced scattering and aberrations, on the performance of a conventional stable resonator. By aberrations, we mean the deviation of the actual wavefront from the spherical reference wavefront; these deviations may be caused by a combination of the spherical shape of the mirror and the nonparaxial transverse excursion of the ray through the resonator.

A central and important theme in our analysis is the concept of frequency-degeneracy (first introduced by Herriot [21] in 1964), where the ray and wave description of light in a resonator are intimately linked. In the ray picture, frequency-degeneracy means that a ray retraces itself after an integer number of N round-trips through the cavity. In the wave picture, frequency-degeneracy imposes that resonances in the spectrum overlap in N clumps of modes within a free spectral range.

The contents of this Thesis is organized as follows:
In Chapter 2, we characterize the roughness-induced scattering of a single mirror by means of its angular distribution (BRDF) and total scattered power (TIS). We also describe the effect of scattering on the performance of a conventional resonator, comprising two mirrors. We demonstrate and discuss how the losses affect the cavity finesse, measured in both time and spectral domain, as well as the average power throughput.

In Chapter 3, scattering is shown to produce mode coupling close to frequency-degenerate points. This effect has drastic consequences which are analyzed in the spatial, spectral, and time domain. A numerical simulation helps us to quantify the number of coupled modes. The effect of mode beating on cavity ring-down is pointed out as well.

In Chapter 4, a scanning cavity is injected on-axis with a compact ("pencil") beam. Although we inject locally, fringes appear over the concave mirror aperture, at least close to frequency-degenerate points. We claim that these fringe are caused by light scattered out of the on-axis beam into resonant orbits. In our resonator, spectral and spatial properties are intimately linked and cannot be separated. We demonstrate how an analysis of the observed fringe pattern yields a method to accurately determine aberrations.

In Chapter 5, we measure the deviations from paraxiality in a folded 3-mirror resonator, a result from earlier attempts to show chaos in an open resonator. We quantify this by accurately measuring the Gouy phase of subsequent higher-order modes around frequency-degeneracy. The experimental results are supported by a ray-tracing simulation.

In Chapter 6, a connection is established between a wave and ray description of aberrations, used in Chapter 4 and 5. The connection is based on Fermat's principle in a frequency-degenerate resonator. We derive and compare the cavity length reductions needed to maintain frequency-degeneracy for higher-order modes or, equivalently, larger transverse displacements.

In Chapter 7, we report on mirrors that are not fabricated by traditional grinding and polishing, but by diamond-machining. The diamond chisel makes circular grooves on the substrate, and causes a different type of scatter than the more random defects introduced in traditionally produced mirrors. We investigate the influence of this production method on the multiple interferences in the resonator and show that a reasonable finesse can still be obtained.

In Chapter 8, the eigenmodes of a resonator with one diamond-machined bifocal mirror are discussed. The central convex part of the bifocal mirror breaks the full quadratic profile of the mirror and imposes Laguerre-Gaussian eigenmodes on the resonator. The observed mode

profiles are compared with analytically calculated eigenmodes and a numerical simulation is performed to model the bifocal mirror.

In Chapter 9, we investigate the behavior of a bifocal cavity, consisting out of a stable outer and an unstable inner resonator, which is expected to show the onset of chaos. We demonstrate the coupling of two resonators based on transmission spectra and patterns, and report on the ability of the configuration to fulfill the basic requirements to obtain chaos.

Characterization of scattering in an optical resonator

Roughness-induced scattering affects the performance of a resonator. We study the scattering of a single mirror first, and compare this result with the losses of a resonator, comprising two mirrors. Besides some standard tools to characterize the losses, a new method based on the spectrally averaged transmission is introduced.

2.1   Introduction

Fabry-Perot resonators in textbooks are assumed to have ideal, lossless and perfectly smooth mirrors; however, those used in experiments are often far from ideal and have deformations on various length scales. In Bennett *et al.* [18], three regimes of deformations are defined based on the size of the roughness features (denoted between brackets): *surface roughness* (< 0.1 mm), producing light scattering, *waviness* ($0.1 - 10$ mm) contributing to the small angle scattering, and *surface figure* (> 10 mm) or deviations from the ideal geometrical shape, deforming the modes in the resonator. All three types of roughness can drastically affect the behavior of the resonator dynamics as will be pointed out in the following Chapters of this thesis. In this Chapter, we will focus on scatter. In Chapter 4, 5, and 6 we will consider surface figure.

The surface quality of mirrors is of crucial importance in a field like cavity QED [4] and applications such as ring-laser gyroscopes and gravitational wave detectors, like LIGO [7], VIRGO [8] and TAMA [9]. For all these fields and applications, the roughness-induced scatter limits the ultimate performance. Specifically, in cavity QED-experiments the coupling between field and atom gets worse [22], whereas for ring-laser gyroscopes the scatter couples the propagating and counter-propagating modes and thus lowers the sensitivity [23]. Light scattered out of the lowest order mode of a gravitational wave detector reduces the fringe contrast and thus the performance [24–27]. State-of-the-art mirrors with ditto coatings have a loss (both absorption and scatter) in the order of 10^{-6} per reflection and a surface roughness (RMS) of 0.1 nm [22, 26, 28].

In this Chapter, we will visualize and demonstrate the amount and distribution of the scatter in a resonator. The mirrors used in these experiments have a diameter of 5 cm, and a radius of curvature $R = 50$ cm. The measured transmittance of the mirror is $T = 4.1 \times 10^{-4}$ at the central reflecting wavelength of 532 nm. The substrate and multilayer coating have a very small absorption loss as compared to the scatter loss; this absorption loss will be neglected (see *e.g.*, [22]). The mirrors described in this Chapter are typical for those used in most experiments of this thesis.

In Section 2.2, the losses of a single mirror are characterized, while Section 2.3 and Section 2.4 discuss the effect of loss in a two-mirror Fabry-Perot cavity. Whereas most loss-measurements performed on a Fabry-Perot are based on the observed resonance linewidth, we will show that similar information can be obtained from a new method that is based on a measurement of the spectrally-averaged transmission. This method turns out to be simple and accurate. Conceptually, the most logical way to measure the spectrally *averaged* transmission is to use *incoherent* illumination, *e.g.*, by using a LED: this measurement has been performed first. Then we demonstrate that the average transmission $\langle T(\phi) \rangle$ (ϕ is round-trip phase) of a *coherently* illuminated resonator gives identical results. Section 2.4 describes the resonator losses as found from the, widely used, finesse and cavity ring-down. We conclude with a comparison and discussion of the various methods in Section 2.5.

2.2   Single-mirror scattering

The amount and distribution of the roughness-induced scatter of a single mirror can be visualized and quantified with a setup as shown in Fig. 2.1. A CW-single-frequency-laser (IN-
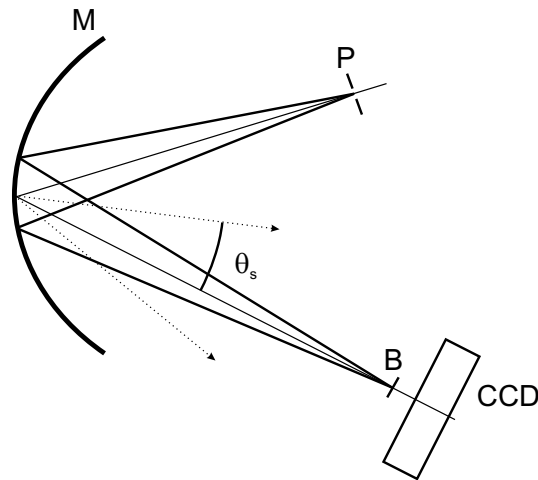
Figure 2.1: *Overview of the setup for measuring the scatter of a single mirror, M. The mirror is illuminated by light diffracted on a pinhole P. The dotted arrows indicate light scattered at the mirror under an angle θ_s. The distances between pinhole and mirror (PM) and mirror and image of the pinhole (MB) are 36 cm and 81 cm, respectively. The angle between both arms $\angle PMB$ is $12°$. The image is blocked, B, to prevent overexposure of the CCD.*

NOLIGHT Prometheus) at a wavelength $\lambda = 532$ nm illuminates a pinhole *P* with a diameter of 200 µm. The pinhole is imaged by the concave mirror under study. In the image plane of the pinhole, the image is blocked to prevent the linear CCD-camera (Apogee Alta U1) from overexposure by the on-axis beam. As the sensitive area of the CCD is only 6.9×4.1 mm^2, we use a patchwork of images on several lateral positions, to obtain the scattering profile over a larger angular range. This results in an image as shown in Fig. 2.2. The center shows the obscuration blocking the on-axis beam; the speckles in the picture result from light scattered out of the on-axis beam due to roughness on the mirror surface. The effect of scatter is clearly visible although the intensity in the central spot and the scattered light differ by $7 - 8$ orders of magnitude. The speckles in Fig. 2.2 result from interferences of the spatially-coherent contributions from different parts of the mirror. Taking a closer look at the speckles, we see the rotational symmetry of the scatter pattern. Furthermore, it turns out that all speckles have roughly the same size, but what determines this size? To answer this question we have to consider that the speckle is Fourier-related to the illuminated area on the mirror and that this area is again (inversely) Fourier related to the pinhole. This means that the speckles are in a way just scaled and randomly displaced images of the pinhole. Statistics on the size of the speckles do indeed show that the speckles have approximately the size of the pinhole scaled by the imaging-magnification.

7
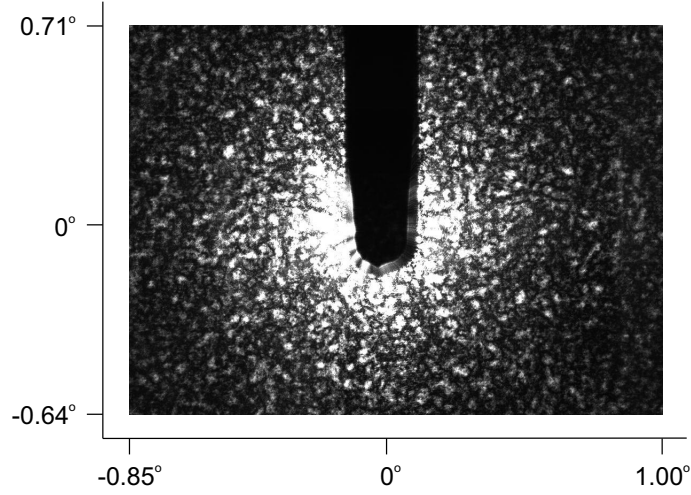
Figure 2.2: *Figure consisting out of 25 CCD images of the scatter from a single mirror. In the center an obscuration blocks the direct beam. The speckles are formed by scatter due to surface roughness of the mirror.*

The speckle pattern is not caused or influenced by edge-diffraction of the mirror as the diameter of the spot (Airy-disk) on the mirror (at $L_1 = 36$ cm away from the pinhole) is small ($1.22\lambda L_1/D \approx 2$ mm) as compared to the size of the mirror. Furthermore, the spot on the mirror is also small as compared to the relevant dimensions of Fig. 2.2, so we can neglect the finite size of the illuminated area and treat it approximately as a point scatterer in our analysis of the angle dependence of the scatter.

The standard way to quantify the distribution and the total amount of scatter of a mirror is expressed by the so-called Bidirectional Reflectance Distribution Function (BRDF) and the Total Integrated Scatter (TIS) [18, 29], respectively. The BRDF is defined as

$$\text{BRDF} = \frac{1}{P_0} \frac{dP}{d\Omega \cos \theta_s} \, ,\tag{2.1}$$

where dP is the optical power scattered into a projected solid angle $d\Omega \cos \theta_s$, θ_s is the scattering angle, and P_0 is the incident energy from the surface. The $\cos \theta_s$-term is a correction to adjust the illuminated area on the mirror to its apparent size when viewed from the scatter direction. When the BRDF is integrated over the solid angle, where θ_s ranges from 0 to $\pi/2$ and ϕ from 0 to 2π, the TIS is found. A correction for the $\cos \theta$-term is made in this integration. The connection between the TIS and the RMS surface roughness σ, is given by [29]

$$\text{TIS} = \left(\frac{4\pi\sigma}{\lambda}\right)^2 \, ,\tag{2.2}$$

assuming that the light is normally incident on the surface. As the scatter was observed to be nicely rotational symmetric, we can use data from one radial direction only. To calculate the BRDF over a larger angular range than found in Fig. 2.2 some additional images were made. To limit the fluctuations in the offset (to ~ 10 units on the 2^{16} scale of the 16 bit camera)

we average on every position over 10 images. Furthermore, to get rid of the speckles, the image is averaged over many vertical pixel lines. The resulting BRDF is shown in Fig. 2.3, where θ_s ranges from $0.14°$ to $7.6°$. The black line fits the calculated data with BRDF= $0.036 \times \theta_s^{-1.33}$. Mirror surfaces which can be described by such a simple power law are named fractal surfaces [29, 30]. Now that we know the distribution of the scatter, we can also calculate the TIS, by integration of the BRDF as found from the fit. The resulting TIS is 1.6×10^{-3}, half of which lies within the θ_s-range of $0 - 20°$. So, for every bounce on the mirrors, a fraction 1.6×10^{-3} of the light is scattered out of the specular direction. This estimate is of course not very accurate as it is found via extrapolation outside the measured θ_s-range.
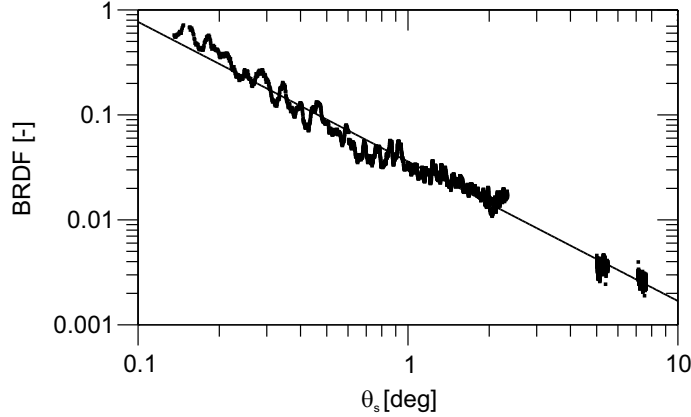
Figure 2.3: *The BRDF for θ_s from $0.14°$ to $7.6°$. The black dots are the BRDF points calculated from similar measurements as shown in Fig. 2.2 and the black line is a fit of the data.*

A ratio that describes which part of the total light escapes the resonator via transmittance of the mirror is the resonator efficiency,

$$\eta = T/(A+T) \, , \tag{2.3}$$

where A is scatter (absorption can be neglected) and T the transmission. The mirror under study has $A = \text{TIS} = 1.6 \times 10^{-3}$ and $T = 4.1 \times 10^{-4}$, which results in $\eta = 20\%$. The rest of the light, roughly 80 %, leaves the resonator via scattering.

Substituting the thus calculated TIS in Eq. 2.2, results in a surface roughness $\sigma = 1.7$ nm. Measurements performed with a (WYKO RST-500) interferometer [31], however, gave a roughness of only $\sigma = 0.4$ nm. This huge difference might result from the wavelength dependence of the multi-layer coating, which comprises 14 pairs of alternating high and low refractive-index $\lambda/4$-layers (at $\lambda = 532$ nm). While our scattering measurement is performed at the design wavelength of 532 nm, the WYKO beam profiler, however, works at a wavelength of 633 nm. At this wavelength, the light penetrates the stack of layers much deeper than at 532 nm. It is not completely understood how this affects the comparison.

Similar experiments to determine the surface roughness have been done by Jakobs [32], Bruno [33], and Elson [34]. They measure the surface roughness of the top-layer with an

AFM and a stylus, out of which the scattering of the multi-layer system is calculated. As the phase relations between individual layers are unknown the calculations can only be performed for two extreme regimes, one where the roughnesses of the consecutive interfaces are fully correlated and the other where they are fully uncorrelated. The mentioned papers perform both calculations.

2.3 Resonator losses

The performance of a Fabry-Perot is generally described in terms of its resonance linewidth (in relation to the free spectral range). Not many people study the peak transmission and hardly anyone looks at the spectrally-integrated or averaged transmission. We will show that the resonator efficiency η can also be determined both from the average transmission under incoherent illumination, as well as from the average transmission of a coherently illuminated resonator $\langle T(\phi) \rangle$ when scanning the length of the Fabry-Perot.

The transmission of a resonator as a function of the single pass phase is [1]

$$T(\phi) = \frac{I_T(\phi)}{I_i} = \left(\frac{T}{T+A}\right)^2 \frac{1}{1 + \left(\frac{2F}{\pi}\right)^2 \sin \phi^2} \ , \tag{2.4}$$

where F is the cavity finesse. The maximum peak transmission of the resonator is found for $\phi = 0$

$$T(0) = \frac{I_T(0)}{I_i} = \left(\frac{T}{T+A}\right)^2 = \eta^2 \ . \tag{2.5}$$

The spectrally-averaged transmission, on which we will elaborate, is given by

$$\langle T(\phi) \rangle = \frac{\langle I_T(\phi) \rangle}{I_i} = \frac{T^2}{2(T+A)} = \tfrac{1}{2} T \eta \ , \tag{2.6}$$

where the relation $\langle [1 + (\frac{2F}{\pi})^2 \sin \phi^2]^{-1} \rangle = \pi/2F = (A+T)/2$ is used ($F^2 \gg 1$). The efficiency η defines how much of the light inside the resonator, leaves via transmission of the mirrors, the rest being scattered and absorbed. Taking into account that $T I_i$ (see Fig. 2.4) defines how much light enters the resonator via the first mirror, Eq. 2.6 can also be rewritten as $\langle I_T(\phi) \rangle = \frac{T}{2(T+A)} T I_i = \tfrac{1}{2} \eta T I_i$.

2.3.1 Spectrally incoherent input beam

A LED, with a central wavelength $\lambda = 525$ nm and a spectral width of 36 nm (FWHM), is used for incoherent illumination of the Fabry-Perot. The mirrors of the resonator are identical to those used in Section 2.2. The cavity length is approximately 10 cm and the cavity is operated far from (lower-order) frequency-degenerate points (see Chapter 5). To operate the resonator at the same wavelength as with a coherent light source ($\lambda = 532.0$ nm), a spectral filter ($\lambda = 532.0$ nm, $\Delta\lambda_{\text{FWHM}} = 3.5$ nm) is placed in front of the LED.

For a proper performance of the experiment, it is important to convert the highly-diverging light coming out of the LED into a more or less parallel beam. We want the light to remain paraxial inside the resonator even after multiple round-trips. This is done in two steps, where
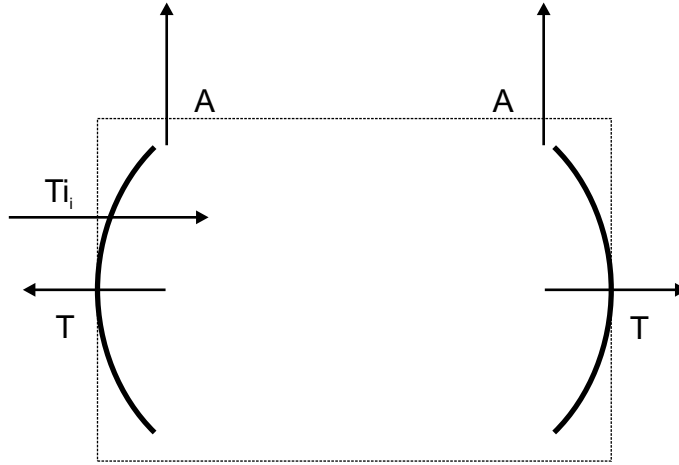
Figure 2.4: *Conservation of energy for an optical resonator requires that of the trapped light a fraction $T/(2T + 2A) = \frac{1}{2}\eta$ is transmitted (coupled out) through each of the mirrors.*

first an enlarged image of the LED is made on a diaphragm (5 mm diameter) and a homogeneous part of this image is cut out. To improve the parallelism of the beam a second diaphragm (5 mm diameter) is placed 50 cm behind the first one, just in front of the resonator. The diameter of the diaphragms is chosen such that the diameter of the beam is smaller than of the detector (8 mm).

The power of the LED is roughly 1 mW, whereas the irradiance behind the mirrors falling onto the detector is sub-nW. To measure reliably at these low output powers, a photomultiplier (HAMAMATSU 5783-01) is used in combination with a chopper and a lock-in amplifier. The transmittance of the front mirror of the resonator, which we have measured first, is $T = (4.0 \pm 0.1) \times 10^{-4}$. This transmission is in nice agreement with the coherent measurement to be discussed in Section 2.3.2. Next, the transmittance behind the resonator (two mirrors) is measured, resulting in an efficiency of $\eta = (23.6 \pm 0.1)\%$. This means that roughly 75 % of the light inside the resonator is lost by scattering or absorption.

Finally, we also wanted to check whether the scatter losses (A-channel in Fig. 2.4) are as strong as would be expected from the (single mirror) BRDF-measurement, described in Section 2.2. For this purpose, the detector is moved from behind the resonator to the side of the resonator where it looks under an angle of 50° inside the resonator to the end mirror. The ratio of the integrated scatter (IS), measured by the detector at this position, divided by the measured scatter losses deduced from the area-integrated spectra (A-channel) is 5.9×10^{-3}. We can calculate a similar ratio from the single mirror BRDF in Section 2.2, as follows. The detector subtends a solid angle of $\Delta\Omega = 6 \times 10^{-2}$ sr at $\theta_s = 50°$. The integrated scatter (IS) is found from extrapolation of the measured BRDF to 50° and integration over the mentioned solid angle $\Delta\Omega$, which results in the ratio IS/TIS$= 6.8 \times 10^{-3}$. This ratio is in nice agreement with the measurement and confirms that the scatter strength as deduced from a two-mirror resonator is identical to that measured on a single mirror.

11

2.3.2 Spectrally coherent input beam

In the next experiment, the resonator is illuminated coherently by a laser (INNOLIGHT Prometheus) at 532 nm, where the beam is mode-matched to the resonator. The length of the resonator is scanned over a few λ with a piezo (PI P-753.1) to obtain the transmission spectrum. The resonances in the transmission (and reflection) spectrum depend on the phase ϕ, determined by λ, L and R. To be able to use the power arguments made in the beginning of this Section, the transmitted power is spectrally averaged over one free spectral range. Doing so, the phase is averaged out.

We know from the previous experiments that scattering losses are approximately $3-5$ times as strong as the transmission of the mirrors. A natural hypothesis is that the scattered light might be "trapped" inside the resonator in the form of (very) high-order modes and thus found in the "floor" of the Fabry-Perot spectrum, *i.e.*, between the resonances. Assuming a finesse of 1000 and a resonance voltage of 1 V on the detector, requires that a floor in the spectrum of 1 mV or less needs to be resolved. To do so, we used a 14-bit digitizer (National Instruments PCI-5911). To resolve the resonances also in the *horizontal* direction, the digitizer is operated at 5×10^6 samples/s. Fig. 2.5 shows the spectrum measured on two vertical scales (two detector amplifications); one to measure the dominant resonances in the spectrum and the other to measure the less prominent resonances and the floor properly. A lens is placed behind the resonator to catch all the light transmitted through the end mirror.

The first result of our measurement is that the floor, if it exists, is smaller than the noise level 0.02 mV, $T_{\text{floor}}/T_{\text{peak}} < 2 \times 10^{-5}$, which demonstrates that the scattered light is *not* found in the spectrum and is thus apparently *not* trapped inside the resonator. Furthermore, we found that the summed transmission on both measurement scales yields an efficiency of $\eta = (20 \pm 2)$ %. We thus find again that only 20 % of the light is transmitted through the mirror, while 80 % escapes via scatter. Of the transmitted intensity roughly 60 % is found in the single prominent resonance (peak ~ 0.3 V) and 40 % is found in the smaller resonances (< 0.05 V).

One might wonder firstly, whether the measured scattering around the reflected beam is sufficient to explain all power loss in a Fabry-Perot resonator in operation and secondly, whether the reflection and the transmission channel affect each other by scattering. To answer the first question, it is important to note that the power ratio of the scatter around the transmitted and reflected beam equals the ratio of the totally transmitted and reflected power. To appreciate this argument, we mention that the angular distributions in both channels are similar as they are Fourier related to the spatial distribution of the same surface. To answer the second question, we mention that our system produces predominantly small-angle scatter. Light scattered out of the beam transmitted by the mirror will therefore not affect light in the reflected beam (and vice versa) because of the angular difference of almost $180°$.

2.4 Connection between cavity finesse and cavity ring-down

In this Section, the performance of a Fabry-Perot is described in terms of the finesse F, which depends on the losses of the resonator via

$$F = \frac{\pi}{1-R} = \frac{\pi}{A+T} \ . \tag{2.7}$$
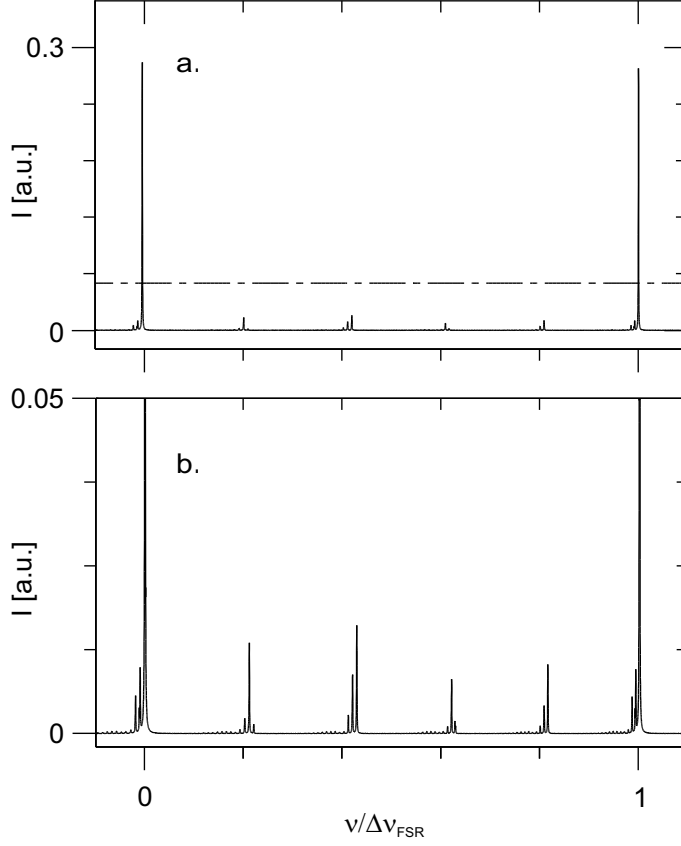
Figure 2.5: *(a) Transmission spectrum of the resonator for one free spectral range. The dashed line indicates the zoomed-in area shown in (b).*

So, if we are able to measure the cavity finesse, the losses can be determined with this relation. Two methods are introduced here, a spectral method and a temporal one.

The spectral method determines the finesse via the ratio of the free spectral range $\Delta\nu_{\text{FSR}}$ and the (FWHM) spectral linewidth $\Delta\nu$

$$F = \frac{\Delta\nu_{\text{FSR}}}{\Delta\nu} \; . \tag{2.8}$$

The temporal method is based on the measurement of the $1/e$ decay time τ of the intracavity intensity after the optical injection has been switched off. This is a so-called "cavity ring-down" experiment [2]. Substitution of the relations $\Delta\nu = 1/(2\pi\tau)$ and $\Delta\nu_{\text{FSR}} = c/(2L)$ into Eq. 2.8 shows how the finesse can also be determined from τ

$$F = \tau\pi c/L \,, \tag{2.9}$$

where c is the speed of light and L is the cavity length.

Performing the spectral measurement, we found that the mirror mounts show a pronounced mechanical resonance at 75 Hz with an acoustic Q-factor of approximately 50. To avoid this resonance, and also its higher harmonics, the scan frequency of the piezo is chosen at 4.6 Hz. At this frequency, the resonator scans in 3.8 ms and 2.8 μs through a FSR and a resonance, respectively. The measured resonance width has a statistical error of 2 %; the line shape is nicely Lorenzian, which shows that the scanning of the resonator is not too fast to perturb the intra cavity field and produce ringing [35]. From this method, we found $F = 1380 \pm 40$. Substituting F in Eq. 2.7 results in $A + T = 2.3 \times 10^{-3}$ which combines with the transmission of a single mirror $T = 4.1 \times 10^{-4}$ to $\eta = (18.0 \pm 0.5)$ %.

Performing the temporal measurement, we start by slowly scanning the resonator length. On the peak of a resonance, a trigger switches off the laser light with an acousto-optic modulator (AOM ISOMET 1205-2). The injection beam switches off in 35 ns and we detect the decaying signal with a 20 MHz-bandwidth detector. The measured decay signal gives a nice exponential decay over two orders of magnitude as shown in Fig. 2.6. The $1/e$ decay time found is $\tau = 0.18$ μs which, in combination with Eq. 2.9, results in $F = 1700 \pm 40$. Furthermore, $A + T = 1.84 \times 10^{-3}$, found from Eq. 2.7, combined with the transmission of a single mirror $T = 4.1 \times 10^{-4}$, gives a cavity efficiency $\eta = (22.2 \pm 0.5)\%$.
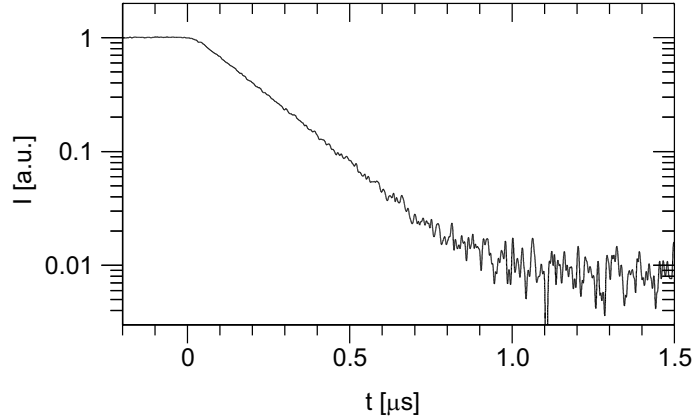
Figure 2.6: *Ring-down curve of a resonator with a cavity length $L = 0.1$ m. The light is switched off at $t = 0$ μs. The fitted ring-down time $\tau = 0.18$ μs corresponds to a finesse of $F = 1700$.*

The difference between the finesse measured with the spectral method and cavity ring-down may be surprising, but has been observed before. A possible explanation has been given by Rempe *et al.* [16]. They state that for a proper *spectral* measurement spatial coherence of the injected field should be retained after repeated reflections. A *temporal* ring-down experiment, however, only requires energy confinement within the cavity, which imposes only a restriction on the "incoherent" field. This is less critical to perturbations by, *e.g.*, scatter, than the restriction on the coherence of the field. Loosely speaking, one might say (in solid-state terminology) that spectral measurements yield something like a T_2-time, whereas temporal measurements yield a T_1-time.

The ring-down method offers an independent method to reject the "trapped-light hypoth-

esis" introduced above. Light recycled in other transverse modes would effectively enlarge the ring-down time. Experimentally, the trapping of scattered light in lower-order modes can be excluded by inserting an intracavity pinhole, absorbing the scattered light. The diameter is chosen such that the lowest order mode is left unaffected. Doing so, the ring-down time of the resonator with intra-cavity pinhole should be shorter than for the situation without. However, the ring-down times were found to be independent of the presence of the intracavity pinhole, consistent with our results in the spectral domain. Apparently, the proper argument is that only a single mode is resonant and scatter cannot be trapped in other modes as they are not resonant. The difference between both methods thus remains unsolved.

2.5   Concluding discussion

The roughness-induced scatter limits the performance of a Fabry-Perot. The scatter of a single mirror is visualized and described by the BRDF and TIS and compared with the losses of a resonator, comprising two mirrors. We show that the finesse and the peak throughput are lower than expected from the mirror's transmission. We have quantified the resonator

Method	Efficiency (η)
TIS	20 %
incoherent illumination	(23.6 ± 0.1) %
coherent illumination	(20 ± 2) %
F_{spectral}	(18.0 ± 0.5) %
$F_{\text{ring}-\text{down}}$	(22.2 ± 0.5) %

Table 2.1: *An overview of the resonator efficiency η determined by the various methods in this Chapter: Via angular-resolved scatter of a single mirror (TIS), via average power measurements for incoherent and coherent illumination of a resonator, and via the spectral width and cavity ring-down.*

efficiency $\eta = T/(A+T)$ by various methods as shown in Tab. 2.1. It shows that all methods give roughly (within statistical errors) identical results; the efficiency of the resonator under study being $\eta \approx 20$ %. Thus 80 % of the light escapes via roughness-induced scattering of both mirrors. Furthermore both the "floor" of a spectrum and the comparison of a spectral and temporal method demonstrate that the scattered light is not resonantly trapped inside the resonator.

CHAPTER 3

Transverse mode coupling in an optical resonator

Small-angle scattering due to mirror surface roughness is shown to couple the optical modes and deform the transmission spectra in a frequency-degenerate optical cavity. A simple model based on a random scattering matrix clearly visualizes the mixing and avoided crossings between multiple transverse modes. These effects are only visible in the frequency-domain spectra; cavity ring-down experiments are unaffected by changes in the spatial coherence as they just probe the intra-cavity photon lifetime.

3.1 Introduction

Optical resonators are used in many experiments; they provide for high resolution in optical interferometry and for field enhancement in QED experiments [4]. At specific "magic" resonator lengths many transverse modes of the resonator have the same eigenfrequencies [12, 21]. Such frequency-degenerate resonators have been suggested as a tool to enhance the efficiency of removing entropy from atoms (cooling) in a resonator [36] and to observe cavity-enhanced spontaneous emission at optical wavelengths [37].

Although loss due to scattering by mirrors is well-known for optical cavities [16, 22], the special role of frequency-degeneracy in scattering is only touched upon in the literature [38] and no systematic study has been performed. In this Chapter, we demonstrate that at frequency-degeneracy it is the *amplitude* scattering instead of the *intensity* scattering that matters and show that the observed difference between time and frequency-domain measurements around frequency-degeneracy is caused by mode-mixing of many transverse modes. The coupling (due to surface roughness of the mirrors) changes the eigenmodes and eigenfrequencies, which no longer coincide at frequency-degeneracy. This results in an inhomogeneous broadening of the measured resonances.

3.2 The experiment

In our experiment, a laser beam at fixed wavelength ($\lambda = 532$ nm) is injected into a symmetric stable (Fabry-Perot) cavity to match its TEM$_{00}$ mode. The cavity is constructed with two nominally identical highly reflective mirrors (specified reflectivity $> 99.8\%$), having a radius of curvature of $R = 50$ cm and a diameter of $D = 5$ cm. We operate the cavity close to a frequency-degenerate point, where the eigenfrequencies of the Hermite-Gaussian (HG) eigenmodes separate into N groups of almost frequency-degenerate modes. At frequency-degeneracy, the Gouy phase θ_0, being the round-trip phase delay between the fundamental HG mode as compared to a reference plane wave, is by definition a rational fraction of 2π: $\theta_0 = 2\pi/N$, the paraxial phase delay of higher-order modes (TEM$_{mn}$) being $(m+n+1)\theta_0$ [12]. In a ray picture of a frequency-degenerate resonator, the ray path closes itself after N (equal to the number of hit points on each mirror) round-trips inside the resonator [21]. For stability reasons, we avoided the popular confocal ($N = 2$) configuration [12]. By way of example, we restrict the discussion to $N = 4$, this corresponds to a cavity length $L = 14.6$ cm at $R = 50$ cm.

We measure transmission spectra by scanning the cavity length L over a few wavelengths with a piezo element. From these spectra we deduce the cavity finesse F as the ratio between the free spectral range $c/(2L) = 1.03$ GHz and the (FWHM) width of the dominant transmission resonance. Fig. 3.1 shows the finesse as a function of the cavity length, which can be accurately adjusted with a translation stage. Note, how the finesse drops from 1300 to 600 around frequency-degeneracy over a range (FWHM) of $\delta = \Delta L/R = 4.3 \times 10^{-4}$. This range corresponds to a frequency difference $\Delta \nu = 0.78$ MHz between consecutive classes of transverse modes ($\Delta(m+n) = N = 4$). The inset shows that the resonance width more than doubles and that the corresponding peak transmission is reduced to below 50% for spectra at $\delta = 0$ as compared to $\delta = -1 \times 10^{-3}$.
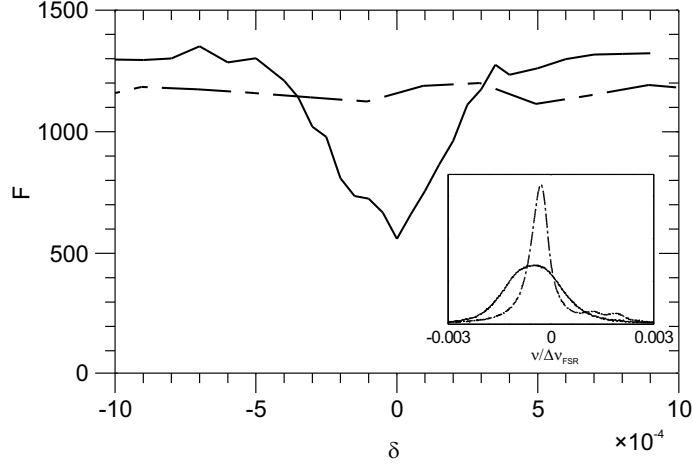
Figure 3.1: *Relative spectral width of cavity resonances, expressed as the finesse F, measured as a function of the normalized cavity length δ, for a resonator with (dashed) and without (solid) a centered intra-cavity pinhole. The inset shows two typical spectra measured at $\delta = 0$ (solid) and $\delta = -1 \times 10^{-3}$ (dashed).*

We attribute the observed drop in finesse to mode coupling induced by scattering at the (imperfect) mirrors. A proof of this statement is given by the dashed curve in Fig. 3.1, which shows the measured finesse for the same cavity with a pinhole centered in the middle of the cavity; *this* finesse is constant over the full range. The intra-cavity pinhole (diameter 1 mm; waist of TEM_{00} mode 0.17 mm) basically converts our multi-transverse-mode system into a single-mode system, by increasing the losses of the higher-order transverse modes and reducing the mode coupling. It thereby removes the mode mixing that caused the finesse reduction and makes the system essentially single transverse mode.

The cavity finesse can also be determined with a cavity ring-down experiment, which measures the intra-cavity photon lifetime after switching-off optical injection [39, 40]. We have performed this experiment (without intra-cavity pinhole) with a sufficiently large detector over the same detuning range and found absolutely no differences at or away from degeneracy. From the measured lifetime of $\tau \approx 0.35$ μs, we obtained a constant value of $F \approx 2200$ over the full range (we do not have an explanation why this value is different from the value $F = 1300$ mentioned above).

Cavity ring-down experiments are insensitive to the power distribution over the transverse modes unless one uses an (extra-cavity) pinhole in front of the optical detector [39, 40]. By passing only a fraction of the amplitude mode profiles, the transmitted power can then reveal beatings between transverse modes that are only orthogonal over their *full* profile. Using this configuration at the degenerate cavity length ($N = 4$), we experimentally observed that the decay becomes nonexponential and, depending on the position of the detector pinhole, can be either faster or slower than the decay observed without pinhole. The obvious conclusion is that we observe the decay and beating of several (nondegenerate) transverse modes that are simultaneously excited by an injection profile that was matched to just a single TEM_{00} mode.

Theoretically, the optical field at any plane in the resonator can be described by separating

19

it in transverse spatial eigenmodes j and amplitudes that change in time

$$E(x,t) = \sum_j a_j(t)u_j(x) \, . \tag{3.1}$$

This evolution is trivial if we assume that all modes have equal loss rates Γ, as should be the case for low-order transverse modes and large mirrors. In a cavity ring-down experiment the spatially integrated intensity decays then with a rate 2Γ. In a spectral measurement, where one scans either the laser frequency or the precise cavity length, a large-area detector will measure

$$P_{\text{out}}(\omega) \propto \sum_j |a_j(\omega)|^2 \propto \sum_j \frac{\left| \int E_{\text{in}}(x) \cdot u_j^*(x) dx \right|^2}{(\omega - \omega_j)^2 + \Gamma^2} \, , \tag{3.2}$$

where the numerator quantifies the spatial overlap between the injected field $E_{\text{in}}(x)$ and the eigenmodes and the denominator quantifies the corresponding spectral overlap.

The key argument we want to make is that the shape of the eigenmodes $u_j(x)$ can be quite different from the usual (HG) shape in a cavity that operates close to frequency-degeneracy. The reason is that even a small amount of scattering at the mirrors can lead to dramatic changes in the modal profile if it can resonantly perturb the mode profile over and over again on consecutive round-trips. A similar phenomenon is known in quantum mechanics, where energy-degenerate perturbation theory is quite different from nondegenerate perturbation theory, which gives second-order expressions that explode at degeneracy as they are inversely proportional to the energy differences between the unperturbed modes.

3.3   Simulations

To find the true eigenmodes in a perturbed cavity we use the observation that the optical field inside a cavity can be described by a Schrödinger-type equation [41]. We take the simplest form of coupling, which is found in many physical systems, and model it with a random matrix **c** of the GOE class [42]. In the basis of the unperturbed HG-modes, the matrix equation for the eigenfrequencies ω_j and eigenmodes $\mathbf{u}_j$ of the coupled system is thus

$$\omega_j \mathbf{u}_j = M\mathbf{u}_j = \begin{pmatrix} c_{00} & c_{01} & c_{02} & \dots \\ c_{10} & \varepsilon + c_{11} & c_{12} & \dots \\ c_{20} & c_{21} & 2\varepsilon + c_{22} & \dots \\ \vdots & \vdots & \vdots & \ddots \end{pmatrix} \mathbf{u}_j \, , \tag{3.3}$$

where ε is the frequency detuning away from degeneracy. The coupling matrix **c** is random but fixed for each realization of the system, with coefficients that are normalized via their statistical variance $\langle c_{ij}^2 \rangle = 1$. Energy conservation is assured via $c_{ij} = c_{ji}^\dagger$ and is physically motivated by the observation that the scattering due to mild surface roughness produces so-called conservative coupling [41]. The amplitudes of the HG modes evolve via the same matrix M as in Eq. 3.3.

For simplicity, we have reduced the transverse dimensionality from 2 to 1, by grouping HG$_{nm}$-modes with the same $n + m$ value and unperturbed eigenfrequency into families

$j = (n+m)/N$, and assume equal coupling between these families. On the one hand, the coupling amplitudes between the individual modes will decrease with increasing mode number difference, as small-angle scattering due to gradual variations of the mirror height profile generally dominates over large-angle scattering [29]. On the other hand, the coupling between mode families will increase with mode number as the number of modes per family also increases. For simplicity again, these counter-acting phenomena are assumed to balance.

The white curves in Fig. 3.2a show the calculated eigenfrequencies as a function of the detuning ε for 10 eigenmodes. Far from degeneracy, the on-diagonal elements of M dominate the dynamics, the eigenmodes closely resemble the HG-modes with equally-spaced eigenfrequencies $j\varepsilon$. Around degeneracy, mode mixing occurs and the eigenvalues exhibit a "10-mode" avoided crossing, with "level repulsion driven chaos" [42] as central at $\varepsilon = 0$. Whereas the white curves show the eigenfrequencies of all modes, the underlying picture is sensitive to the overlap with the injection mode, making some (lower-order) modes visible around degeneracy, whereas others are barely excited. Fig. 3.2a has been obtained by assuming a damping rate $\Gamma = 1$ to produce finite spectral widths and a realistic injection profile $E_{in}(x)$ that is matched to the fundamental HG mode. Note how the almost single-mode excitation away from degeneracy unavoidably decomposes into many (modified) eigenmodes at degeneracy.

Fig. 3.2b shows a composite plot of the measured transmission curves as a function of the normalized cavity length δ, which can be transformed into a frequency detuning via $d\varepsilon/d\delta \approx Nc/[2\pi L \sin(\theta_0/2)] = 1.84$ GHz. We dominantly excite the TEM$_{00}$; the intensity ratio of the TEM$_{04}$ and TEM$_{00}$ is only 5%. Note that close to frequency-degeneracy $\delta = 0$ the peak transmission reduces and the resonance broadens due to mode-mixing, as shown previously in Fig. 3.1. The results of our model are in nice agreement with the measurements.

For a qualitative comparison between the mirror surface roughness and the mode coupling, we note that the amplitude of the roughness is directly proportional to the coupling amplitude c_{ij} between modes. The spatial frequency of the roughness determines the scattering angle or equivalently the TEM$_{mn}$-mode to which the scatter couples; the system is particularly sensitive to spatial frequencies in the order of the inverse beam size (0.17 mm). A rough estimate of the scatter *amplitude* c_{ij} is given by the ratio of the locking range over the free spectral range, being 8×10^{-4} (roughly equal to the scaling between Fig. 3.2a and b). Away from frequency-degeneracy the system feels only the scatter *intensity* which is less than 10^{-6} per mode.

From a general perspective, the time and frequency domain measurements of the cavity finesse provide information that is similar to the T_1 (population decay) and T_2 (dephasing) time measured in coherent spectroscopy, respectively. The time-domain ring-down experiment only measures intensity decay rates and is thus equivalent to a T_1-measurement. The measurement in the frequency domain is phase sensitive and thus equivalent to a T_2-measurement.

The level repulsion phenomena described in this Chapter, which we also observed for several sets of other mirrors, give our system the flavor of a chaotic system [42]. This is not really surprising when we think of the (imperfect) mirror as a deterministic random scatterer. Although the experiments show level repulsion qualitatively, we cannot prove chaos to its full extent.

In conclusion, we have demonstrated mode coupling in a passive resonator. The coupling changes the eigenmodes and eigenfrequencies, which no longer coincide at frequency-
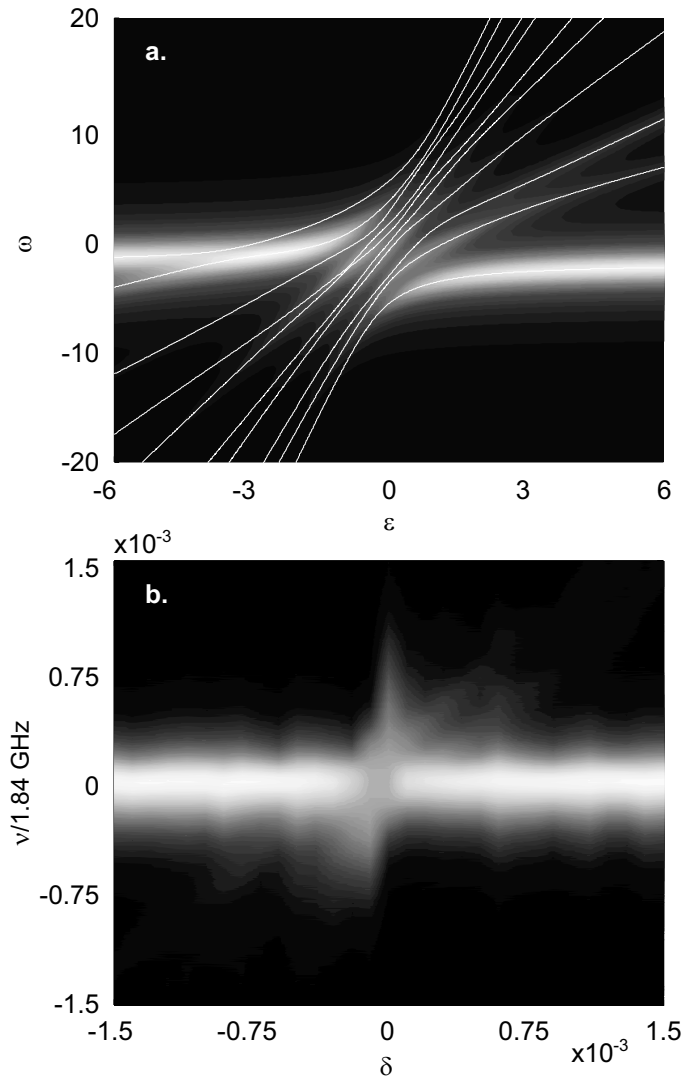
Figure 3.2: *False color (white=high and black=low) plot of the cavity transmission as a function of the normalized frequency detuning (horizontally) and frequency (vertical); vertical cuts represent transmission spectra at fixed cavity length. Both (a) simulations and (b) experimental data show how mode coupling leads to a spectral broadening and a reduction in peak transmission around the frequency-degenerate point $\varepsilon = \delta = 0$. Both effects result from level repulsion and mode mixing.*

degeneracy. This results in an inhomogeneous broadening of the measured resonance and explains the difference between the finesse measured in the time and frequency domain. A coupled-mode model correctly describes the observed behavior. These effects *cannot* be observed by cavity ring-down experiments; this should serve as a warning to experimentalists.

Appendix (unpublished material)

In this appendix, we discuss in more detail a number of topics, that were only touched upon in the previous Sections. First, we visualize how the shape of the mode changes due to mode coupling. Then, we estimate the number of modes involved in the coupling. As the "coupled" basis is unknown, we project it onto the standard eigenmodes in the "uncoupled" basis, *i.e.*, the Hermite-Gaussian (HG) modes. Finally, the nonexponential decay observed in certain cavity ring-down experiments is highlighted.

3.A Shape of the eigenmodes

We have mentioned that mode coupling also changes the shape of the eigenmodes. To quantify this statement, we have measured intensity profiles of modes behind the scanning resonator with an intensified CCD-camera (ICCD). The frequency-degenerate resonator ($N = 4$) is injected again with a beam mode-matched to the fundamental mode. When the resonator scans through a resonance in the spectrum, the ICCD-camera is triggered to image the intensity profiles. The advantage of the ICCD-camera is that the gatewidth ($\sim$shuttertime) is only 30 ns, very small as compared to the resonance width (FWHM) of ~ 10 µs. This means that we can visualize the mode profiles for a fixed cavity length.

The intensity profiles are measured at frequency-degeneracy ($\delta = 0$) and away from frequency-degeneracy ($\delta = 0.6 \times 10^{-3}$) in a symmetric cavity with $R = 50$ cm. Fig. 3.3a shows the profile away from frequency-degeneracy. We observe a nice HG$_{00}$ intensity profile that we expect as only the lowest-order mode is excited and no higher-order modes are available. Fig. 3.3b shows the mode profile at frequency-degeneracy. There is still strong intensity in the center, but the mode profile is now highly distorted and shows a honeycomb-like or speckled structure. Also outside the region, shown in Fig. 3.3b, the intensity profile is different from Fig. 3.3a. At frequency-degeneracy, scattered light is present much further outside the on-axis region even up to 10 times the waist. This shows that light is also weakly coupled to many, many higher-order modes up to a mode number $m \sim 10^2 = 100$. We conclude that the light dominantly couples to the lower-order modes, but also somewhat to higher-order modes as long intensity tales are present far away from the intensity center.

3.B The number of modes involved

Now that we have demonstrated the change of the shape of the eigenmodes, and roughly know the distribution of the scattered light over the (coupled) modes, the question remains how
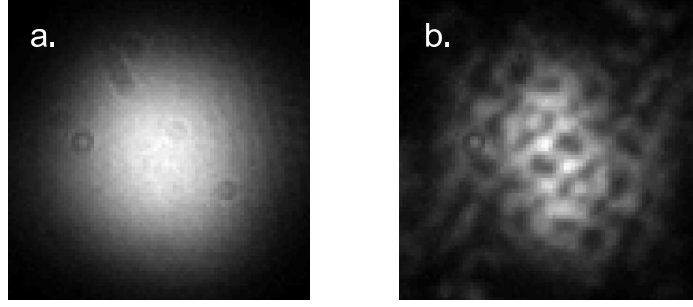
Figure 3.3: *Intensity profiles on the mirror of a resonator tuned (a) away from degeneracy and (b) at degeneracy. In both situations the cavity is injected with an (identical) input beam that is mode-matched to the fundamental mode. Away from degeneracy, we observe the fundamental Hermite-Gaussian eigenmode, whereas at degeneracy the modeprofile is totally different as the mode coupling has defined a new set of resonator eigenmodes. The dimensions of both images are 0.45×0.45 mm^2.*

many modes are involved in the coupling process. An answer to this question can be found in both the spatial and spectral domain. Measurements in the spatial domain reveal the mode number of the *highest-order* mode involved in the coupling process. Spectral measurements, on the other hand, help us to find the *effective number* of modes involved. The effective number of modes is a good measure for the number of lower-order modes involved, as light is dominantly scattered to these lower-order modes.

3.B.1 Spatial domain

In the spatial domain, the highest HG-mode that participates in the coupling can be found in two ways. First of all, it can be deduced from the spatial structure in the mode profile shown in Fig. 3.3b. The highest spatial frequency can be attributed to the highest-order mode involved. Siegman [12] states that the spatial period Λ_m of mode number m and the mode number m are related via $\Lambda_m \approx 4w/\sqrt{m}$, with w the waist of the fundamental mode. An intersection of the intensity profile shows that the lowest spatial period is $\Lambda \approx 31$ μm, which corresponds to a mode number of $m = 480$ for a waist of $w = 170$ μm. Taking into account the 4-fold frequency-degeneracy, which means that at resonance only one out of four modes is excited, we estimate for the total number of coupled modes $\sim 480/4 = 120$.

As an alternative method to determine the highest-order coupled mode, we insert an on-axis diaphragm inside the resonator. The opening of the diaphragm is increased until the intensity profile on the mirror does not change anymore. For this setting, all modes pass apparently the diaphragm. The diameter of the diaphragm $2a$ is a direct measure for the mode size. The corresponding mode m number is found from $m \approx (a/w)^2$ [12]. Experimentally, we find that for a diameter of the diaphragm of 6 mm (and higher) the spatial period remains constant. Combined with $w = 170 \times 10^{-4}$ μm, the highest-order mode has a mode number $m \sim 310$. This is roughly in agreement with the measurement based on the spatial period.

3.B.2   Spectral domain

The number of modes involved in the coupling process can also be estimated from the experimental cavity transmission shown in Fig. 3.2. More specifically, we use the width of the dip in frequency detuning $\Delta\delta$ (horizontal scale) in combination with the broadening of the normalized spectral difference $\Delta\nu/1.84$ GHz (vertical scale). This estimate from the experiment is based on, and validated by, the numerical simulation. For clarity, we note that in the experimental spectra $\Delta\delta$ and $\Delta\nu/1.84$ GHz indicate the frequency detuning and the normalized spectral difference, whereas in the numerical simulation $\Delta\varepsilon$ and $\Delta\omega$ are used.

The theoretical description centered around Eq. 3.3 is based on the assumption that all modes contribute equally to the mode coupling at $\varepsilon = 0$. For increasing ε, higher-order modes will contribute less, and modes no longer contribute if $N\varepsilon \gg c$. For small c values, only the two lowest-order modes (TEM$_4$ and TEM$_0$) couple. The width of the dip in frequency detuning $\Delta\varepsilon$ thus scales linearly with the scatter amplitude c. The broadening of the normalized spectra at $\varepsilon = 0$ is determined by the eigenvalue of a $N \times N$-matrix. Assuming equal scatter amplitudes c, $\Delta\omega$ scales with $\sqrt{N}c$ instead of c.

The number of modes involved can thus be found experimentally from the ratio of $\Delta\nu/1.84$ GHz and $\Delta\delta$ squared

$$\left(\frac{\Delta\nu/1.84 \text{ GHz}}{\Delta\delta}\right)^2 = \left(\frac{\sqrt{N}c}{c}\right)^2 = N \,. \tag{3.4}$$

From Fig. 3.2b we deduce that $\Delta\nu/1.84$ GHz$= 8.8 \times 10^{-4}$ and $\Delta\delta = 3.1 \times 10^{-4}$, which results in $N = 8$. The assumption that all modes contribute equally shows that light is scattered *effectively* to 8 lower-order resonant modes.

We conclude from the measurements in the spatial domain that the light is coupled to $75 - 120$ modes, and that the highest-order mode involved has a mode number $m = 310 - 480$. The coupling to the higher-order modes is, however, very weak. Spectral measurement show that light is dominantly coupled to the 8 lowest-order modes present.

3.C   Cavity ring-down and mode beating

To further clarify the nonexponential decay and the mode beating in cavity ring-down at frequency-degeneracy, mentioned in Section 3.2, we demonstrate additional experimental results and introduce some theory [12]. The total field of two modes with eigenfrequencies ω_1 and ω_2 is obviously given by

$$E(x,t) = u_1(x)e^{-i\omega_1 t} + u_2(x)e^{-i\omega_2 t} \,, \tag{3.5}$$

where $u_1(x)$ and $u_2(x)$ are the spatial transverse patterns of the modes. The intensity signal that this field will produce at the detector with transverse dimension A is

$$I(t) = \int_A |E(x,t)|^2 dx = I_1 + I_2 + I_{12}\cos[(\omega_1 - \omega_2)t] \,, \tag{3.6}$$

25

where I_1 and I_2 are just dc-currents and I_{12} is the beat frequency term, $\omega_1 - \omega_2$ being the beat frequency between the modes. The beat frequency term I_{12} equals

$$I_{12} = \int_A u_1^*(x) \cdot u_2(x) dx \begin{cases} = 0 & \text{if } A > \text{mode size} \\ \neq 0 & \text{if } A < \text{mode size} \end{cases}.$$

This integral cancels out to zero if the detector area A is bigger than the area spanned by the two modes, which have orthogonal modeprofiles. If the detector area A is smaller than the size of the modes, the modal overlap does not integrate to zero and beating occurs. The value (and sign) of I_{12} depends strongly on the size and position of the aperture in the output. Next, we will show this experimentally, for a ring-down experiment observed with a "bucket"-detector ($A > $ mode size) and a "point"-detector ($A < $ mode size) .

Away from frequency-degeneracy ($\delta = 0.6 \times 10^{-3}$), the ring-down curves in Fig. 3.4a are observed to be independent of the size of the detector. In the absence of coupling only a single mode is excited. At frequency-degeneracy, however, multiple modes will be excited with slightly different ω's. Observation of the ring-down signal with a "bucket"-detector still shows that the beating term cancels. For a "point"-detector, either on- or off-axis, the beating causes a nonexponential decay due to the level-repulsion caused by the mode coupling; this is shown in Fig. 3.4b. The decay can be faster or slower than the exponential decay, and depends on both position and size of the aperture. The reason that we observe less than one full oscillation must be that the frequency difference $v_1 - v_2$ is substantially smaller than $1/\tau \approx 3$ MHz.
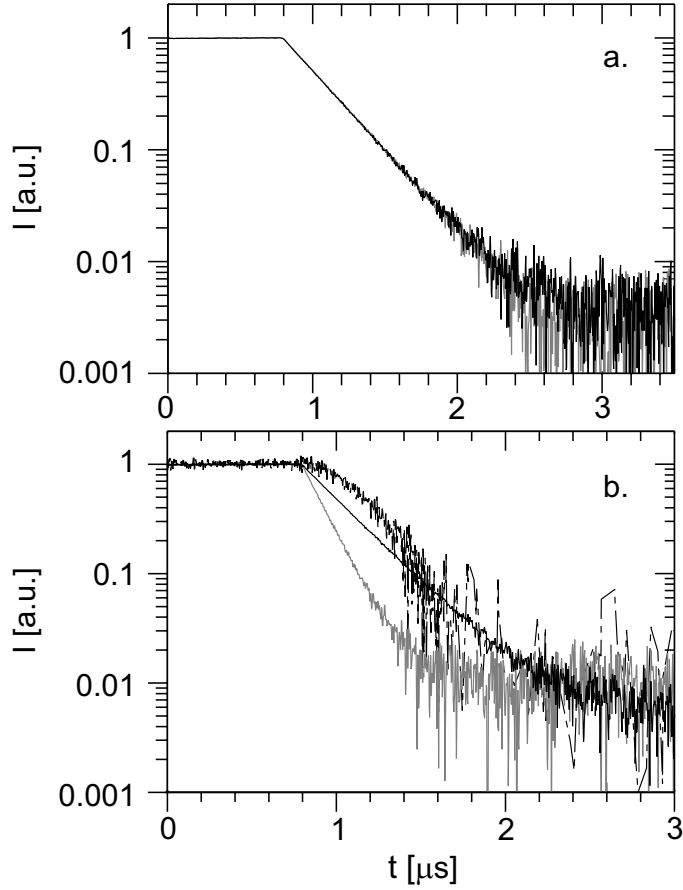
Figure 3.4: *(a) Ring-down curves of a resonator tuned $\delta = 0.6 \times 10^{-3}$ away from the $(K/N = 1/4)$ frequency-degeneracy, as observed with a detector with an effective diameter of 8 mm (black) and 1 mm (grey). The ring-down curves for the "bucket"- and the "point"-detector are identical. The fitted decay time $\tau = 3.1 \times 10^{-7}$ s corresponds to a finesse $F = 1970 \pm 50$. (b) Ring-down curves at exact degeneracy $(K/N = 1/4)$ for a "bucket"-detector (solid black), an on-axis "point"-detector (grey) and an off-axis "point"-detector (at $x = 0.75$ mm) (wiggly dotted). The ring-down curve for the "bucket"-detector shows an exponential decay, whereas the curves for the "point"-detectors show a nonexponential decay, indicating mode beating. The measurement of the off-axis "point"-detector is very noisy because of the low power.*

CHAPTER 4

Resonant trapping of scattered light in a degenerate resonator

We demonstrate and discuss the formation of an intriguing interference fringe pattern that is visible in stable resonators at resonator lengths corresponding to a higher-order frequency-degeneracy. The optical trajectories that form these fringes are described for arbitrary degeneracy; the fringes can be used to visualize and quantify imaging aberrations of the cavity relative to a cavity consisting of ideal mirrors.

4.1 Introduction

In textbooks [43, 44], two main types of interference rings are presented: rings of equal inclination, visible in, *e.g.*, a planar Fabry-Perot, and rings of equal thickness, often called Newton rings. It is also known that under certain conditions a third type of interference rings can be observed in the transmission pattern of a multi-transverse-mode Fabry-Perot cavity with spherical mirrors [19, 45, 46]. For cavity lengths close to frequency-degeneracy rings are observed that are formed by interference in closed optical paths and are resonantly trapped; we dub these "rings of equal (multiple) round-trip path length".

Such interferograms of Fabry-Perot cavities have already been demonstrated in the sixties [19, 45, 46], but only for special cases and generally only for plane-wave illumination. Concentric cavities, which reproduce the optical field on a single round-trip, are discussed by Arnaud [47]. Confocal cavities, which reproduce the field after two round-trips, are discussed by, a.o., Hercher [19] and Bradley and Mitchell [45]. Cavities with other, more general, degeneracies have, however, not been studied to our knowledge.

In this Chapter, we generalize the description of the interferograms for the confocal resonator to resonators, which reproduce the optical field after an *arbitrary* integer number of round-trips (arbitrary degeneracy), including the effect of spherical aberration. We explain the observed interference fringes with a similar approach as Bohr used to explain the discrete levels in atomic systems [48]: we use a ray description to find the optical path (Fermat's principle) and impose the wave criterium that the *N*-fold round-trip path length should equal a multiple wavelengths.

As an example, we have chosen (arbitrarily) a 6-fold degeneracy cavity. As compared to the earlier work [19, 45, 46], where plane wave, *i.e.*, wide-beam, illumination is used, we use *localized* illumination with a narrow beam. Although we dominantly excite the TEM_{00}-mode, we still observe, surprisingly, weak interference fringes spread over the full mirror aperture. This is due to scattering at the mirrors. This indirect illumination offers a crucial advantage over wide-beam illumination as the resulting fringe pattern is stationary and hardly sensitive to variations in the cavity length. We demonstrate how the fringe pattern can be used to visualize and quantify the imaging aberrations of the cavity. In particular, we demonstrate how the use of higher-order degeneracies allows one to increase the sensitivity for global deformations, like astigmatism, up to accuracies of $\lambda/1000$.

In Section 4.2, we introduce the experiment and describe the formation of the fringe pattern. A generalization of the ray description to arbitrary degeneracy is discussed in Section 4.3. In Section 4.4, we present an application of the interference patterns for very accurate measurement of cavity aberrations. We also give a quantitative description of the relation between the observed interference patterns and mirror deviations from the ideal spherical form. In Section 4.5, we propose a potential application. We summarize our work in Section 4.6.

4.2 Experimental setup and fringe formation

Our optical resonator (see Fig. 4.1) consists of two highly reflective mirrors (nominal specification $R > 99.8\%$ and measured finesse $F \approx 1500$) with a radius of curvature of 50 cm and a

diameter of 5 cm. We probe the resonator with a weakly focussed beam of 1.7 mm diameter at a wavelength of 532 nm, produced by a frequency-doubled single-mode Nd:YAG laser, which dominantly excites the TEM_{00}-mode. We use a piezo element to scan (1 s period) the cavity length over a few wavelengths and average over the cavity resonances. One mirror is placed on a high-resolution mechanical translation stage to set the overall cavity length.
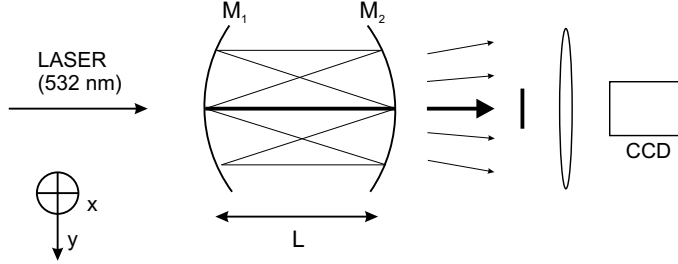

Figure 4.1: *A laserbeam is injected into a symmetric resonator of length L, comprising mirrors M_1 and M_2 of equal radius R. The fringe pattern formed inside the resonator is imaged by a lens onto a CCD-camera. The central ray is obscured to prevent overexposure of the CCD-camera.*

As frequency-degeneracy plays a crucial role in our experiment, we will first explain this concept on the basis of the Gouy phase. In a wave-optical description, the Gouy phase θ_0 is the round-trip phase delay between the fundamental Hermite Gaussian (HG)-mode as compared to a reference plane wave; higher-order modes (TEM_{mn}) experience a phase delay of $(m+n+1)\theta_0$ [12]. At frequency-degeneracy the Gouy phase is by definition a rational fraction of 2π, $\theta_0 = 2\pi K/N$, with as extreme cases the planar ($K = 0$) and concentric ($K = N$) cavities that operate at the edge of stability. In the ray-optical description, N is the number of longitudinal round-trips that is needed before the ray returns on itself [49], while K represents the number of transverse "oscillations" an orbit makes before closing. For a symmetric cavity, the cavity length L, for which these degenerate points occur, follows from $L = R[1 - \cos(\theta_0/2)]$, where R is the radius of curvature of the mirrors. In this Chapter, we (arbitrarily) chose the degeneracy $K/N = 1/6$, which corresponds to a cavity length $L = 6.7$ cm at $R = 50$ cm. Contrary to the confocal and concentric cavities studied previously [19,45,46], our cavity is not at the border of the stability region but well inside [12].

The weak interference fringes, alluded to in Section 4.1, are only observed around frequency-degenerate cavity lengths, where the eigenfrequencies of several eigenmodes overlap. After blocking the on-axis injection beam with a thin obscuration behind the cavity this fringe pattern is imaged by a lens onto a CCD-camera. A typical interference pattern, as observed for a cavity length slightly *longer* than this cavity length, is shown in Fig. 4.2a. The fringes are (almost) circular and the aperture of the mirror is clearly visible. Another pattern, typical for cavities slightly *shorter* than exact degeneracy, is shown in Fig. 4.2b. We attribute the fringes in both these patterns to light that is scattered at the (imperfect) mirror surface out of the injected fundamental mode [50] and resonantly trapped inside the cavity for some specific scattering angles, but not for others.

The advantage of the use of localized over wide-beam illumination is that the fringe pattern is very robust against vibrations; large amounts of scattered light are generated only
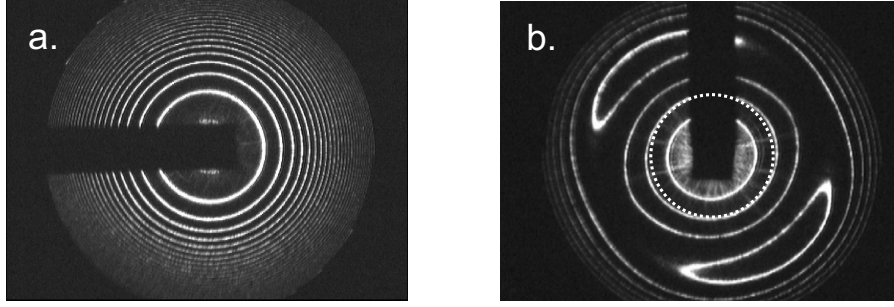
Figure 4.2: *(a) Interference pattern for a cavity tuned slightly longer ($\varepsilon = 50$ μm) than an exact degeneracy of $K/N = 1/6$. The imaged mirror aperture is 5 cm. (b) Interference pattern for a cavity tuned slightly shorter ($\varepsilon = -80$ μm) than an exact degeneracy of $K/N = 1/6$.*

when the cavity length corresponds exactly to a resonance of the fundamental mode. Piezo-scanning of the cavity length leads then to a stroboscopic effect and offers a stationary time-averaged interference pattern. This is contrary to the case of wide-beam illumination which is much more sensitive to vibrations. In that case, there is resonant light present in the cavity for every cavity length: sub-wavelength variations in the cavity length readily wash out the interference pattern, as they lead to shifts of the interference pattern over full fringe distances.

Fig. 4.3 gives a clear demonstration of the buildup of the interference fringes in Fig. 4.2a and b. For clarity, we injected at degeneracy slightly off-axis, which is indicated in Fig. 4.3 by the six bright spots. The piezo, which drives one mirror, is scanned very slowly (100 s period), whereas Fig. 4.2a and b are the result of fast scanning through many resonances. The slow scanning allows us to capture the interference patterns for a specific (almost fixed) cavity length and helps us to visualize the build up of the interference fringes around a single resonance.

Part of the light in the six hit points is scattered into *elliptical* periodic 2D-orbits (see Fig. 4.3) for which only one scatter event is needed. The turning points or vertices of these elliptical orbits form the interference fringes such as shown in Fig. 4.2a and b. The position of the turning points, or equivalently the length of the long axis of the ellipses, is determined by the condition for constructive interference. The total path length of a scatter orbit through the resonator (see Fig. 4.4), of which the hit points on the mirrors are visible as elliptical segments on the mirrors, then has to be a multiple of λ. The ellipses that form the next interference fringe have a total path length which is one λ longer (outside Fig. 4.3). The short axis of the ellipses is determined by the distance between the injection spots out of which the light is scattered.

In the rest of this Chapter, we assume *on-axis* injection, which means that the six injection spots, which were assumed before, now overlap and the scatter ellipses squeeze thus into lines. The fringes are then formed by series of the vertices of *in plane* 1D-orbits. The number of ellipses and the orientation of the ellipses is determined by the precise spatial distribution of the scatter.
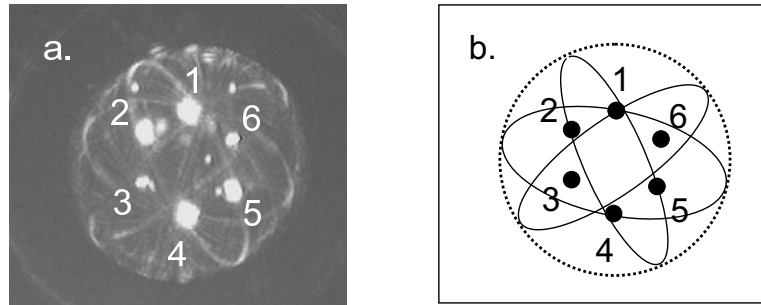
Figure 4.3: *(a) Observation and (b) schematic representation of the buildup of one fringe (m = 1) on the mirror under slow-scan imaging. The 6 bright spots (numbered) are a result of off-axis injection into a N = 6 degenerate cavity. The ellipses are formed by light that is scattered out of the six hit points into periodic orbits. Only the ellipses that interfere constructively after one round-trip (total path length equals λ) are visible. The turning points of the scatter ellipses are observed as the fringe (dotted circle), which has a diameter of 1 cm.*
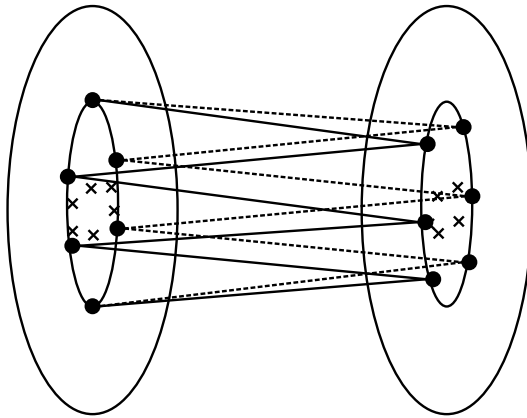
Figure 4.4: *Ray-trace of one periodic orbit through a two-mirror resonator with a degeneracy of N = 6 forming a 2D-ellipse on the mirrors. The hit points of the slightly off-axis injected beam on the mirrors are represented by crosses and the rays in the back are dotted for clarity. The turning points of many of these ellipsis form a fringe in the interference pattern.*

The buildup of the fringes out of elliptical orbits is confirmed by another experiment, where we inserted from *one* side of the resonator a thin obscuration into the cavity. As shown in Fig. 4.5, we observe not *one* but *two* shadows in the fringe pattern, one directly behind the obscuration and the other symmetrically around the optical axis. The obscuration blocks the light scattered out of the injection beam, and obscures a number of ellipses formed out of scattered light. As an ellipse is mirror symmetric around the optical axis, the obscuration of these ellipses appears in the interference fringe patters as *two* shadows.
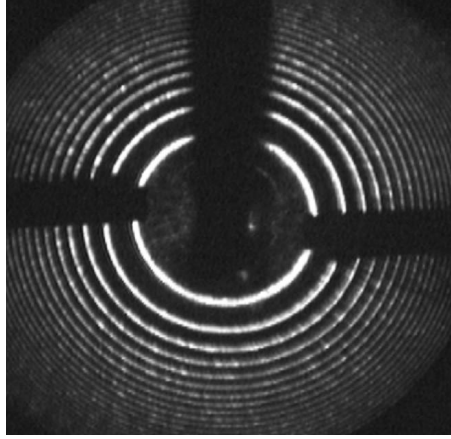
Figure 4.5: *Interference patterns at $\varepsilon = +50 \ \mu m$. The vertical shadow is the obscuration outside the resonator blocking the injection beam. The two horizontal shadows are due to a single obscuration inside the resonator.*

4.3 Calculation of "average round-trip path length"

A description of the total round-trip path length in a cavity operating close to an *arbitrary* frequency-degeneracy (including the spherical aberration), other than for the confocal and concentric case, is missing in the literature. In this Section, we will present such expression. We will use a perturbative approach, where we start with the well-known "ABCD-matrix" formalism [12] and add the spherical aberration in a perturbative way by calculating the length of a closed round-trip beyond the second-order expression. We will present a 1D analysis, which properly describes the interference fringes, formed out of the 1D orbits.

For a symmetric two-mirror resonator, we assume that the hit points on the (ideal spherical) mirrors are given by the paraxial form $x_n = \rho \cos(n\theta_0 + \phi_0)$ [49], where $\theta_0 = 2\pi K/N$ is the Gouy phase, ρ is the maximum transverse displacement, and ϕ_0 determines the phase of the first hit point (the ϕ_0 values on the two mirrors differ by $\theta_0/2$). We then calculate the single transit path length $L_{n,n+1}$ between the mirror hit points x_n and x_{n+1} up to fourth order in these transverse displacement. Finally, we average over all x_n values to obtain the average path length

$$\frac{1}{2N}L_{\text{tot}}(\rho) = (L_{\text{res}} + \varepsilon) - B\varepsilon\frac{\rho^2}{R^2} - A\frac{\rho^4}{R^3} \ , \tag{4.1}$$

where $\varepsilon = L - L_{\text{res}}$ is the length detuning away from exact $1/N$-degeneracy and $L_{\text{res}} = R[1 - \cos(\theta_0/2)]$. Note that by Fermat's principle the round-trip path length of the *physical* ray is approximately equal to the length of a nearby closed ray for which the hit points on the mirrors are given by equation mentioned above. The detuning coefficient B and the spherical aberration coefficient A are simple functions of the Gouy phase

$$A = \frac{1 + \cos(\theta_0/2)}{32[1 - \cos(\theta_0/2)]} = \frac{2R - L_{\text{res}}}{32 L_{\text{res}}} \quad \text{and} \tag{4.2}$$

$$B = \frac{1}{2}\left[\frac{1}{1 - \cos(\theta_0/2)}\right] = \frac{R}{2 L_{\text{res}}} . \tag{4.3}$$

Both coefficients are always positive as $L_{\text{res}} < 2R$ for stable resonators and the off-axis path length $L_{\text{tot}}(\rho)$ is thus always smaller than the on-axis path length $L_{\text{tot}}(0)$. The term containing B is the paraxial term (second order in ρ) and the term containing A is the nonparaxial term (fourth order in ρ), which makes L_{tot} a nonparaxial expression.

The above expressions for A and B are only valid for degeneracies with $N \geq 3$, for which the cycle phase ϕ_0 drops out of the averaging $\langle L_{n,n+1} \rangle$. For the confocal case ($N = 2$), the round-trip path length does depend on the cycle phase ϕ_0 [19, 46]. As a result, the "V-type"-orbit has no ρ^4-term whereas the "bowtie"-orbit has an A-coefficient that is twice the value of Eq. 4.2, *i.e.*, $A = 1/16$. For $N = 2$, our general result, Eq. 4.1, thus reduces to the $N = 2$ result of Hercher [19] and Ramsay and Degnan [46], after substitution of the extreme transverse displacements $x_m = \rho \cos(\pi/4) = \rho/\sqrt{2}$.

Fringes appear on the mirrors when the scattered light rays interfere constructively, *i.e.*, when the round-trip path length L_{tot} equals a multiple of a wavelength $n\lambda$ (n is an integer). For $\rho = 0$, we find from Eq. 4.1 the on-axis interference condition: $2N(L_{\text{res}} + \varepsilon) = n_0\lambda$, which gives us for $\rho \neq 0$

$$-2N\left(B\varepsilon\frac{\rho^2}{R^2} + A\frac{\rho^4}{R^3}\right) = (n - n_0)\lambda . \tag{4.4}$$

Using $m = n_0 - n$, the fringe radii for various ε can be calculated by rewriting Eq. 4.4

$$\rho_m^2 = R\frac{B}{2A}\left(-\varepsilon \pm \sqrt{\varepsilon^2 + m\lambda 2R\frac{A}{B^2}}\right) . \tag{4.5}$$

For $\varepsilon > 0$, ρ_m has only one solution and only for $m > 0$. For $\varepsilon < 0$, Eq. 4.5 has one solution for every $m > 0$ and maximally two solutions for $m < 0$. In the regime where ρ has two solutions, two fringes in the interference pattern fulfill the same interference condition and have the same total path length.

For our specific $N = 6$-configuration, we have calculated the fringe radii for $m \in [-6, 10]$ on the interval $\varepsilon \in [-0.15, 0.17]$ mm using Eq. 4.5, indicated by the solid lines in Fig. 4.6. For $\varepsilon > 0$, it is obvious that every m has only one solution and for $\varepsilon < 0$, m can have two solutions. We also determined the fringe radii as a function of ε experimentally from interference patterns such as shown in Figs. 4.2a and 4.2b, represented by the dots in Fig. 4.6. The excellent agreement of the calculations and measurements confirms our model.
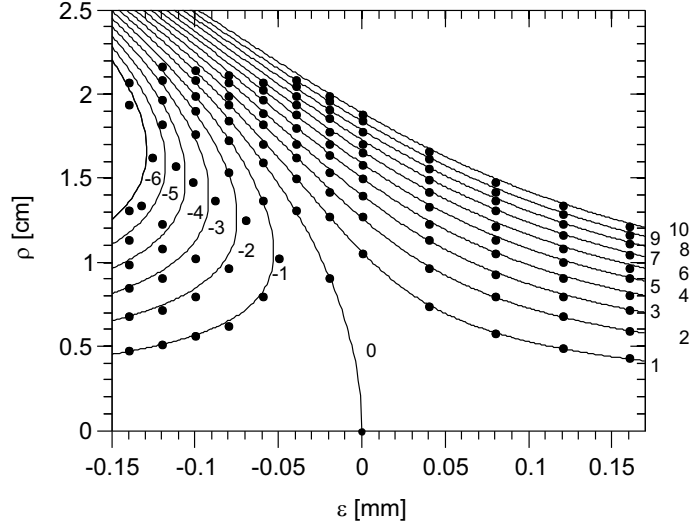
Figure 4.6: *The fringe radius ρ as a function of the distance ε from exact $1/6$-degeneracy. The solid lines are the calculated fringe radii and the dots are the measured fringe radii. There is no adjustable parameter except from a small scaling ($1.14\times$) of the vertical axis to correct for the sharp imaging outside the resonator due to defocussing of the resonator. The numbers in the figure indicate the fringe numbers.*

We noticed that the experimental fringes are imaged sharply in a plane behind the cavity and not on the mirror where the theoretical fringe radii are calculated. The sharp imaging outside the resonator occurs as the rays (of the *physical* path) do not fully coincide, due to intrinsic defocussing of the resonator as described in Eq. 4.1; the fringes are localized where the rays intersect, in our case outside the resonator. That a sharp image of the fringes is not found in the center of the resonator but away from this point has already been mentioned by Bradley *et al.* [45]. We corrected the fringe radii for the diffraction over this distance for a proper comparison (see discussion around Fig. 4.7).

4.4 Aberrations

The transmission interferogram of a cavity composed of two nonspherical mirrors will obviously deviate from that observed or calculated for a cavity with two spherical mirrors. The difference between these interferograms is a sensitive measure for the differences between their mirror height profiles as all mirrors are hit N times, where N can be very large. By comparing the observed interferogram with that expected for ideal spherical mirrors (Eq. 4.1), one can easily deduce the position-dependent change in N-fold round-trip path length $\Delta L_{\text{tot}}[\rho\cos(\theta_0/2), \rho\sin(\theta_0/2)]$ via the criterium that for every extra fringe the total path length changes by λ. The relation between this ΔL_{tot}-profile and the actual height profiles $h_i(\vec{r})$, by which the two mirrors deviate from their ideal spherical reference, is more complicated due to the zigzag nature of the round-trip path. It involves a summation over all

N hit points on each mirror and can be written as

$$\Delta L_{\text{tot}}(\rho \cos \varphi, \rho \sin \varphi) = 2 \sum_{n=1}^{N} h_1(x_n, y_n) + h_2(x'_n, y'_n)$$

$$\approx \frac{2N}{\pi} \int_{-\rho}^{\rho} \frac{h(r \cos \varphi, r \sin \varphi)}{\sqrt{\rho^2 - r^2}} dr . \qquad (4.6)$$

The integration in Eq. 4.6 remains 1-dimensional as the hit points of the ellipses on each mirror lie on a straight line segment through the origin. This holds for excitation with the fundamental HG-mode only.

The transition from a summation to an integration is valid when the degeneracy N, the cavity finesse F, and the off-axis distance ρ are all sufficiently large to wash out the dependence on the phase $\theta_0/2$ within the transverse oscillations; equivalent to the washing out of the intermediate hit points on the ellipses. This is already the case for the ellipses forming the first fringe ($m = 1$) at exact degeneracy ($\varepsilon = 0$) as shown in Fig. 4.3.

Eq. 4.6 gives the formal link between the combined mirror height profile $h(\vec{r}) = h_1(\vec{r}) + h_2(\vec{r})$ and the deviation $\Delta L_{\text{tot}}(\vec{\rho})$, deduced by comparing the observed interferogram with that expected for ideal spherical mirrors. The inversion of this equation is simple in a Taylor expansion (see below). The integral form already provides for a few basic rules: (i) Only the symmetric part of the function $h(\vec{r})$ survives the (symmetric) integration from $r = -\rho$ to ρ. Any local bump or dip positioned at ρ_0 will show up both at $r = \rho_0$ and at $r = -\rho_0$ as the function $L_{\text{tot}}(\vec{\rho})$ is symmetric in ρ. (ii) The closed round-trip path length $L_{\text{tot}}(\rho)$ is sensitive only to height variations $h(r)$ at $|r| < \rho$. The denominator shows that height variations around $|r| \approx \rho$ have a large weighting factor, as these are the turning points of the transverse oscillation. (iii) The sensitivity of $L_{\text{tot}}(\rho)$ to local height variations $h(r)$, depends on the exact topography of these variations. This sensitivity is better than $\lambda/2$ as each mirror is hit N times during a closed orbit. It is, however, generally smaller than $\lambda/2N$ as the integration corresponds to averaging over the full mirror. The $\lambda/2N$ accuracy is reached only for global mirror deformation that are noticeable all over the mirror surface. The effects of global deformations are best evaluated through a Taylor expansion in position coordinates.

As a check on the validity of Eq. 4.6, we will compare two symmetric cavities, one with spherical mirrors of radii R and the other with mirrors of radii $R + \Delta R$. For this check, we note that the difference ΔL_{tot} in a N-fold round-trip length can be described by both the total path length (Eq. 4.1) and the difference in height profile (Eq. 4.6). The mentioned deformation from mirrors with a radius of curvature of R to $R + \Delta R$ is equivalent to a combined mirror height profile $h[r \cos(\phi), r \sin(\phi)] = -2 \times \frac{\Delta R}{2R^2} r^2$. Substitution of Eq. 4.6 yields a path length change $\frac{1}{2N} \Delta L_{\text{tot}}(\rho) = -\frac{\Delta R}{2R^2} \rho^2$. Alternatively, we can interpret the difference in radii as an extra detuning from the (now different) resonance length $\varepsilon = -\Delta R[1 - \cos(\theta_0/2)] = -\frac{\Delta R}{R} L_{\text{res}}$. Substitution into Eq. 4.1 gives the same path length change as before, which concludes our check.

The center and the outer region of Fig. 4.2b display almost circular fringes. In the intermediate region ($\rho \approx 1.04$ cm) the two patches below and above the injection beam originate from the birth of a "fourth" fringe, counting from the center. The appearance on only the vertical axis clearly demonstrates the presence of mirror astigmatism. The advantage of $\varepsilon < 0$ is that the path length of the N-fold round-trip first increases and then decreases as a function

of the radial distance ρ (see Fig. 4.5), which creates a pattern with a relatively large radial fringe spacing.

To quantify the relation between the interference pattern and the astigmatism of the mirrors, we take a closer look at the labelling of the fringes. The radial dependence of the round-trip path length makes the labelling of the fringes in the vertical direction of Fig. 4.2b, for increasing radial distance: $n = -1, -2, -3, -4, -4, -3, -2, -1, 0, 1, \ldots$. The patches of light labelled with $n = -4$ are thus clamped between the two fringes $n = -3$.

The occurrence of these patches shows that, for a radial distance $\rho = 1.70$ cm off-axis, the difference in the corresponding total round-trip path length is definitely less than two fringes ($\frac{1}{2N}(L_{\text{tot,x}} - L_{\text{tot,y}}) < 2\lambda/12$). This results in a first estimate of the astigmatism of $\Delta R/R < 6.1 \times 10^{-4}$.

We can also determine the astigmatism of the mirrors from the closed inner fringes. The ellipticity of the fringes indicates that the same L_{tot} is found for slightly different off-axis distances ρ. In Fig. 4.2b the ellipticity of fringe $n = -2$ is demonstrated by the tangent inner dotted circle. As the radii of the tangent inner and outer circles differ $(6\pm2)\%$ and the radii of the fringes $n = -2$ and $n = -3$ differ by 30% we conclude that the astigmatism at $\rho \approx 0.91$ cm corresponds to a *average* height difference of $[(6\pm2)/30]\lambda/2N = (9\pm3)$ nm or a relative difference in radii of $\Delta R/R = (2.0\pm0.7) \times 10^{-4}$.

The best estimate for the astigmatism is found from a fit of the experimental fringe positions in Fig. 4.7 by $m = a\rho^4 - b\rho^2$ similar to Eq. 4.1, where $a = 2NA/\lambda R^3$ and $b = 2NB\varepsilon/\lambda R^2$. By taking the spherical aberration rotationally symmetric over the mirror we obtain identical fit values $a_x = a_y = 4.80 \times 10^7$. The fitted b is 2.61×10^4 and 2.87×10^4 in the x- and the y-direction, respectively. From these fits we find that $\Delta R/R = (2.30\pm0.08) \times 10^{-4}$, so that the radii of curvature differ by $R_x - R_y = (115\pm4)$ μm for $R = 50$ cm. This corresponds to a height difference at $\rho = 1.7$ cm of (67 ± 2) nm or an average height difference of $0.75 \times \lambda/12$ fringe spacings.
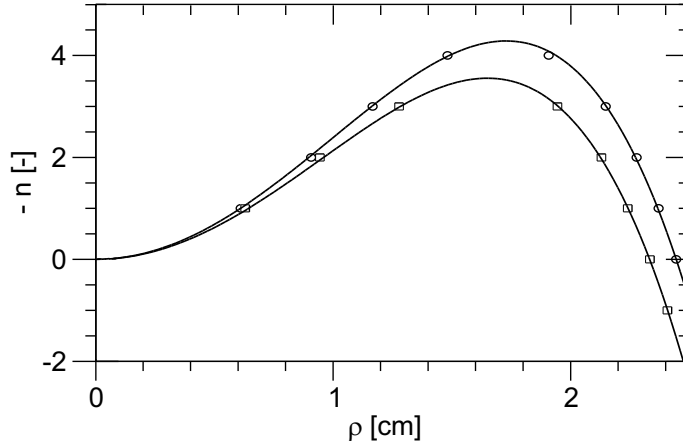

Figure 4.7: *The fringe number as a function of the fringe radius. The upper and lower curve correspond to cuts along the "long" and "short" symmetry axes of Fig. 4.2b.*

It is easy to increase the number of fringes even further by going to a higher-order de-

generacy. A relatively small change in the cavity length (6.70 to 6.28 cm) in fact suffices to go from the $K/N = 1/6$ degeneracy to the $mK/(mN + 1) = 5/31$ and thereby increase the number of fringes by roughly an integer factor $m = 5$. The resulting fringe pattern is shown in Fig. 4.8, where the cavity is tuned $\varepsilon \approx -93$ μm away from the degenerate point. The number of fringes in Fig. 4.8 is indeed roughly 5 times as large as in Fig. 4.2 and immediately shows the enhanced sensitivity to average height variations, *i.e.*, $\Delta L/N = \lambda/62$ (an extra fringe appears for every ~ 9 nm average height variation!).
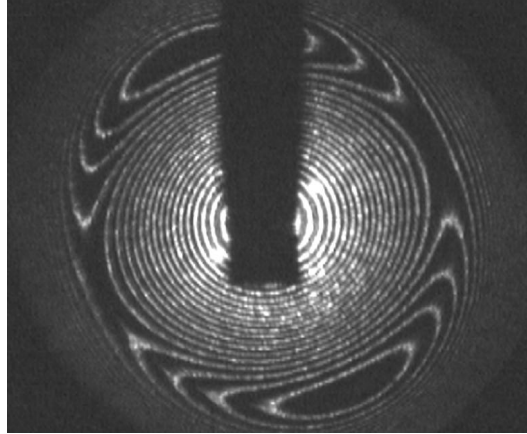
Figure 4.8: *The interference pattern for a degeneracy of $K/N = 5/31$. Due to the higher degeneracy more interference fringes are visible, with spacings corresponding to $\lambda/62$ height variations.*

For proper comparison of the simulated and measured fringe radii, as shown in Fig. 4.6, we have to correct for the diffraction over the distance between the second mirror, where the fringe radii are calculated, and the image-plane of the fringes (6 cm behind the cavity). The comparison of the theoretical and experimental a fitted in Fig. 4.9 can be used for this scaling. As a scales with $1/\rho^4$ (see Eq. 4.1), the magnification of the experimental fringe radii as compared to the theoretical fringe radii ($\rho_{\mathrm{meas}}/\rho_{\mathrm{th}}$) scales with $(a_{\mathrm{th}}/a_{\mathrm{meas}})^{1/4} = (7.97 \times 10^{-4}/4.8 \times 10^{-4})^{1/4} = 1.14\times$. The spatial evolution of the fringe radii due to diffraction inside and outside the resonator (Fig. 4.9) provides us with the same scaling: $1.15\times$.

Finally, we compared the results obtained with our new fringe method with an aberration analysis with a commercially available standard phase-stepped Fizeau interferometer [51–53] (Wyko 400) on which we tested two identical mirrors. The interferograms showed no separated fringes apart from the ones produced by defocus. The phase-stepping technique allowed us to quantify the peak-to-peak height deviation of the individual mirrors, as compared to the spherical reference mirror, to be less than 90 nm within the central aperture of radius $\rho = 1.5$ cm. The astigmatism of each mirror was less than 40 nm peak value in this aperture. Although the values for the astigmatism we found with our fringe method depend on the mutual orientation of the mirrors, the order is comparable with values found with the Fizeau interferometer [51–53].
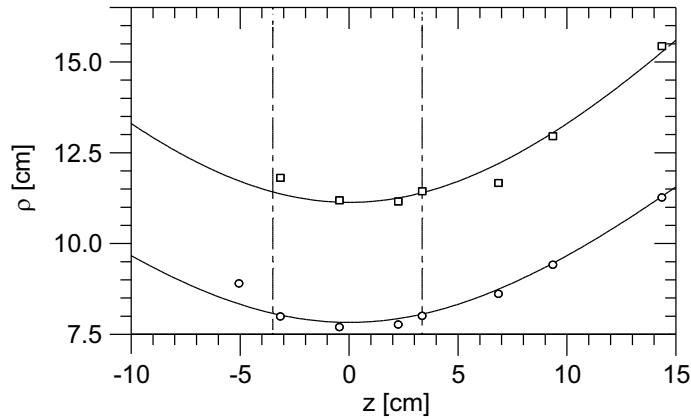
Figure 4.9: *The measured and fitted radii of two fringes for various positions inside and outside the resonator. The dashed-dotted lines represent the mirrors of the resonator.*

4.5 Applications

The described *multi*-beam resonator method may be useful for the accurate inspection of the global aberrations of *single* mode resonators. This may sound surprising, since the cavity length and mirror radii of a single-transverse resonator are such that higher-order transverse modes experience sizeable losses. To study the aberrations in these cavities, we propose to greatly reduce the cavity length, so as to use them in the *multi*-transverse-mode regime. When we then operate the cavity around a higher-order degenerate point with on-axis injection, resonant trapping of scattered light should again produce interferograms like Fig. 4.2. In essence, by greatly shortening the cavity length L and thus increasing the Fresnel number, $N_F = a^2/\lambda L$ [12], where a is the mirror radius and λ the wavelength, we may visualize the resonator aberrations.

An example of a single-mode resonator, where aberrations are a key issue, is the LIGO interferometric gravitational wave detector. The mirrors used in these resonators have to meet very stringent requirements (order $\lambda/2000$ for $R = 7$ km mirrors [7]). Currently, a null wave-front interferometer is used to measure the aberrations of the mirrors. The disadvantage of this method is the required stability for full aperture testing, and the limited aperture capability, where the evolution of LIGO is toward mirrors with even larger radii [54]. Fabrication of such surfaces is a difficult process and our multi-pass method could provide a rapid, full surface scanning of such mirrors, although the limited Finesse of the LIGO interferometer ($F \sim 210$) is still a practical limitation of our method.

4.6 Concluding remarks

We have demonstrated and discussed the formation of fringes in the interference patterns observable around frequency-degenerate cavity lengths. These fringes are the vertices of light that is scattered into closed orbits and resonantly trapped inside the resonator. From this

mechanism we have generalized the total round-trip path length for arbitrary $1/N$ degenerate points. Finally, we have shown how the observed interference pattern can be used for visualization and quantification of cavity aberrations, and possibly applied for testing the mirrors used in gravitational wave detectors.

Appendix (unpublished material)

4.A   Calculation of the total path length

In this Section, the derivation of the total path length in an arbitrary frequency-degenerate cavity ($N > 2$) will be discussed in more detail. We start out calculating the length L of a single pass ray, connecting the hit points on the mirrors P_1 and P_2, as shown in Fig. 4.10. We normalize all (positions and) distances by the identical mirror radii R. The normalized on-
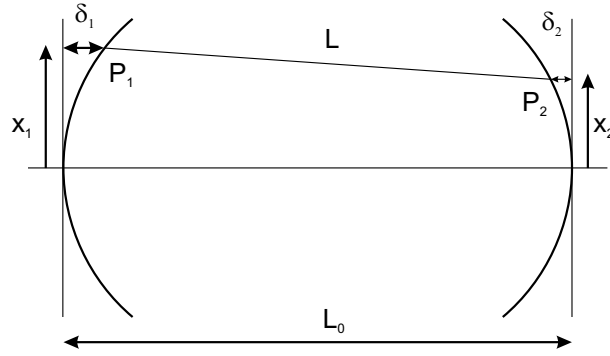
Figure 4.10: *Schematic representation of a ray with a length L connecting the hit points P_1 and P_2 in a frequency-degenerate two-mirror resonator with a cavity length L_0.*

axis cavity length of the frequency-degenerate cavity is $L_0 = L_{\text{res}}/R = 1 - \cos(\theta_0/2)$, where $\theta_0 = 2\pi K/N$ is the round-trip Gouy phase. The (horizontal) distance between the hit points on the mirror and the reference plane is denoted δ.

The length of the ray connecting P_1 and P_2 is given by

$$L = \sqrt{(L_0 - \delta_1 - \delta_2)^2 + (x_2 - x_1)^2} = (L_0 - \delta_1 - \delta_2)\sqrt{1 + \left(\frac{x_2 - x_1}{L_0 - \delta_1 - \delta_2}\right)^2}. \qquad (4.7)$$

In the paraxial limit ($x_1, x_2 \ll L_0$), Eq. 4.7 becomes

$$L \approx (L_0 - \delta_1 - \delta_2) + \frac{(x_2 - x_1)^2}{2(L_0 - \delta_1 - \delta_2)} - \frac{(x_2 - x_1)^4}{8(L_0 - \delta_1 - \delta_2)^3}. \qquad (4.8)$$

Using a Taylor expansion of δ_1 and δ_2 up to the fourth order, *i.e.*,

$$\delta_{1,2} = 1 - \sqrt{1 - x_{1,2}^2} \approx \frac{x_{1,2}^2}{2} + \frac{x_{1,2}^4}{8}, \qquad (4.9)$$

41

we find for Eq. 4.8

$$L \approx L_0 + \frac{(x_2 - x_1)^2}{2L_0} - \frac{x_1^2 + x_2^2}{2} - \frac{x_1^4 + x_2^4}{8} + \frac{(x_2 - x_1)^2(x_1^2 + x_2^2)}{4L_0^2} - \frac{(x_2 - x_1)^4}{8L_0^3} . \qquad (4.10)$$

We will use this expression to calculate the total path length L_{tot} of a closed orbit in a frequency-degenerate cavity. To do so, we decompose this orbit in $2N$ single passes via $L_{\text{tot}} = \sum_{n=0}^{2N-1} L_{n,n+1} = 2N \langle L_{n,n+1} \rangle$. Using Eq. 4.10, the average path length $\langle L_{n,n+1} \rangle$ for a ray connecting two hit points x_n and x_{n+1} can be written as

$$\begin{aligned} \langle L_{\text{n,n+1}} \rangle \quad \approx \quad & L_0 + \frac{\langle (x_{n+1} - x_n)^2 \rangle}{2L_0} - \frac{\langle x_n^2 + x_{n+1}^2 \rangle}{2} - \frac{\langle x_n^4 + x_{n+1}^4 \rangle}{8} \\ & + \frac{\langle (x_{n+1} - x_n)^2 (x_n^2 + x_{n+1}^2) \rangle}{4L_0^2} - \frac{\langle (x_{n+1} - x_n)^4 \rangle}{8L_0^3} . \end{aligned} \qquad (4.11)$$

For x_n, the unaberrated positions of the hit points are used, found from $x_n = \rho \sin(n\theta_0/2 + \phi_0)$. The eventual extra phase factor ϕ_0 determines the type of orbit, *e.g.*, V-shaped or bow-tie. The relation $x_n = \rho \sin(n\theta_0/2 + \phi_0) = \rho \{ \exp[i(n\theta_0/2 + \phi_0)] - \exp[-i(n\theta_0/2 + \phi_0)] \}/2i$ helps us to simplify Eq. 4.11. Furthermore we use the relation $\langle \exp[i(n\theta_0/2 + \phi_0)] \rangle = 0$, which holds in the case of frequency-degeneracy, where the values $n\theta_0/2$ are equally distributed over the "unit circle" $[0, 2\pi)$. Cycle averages of other powers of x_n and x_{n+1} are calculated by reexpressing products of exponents into sums of exponents with combined arguments followed by a similar cycle average, *e.g.*, $\langle x_n^2 \rangle = \rho^2 \langle \frac{1}{2} + \frac{1}{2} \exp[i(n\theta_0 + 2\phi_0)] \rangle = \rho^2/2$. We note that the phase factor ϕ_0 drops out of all these averages. This means that the total path length for an arbitrary degeneracy ($N > 2$) is independent of the type of orbit. Application of both ideas on the individual terms of Eq. 4.11 results in

$$\langle (x_{n+1} - x_n)^2 \rangle = \rho^2 [1 - \cos(\theta_0/2)] , \qquad (4.12)$$
$$\langle x_n^2 + x_{n+1}^2 \rangle = \rho^2 , \qquad (4.13)$$
$$\langle x_n^4 + x_{n+1}^4 \rangle = \tfrac{3}{4} \rho^4 , \qquad (4.14)$$
$$\langle (x_{n+1} - x_n)^2 (x_n^2 + x_{n+1}^2) \rangle = \rho^4 \{ \tfrac{1}{2} [\cos(\theta_0/2) - \tfrac{3}{2}]^2 - \tfrac{1}{8} \} , \qquad (4.15)$$
$$\langle (x_{n+1} - x_n)^4 \rangle = \tfrac{3}{2} \cos(\theta_0/2)^2 - 3\cos(\theta_0/2) + \tfrac{3}{2} . \qquad (4.16)$$

Substitution of Eqs. 4.12–4.16 into Eq. 4.11 finally results in Eq. 4.1, which reads

$$\frac{1}{2N} L_{\text{tot}}(\rho) = (L_{\text{res}} + \varepsilon) - B\varepsilon \frac{\rho^2}{R^2} - A\frac{\rho^4}{R^3} , \qquad (4.17)$$

where

$$A = \frac{1 + \cos(\theta_0/2)}{32[1 - \cos(\theta_0/2)]} = \frac{2R - L_{\text{res}}}{32L_{\text{res}}} \quad \text{and} \qquad (4.18)$$

$$B = \frac{1}{2} \left[\frac{1}{1 - \cos(\theta_0/2)} \right] = \frac{R}{2L_{\text{res}}} . \qquad (4.19)$$

4.B   Evolution of fringes around frequency-degeneracy

For a better understanding of Eq. 4.5, as depicted graphically for $N = 6$ in Fig. 4.6, we discuss here a number of corresponding fringe patterns on the mirror. The intensity profiles for various distances ε away from the exact frequency-degenerate point $N = 7$ are shown in Fig. 4.12. The cavity detuning ε is increased stepwise by 5 μm from $\varepsilon = -55$ to 20 μm. To prevent redundancy, not all pictures out of this series are shown in Fig. 4.12. The astigmatic axis are prominently visible in, a.o., images 1 and 4. The disappearance of the fringes $m = -2, -1$, and 0 can be observed between the images $1 - 2$, $4 - 5$, and in the series of $9 - 12$, respectively. At these points, the transmitted power is redistributed over the mirror. This is shown in Fig. 4.11, where we obscured the on-axis transmitted power and measured the off-axis power as a function of ε. We observe increased transmission exactly at these points, denoted $1, 4$, and 9. The radii of the disappearing fringes correspond to $\partial L_{\text{tot}} / \partial \rho = 0$ found from Fermat's principle (see Chapter 6). For those trajectories, the interference of the scattered light is maximally constructive, and the light is "resonantly trapped".
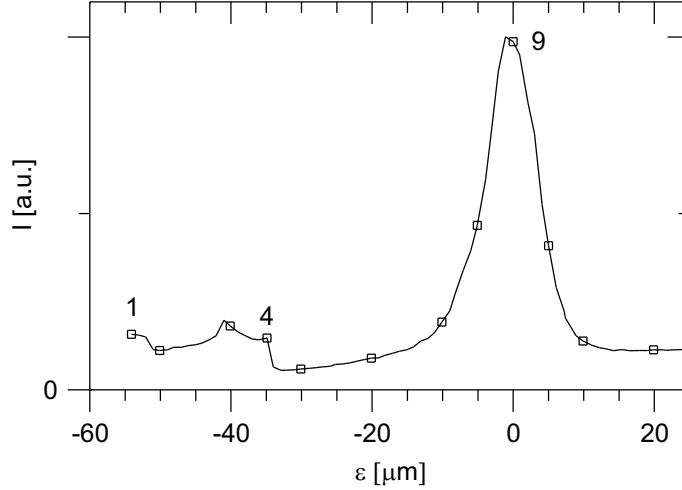
Figure 4.11: *The transmitted power outside the on-axis beam as a function of the cavity detuning. The labelling corresponds to Fig. 4.12. Images 1, 4, and 9 show an increase of the transmitted power (outside the optical axis), corresponding to the "birth" of the fringes $m = -2, -1$ and 0, respectively. The length detuning from image 1 to 4 nicely corresponds to the difference found in the simulations and measurements.*
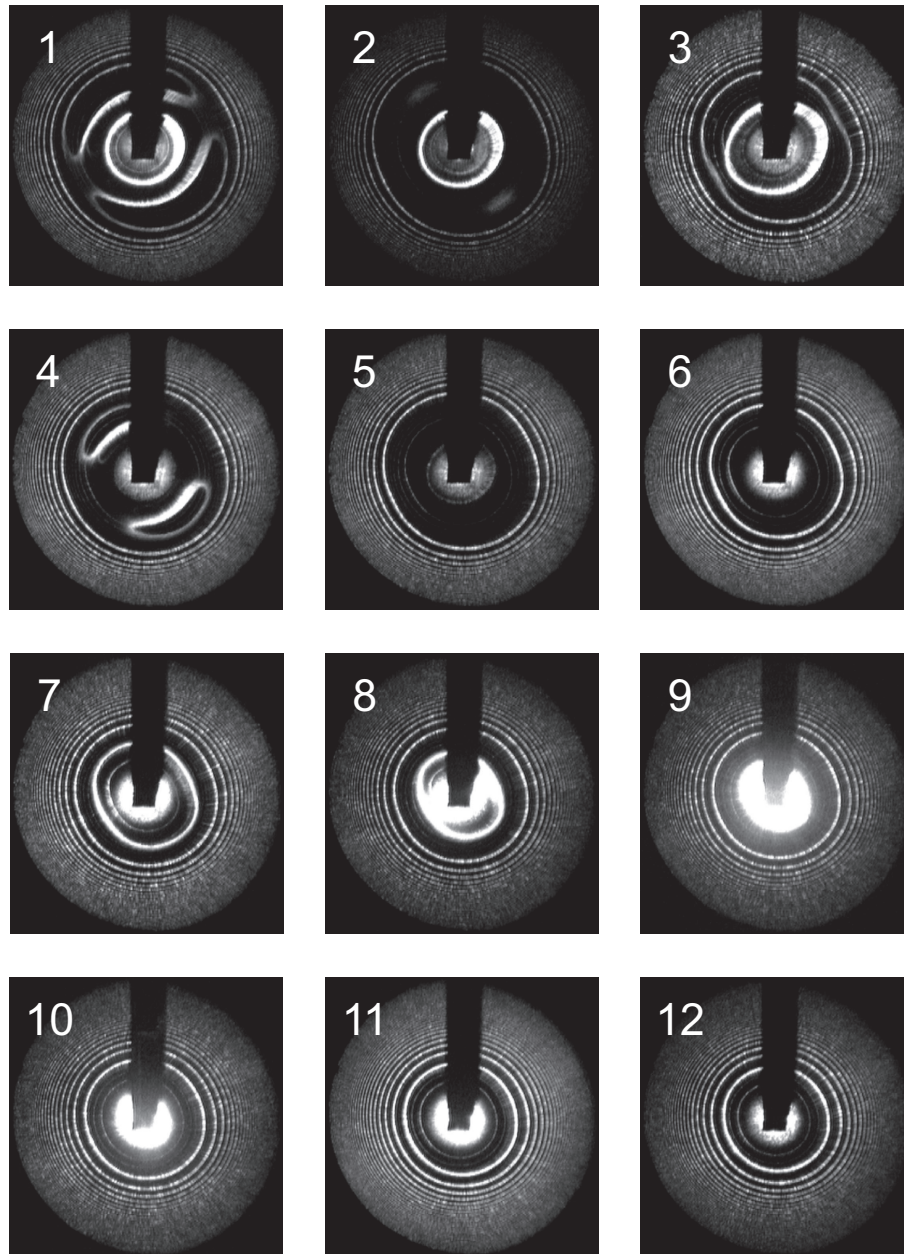
Figure 4.12: *Intensity profiles over the full mirror aperture (diameter 5 cm) around the 7-fold frequency-degeneracy point (N = 7) from ε = −55 (Image 1) to 20 μm (Image 12) in steps of 5 μm (Images at ε = −45, −25, −15 μm and −15 μm are left out). Image 9 represents the fringe pattern at exact frequency-degeneracy (ε = 0) and shows the birth of the m = 0-fringe. To prevent the pictures from overexposure the on-axis beam is blocked.*

Gouy phase of nonparaxial eigenmodes in a folded resonator

We study the effect of nonparaxiality in a folded resonator by accurate measurements of the Gouy phase, as function of the mode number for mode numbers up to 1500. *Our experimental method is based upon tuning the resonator close to a frequency-degenerate point. The Gouy phase shows a nonparaxial behavior that is much stronger in the folding-plane than in the perpendicular plane. Agreement with ray-tracing simulations is established and a link with aberration theory is made.*

5.1 Introduction

Our interest is in the spectrum of a folded (3-mirror) optical resonator; this is stimulated by the fact that Dingjan *et al.* [55] have recently found a signature of wave chaos in such a resonator. Generally, to obtain wave chaos, a minimum requirement is that the wave equation describing the system is nonseparable. This can be achieved by making the numerical aperture of the resonator relatively large, *i.e.*, going beyond the paraxial regime. Since in this regime aberrations occur, it is natural to look for a connection between the basic concept of a paraxial resonator, namely its Gouy phase, and optical aberration theory. In the present Chapter, we make this connection by extending the concept of the Gouy phase, which is essentially a paraxial concept, into the nonparaxial domain where optical aberrations form the more natural concept. Our approach is mainly experimental; it is based on accurate measurements of the Gouy phase, being the diffraction-induced phase delay of a finite-diameter focused beam as compared to a plane wave. By measuring this phase difference for transverse modes up to very high mode numbers (beyond paraxiality), we can obtain quantitative information on the optical aberrations in the cavity. In principle, a connection with standard lens aberration theory can be made by realizing that the optical cavity (a folded one in our case) is equivalent to a periodic lens guide [12]. However, this comparison is hampered by the fact that we deal with a highly unusual series of lenses as shown in Fig. 5.8b below (periodic; relatively large separations; strongly astigmatic elements), which does not appear in the literature on lens aberrations.

In Section 5.2, we introduce the theory of the Gouy phase. The experiment is described in Section 5.3 and the experimental results are discussed in Section 5.4. In Section 5.5, we present ray-tracing calculations and compare them with the experimental results. The results are explained using aberration theory in Section 5.6 and we summarize our work in Section 5.7.

5.2 Gouy phase theory

The Gouy phase is an essential ray- and wave-property of optical resonators [12, 21, 46]; it plays an important role in determining the position and slope of the intra-cavity rays and the spectral properties of the modes. These modes can be chosen as Hermite-Gaussian eigenmodes with eigenfrequencies

$$\nu_{q,nm} = \frac{c}{2L}\left[q + (m+n+1)\frac{\theta_0}{2\pi}\right] , \tag{5.1}$$

where θ_0 is the Gouy phase, L the length of the cavity and q, n and m are the longitudinal and transversal mode numbers, respectively. Throughout this Chapter, we choose $n = 0$ as we excite in the experiment discussed below only a set of 1-dimensional modes. The longitudinal mode spacing is called the free spectral range: $\Delta \nu_{\mathrm{FSR}} = c/2L$. Frequency-degeneracy occurs when the Gouy phase is equal to a rational fraction of 2π, $\theta_0 = 2\pi K/N$. In the ray picture, N longitudinal round-trips are then needed before the ray returns on itself [21], and K is the number of transverse "round-trips" an orbit makes before closing; in all our experiments, we use a resonator configuration that yields $K = 1$. The frequency-degenerate eigenfrequencies
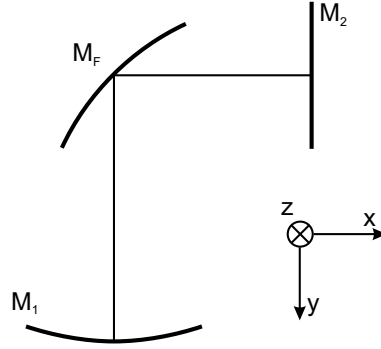
Figure 5.1: *The folded 3-mirror resonator and its orientation.*

in the spectrum are thus

$$\nu_{q,m0} = \frac{c}{2LN} \left[Nq + (m+1) \right] , \tag{5.2}$$

which implies that when we raise m by N and at the same time lower q by 1 that $\nu_{q,m}$ and $\nu_{q-1,m+N}$ are the same. The spectrum collapses into N "clumps" of modes.

For the fundamental Gaussian mode, the Gouy phase θ_0 is defined as the round-trip phase delay ψ_0 between this mode and a plane wave. Higher-order TEM$_{m0}$ modes experience a larger phase delay ψ_m as compared to the reference plane wave; in the paraxial regime, we have simply $\psi_m \equiv (m+1)\theta_0$ [12]. In the nonparaxial regime, we can similarly define an m-dependent Gouy phase θ_m via $\theta_m = (\psi_m - \psi_0)/m$. Any m-dependence of θ_m, *i.e.*, any change in Gouy phase as a function of the mode number, is equivalent to the presence of aberrations with respect to paraxiality.

Next, we consider a folded 3-mirror resonator, with a folding angle of, *e.g.*, 90°, and a *spherical* folding mirror (Fig. 5.1); note that when using a *planar* folding mirror, the folded 3-mirror cavity is trivially equivalent with a two-mirror cavity. Already in the paraxial regime, the effective power of the folding mirror in the *xz*-principal plane is different from the effective power in the *y*-principal plane. This trivial form of astigmatism causes that *two* Gouy phases are needed to describe the resonator. The same degeneracy N requires different lengths of the resonator in the *xz*-principal plane and the *y*-principal plane.

In the nonparaxial regime, the folding mirror affects the magnitude of the aberrations in both planes of the folded resonator. The modes in the *y*-principal plane will hardly feel the aberrations of the folding mirror. In contrast, the modes in the *xz*-principal plane, will undergo the full effect of the aberrations introduced by the folding mirror; these will be stronger than in the case of a two-mirror resonator.

Since we operate close to frequency-degeneracy, the Gouy phase θ_m for an arbitrary mode m (integer multiple of N) can be written as

$$\theta_m = \frac{2\pi}{N} + \Delta\theta_m , \tag{5.3}$$

where θ_m is the Gouy phase and $\Delta\theta_m$ parametrizes how close the spectrum is to degeneracy. A generalization of Eq. 5.1, along the lines described above, using $\theta_m = (\psi_m - \psi_0)/m$, shows

that $\Delta\theta_m$ can experimentally be found from

$$\Delta\theta_m = \frac{2\pi}{\Delta\nu_{\text{FSR}}} \frac{\Delta\nu_m}{m} \; , \tag{5.4}$$

where m is the transverse mode number, $\Delta\nu_m$ is the frequency difference of the fundamental mode and mode m, and $\Delta\nu_{\text{FSR}}$ is the free spectral range.

5.3 Experiment

Our folded optical resonator (Fig. 5.1) consists of three highly reflective mirrors (nominal specification $R > 99.995\%$). The folding angle is $90°$, the radii of curvature of mirror M_1 and M_F are 1 m, mirror M_2 is planar, and all mirrors have a diameter of 2.5 cm. Fig. 5.2 shows the complete experimental setup. The length of arm A_2 is 1.2 cm, the length of arm A_1 is variable. We probe the transmission of the resonator with a beam at a wavelength of 532 nm, produced by a frequency-doubled single-mode Nd:YAG laser. The beam is sent to the resonator via lens L_1, enters the cavity through mirror M_1 (here the beam diameter is ~ 0.5 mm) and excites the Hermite-Gaussian modes of the cavity. The focal length of lens L_1 equals distance A_3, so that the (dotted) beam is injected parallel to the optical axis, independent of the rotation-angle of mirror M_3. This allows us to vary Δr, the off-axis position of injection on mirror M_1, independent of the angle of injection. We inject in the xz-principal plane or in the y-principal plane in order to excite only 1-dimensional TEM$_{m0}$ or TEM$_{0m}$ modes. Exciting a limited set of modes makes labelling of the modes easier and allows us to measure closer to degeneracy. The spectrum is obtained from the spatially integrated throughput as a function of the cavity length, by scanning the position of mirror M_1 with a piezo-element. Judging from these spectra, we estimate the finesse of the cavity as ~ 5600 for low-order modes and ~ 5000 for high-order modes. This is considerably smaller than the value of the finesse allowed by the mirror reflectivities ($> 99.995\%$). We attribute this discrepancy mainly to scattering due to polishing errors of the mirrors.

The length L of the cavity is varied by changing the length of arm A_1; this length is chosen such that the spectrum is almost N-fold degenerate resulting in N "clumps" of modes (see Fig. 5.3). Fig. 5.4 shows a detail of the modes within the "fundamental" clump. The mode number difference of subsequent modes is N. The transverse mode numbers of the modes within this clump are thus labelled $m = lN$, where $l = 0, 1, 2$, etc.

The closeness to degeneracy is illustrated by the typical distance between subsequent peaks $\Delta\nu_N / \Delta\nu_{\text{FSR}} \approx 1 \times 10^{-3}$, where $\Delta\nu_N$ is the distance between mode $m = 0$ and mode N and $\Delta\nu_{\text{FSR}}$ is a free spectral range. Higher-order modes are therefore still relatively close to the $m = 0$ mode so that the effect of vibrations on the time scale of the piezo scan is limited (we scan typically over $\Delta\nu_{\text{FSR}}$ in ~ 22 ms). Specifically, for a frequency range $\Delta\nu_{\text{FSR}}/16$ ($m \approx 500$)), the measured vibration-induced fluctuations in $\Delta\nu/\Delta\nu_{\text{FSR}}$ are of the order 3×10^{-4}. This is acceptable as in our range of mode numbers (m up to 1500) the modes can still be labelled uniquely, ($3 \times 10^{-4} < 1 \times 10^{-3}$).

To find the Gouy phase as a function of mode number, a set of $15 - 25$ spectra is measured for increasing off-axis position of injection, Δr. Every time the off-axis distance of the beam is increased, a different clump of peaks containing higher-order Hermite-Gaussian modes is
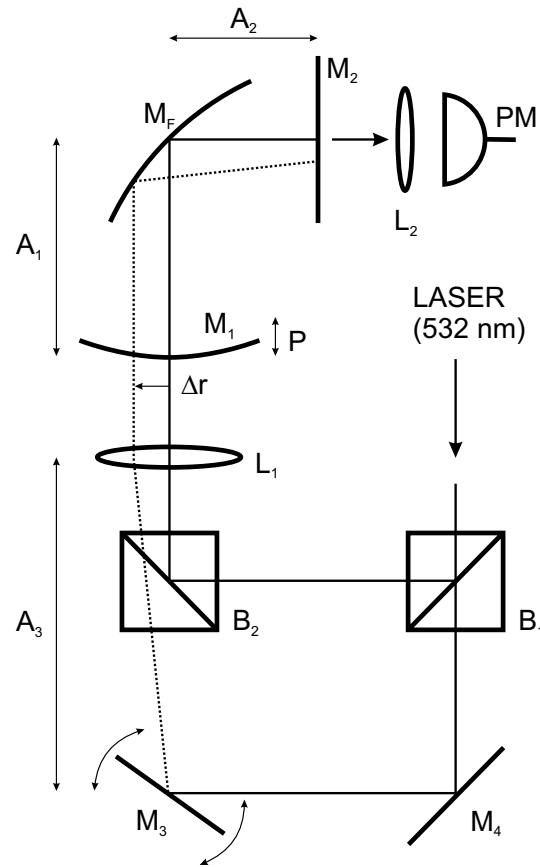
Figure 5.2: *Overview of the setup, where the mirrors M_1, M_F and M_2 form the folded resonator. A_1, A_2: lengths of resonator arms, PM: photomultiplier, L_1, L_2: lenses, B_1, B_2: beamsplitters, M_3, M_4: mirrors. The solid line indicates the fixed beam which excites the fundamental mode. The position of the other (dotted) beam on mirror M_1 can be increased by rotating M_3 to excite higher-order modes.*

excited. Starting from the on-axis position, the position of injection is increased stepwise such that the spectra of successive measurements overlap. Finally, a second beam is always injected into the resonator to excite only the fundamental ($m = 0$) mode. The presence of this reference mode, in the set of overlapping spectra, allows for a unique labelling up to transverse mode numbers $m \approx 1500$.

5.4 Experimental results

For every transverse mode m, the frequency difference $\Delta \nu_m$ is measured and this is transformed to a round-trip Gouy phase by using Eq. 5.4. For several degenerate configurations ($N = 7$, 8, and 9), the change of the Gouy phase as a function of the mode number has thus
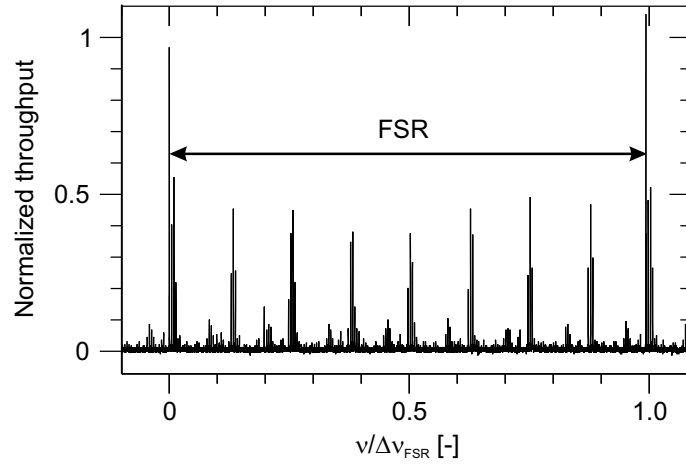
Figure 5.3: *Spectrum for an almost 8-fold degenerate cavity configuration. The modes collapse into 8 clumps of peaks. The two highest peaks are due to the fundamental mode, which serves as a reference.*
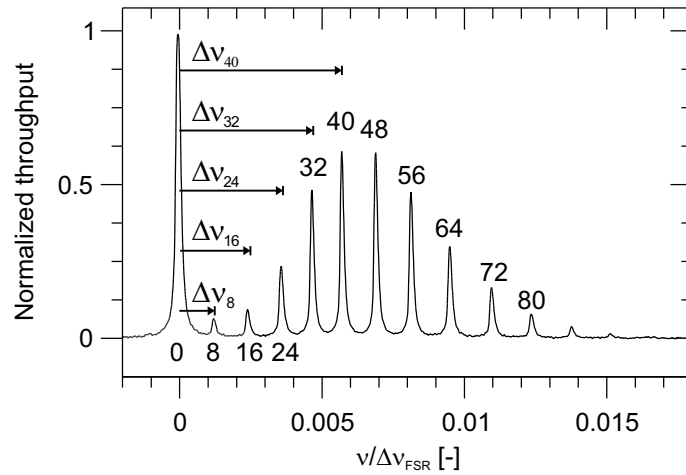
Figure 5.4: *Spectral detail of the fundamental mode and the nearest clump of peaks. The almost 8-fold degeneracy makes the difference in mode number between two subsequent modes equal to 8. $\Delta\nu_m$ is the distance between the fundamental mode $m = 0$ and mode m.*
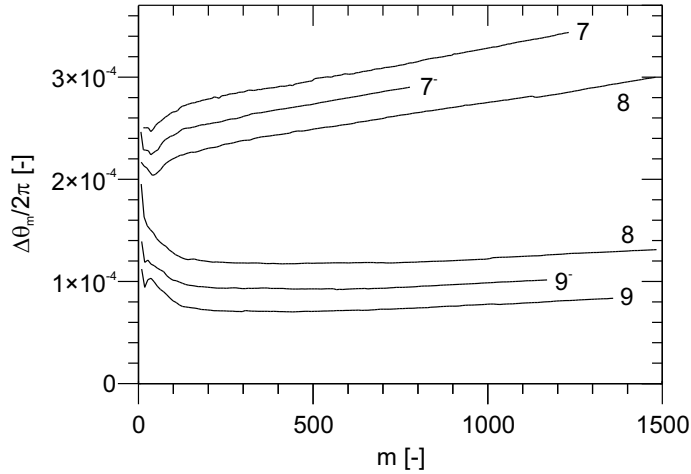
Figure 5.5: *$\Delta\theta_m$ vs. mode number m for various values of N. The upper three curves are measured in the xz-principal plane, the lower ones in the y-principal plane. For easy comparison all curves have been vertically shifted by an arbitrary amount to bring them closer to each other; the N^- indicates an originally negative valued $\Delta\theta_m$.*

been determined. Fig. 5.5 shows the measured value of $\Delta\theta_m/2\pi$ as a function of the transverse mode number m. The three top curves show this dependence for displacements of the injected beam in the xz-principal plane (for orientation see Fig. 5.1), at three different but fixed cavity lengths, corresponding to degeneracy near $N = 7$, somewhat below 7 (denoted 7^-) and near $N = 8$. The three bottom curves show this dependence for displacements in the y-principal plane for $N \simeq 8, 9^-$ and 9. As only the *change* of $\Delta\theta_m$ with m is important, a suitable vertical offset has been added to the various curves to allow better comparison.

The change of $\Delta\theta_m$ with m is a nonparaxial effect that corresponds with the onset of aberrations. For $N = 8$ in the xz-principal plane, $\Delta\theta_m/2\pi$ increases with 0.7×10^{-4} when going from for low m-values to $m \approx 1200$. In this region, $\Delta\theta_m/2\pi$ changes in the y-principal plane with only 0.1×10^{-4}. We thus find almost an order of magnitude stronger aberrations in the xz-principal plane than in the y-principal plane. We attribute this key result to the fact that modes in the y-principal plane will hardly feel the aberrations due to the folding mirror, M_2, in contrast to the modes in the xz-principal plane.

Varying the degree of degeneracy, N changes the position and angle of incidence at which the rays hit the optical elements. On this basis, one could expect that the change of the Gouy phase depends on N. More detailed inspection of Fig. 5.5 shows first of all that the Gouy phase is practically independent of the odd/even nature of the number of hit points, N, on the mirrors. Secondly, $\Delta\theta_m$ shows a strange wiggling for the lower-order mode numbers, $m = 0$ up to 150. A likely explanation for this phenomenon is in the surface polishing errors of the mirrors [56]. These imperfections are expected to affect the lower-order modes much stronger than the higher-order ones, as the latter have larger transverse mode sizes and should thus smooth out local errors in the shape of the mirrors.

In order to enable a comparison of the experiment with ray-tracing simulations (see Sec-
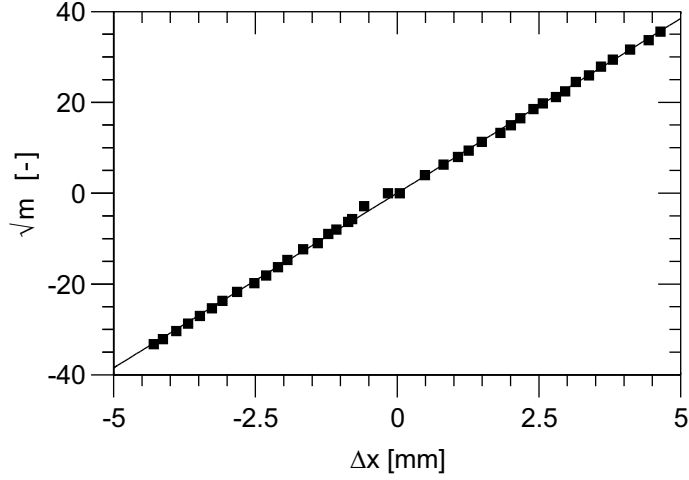
Figure 5.6: *The square root of the mode number vs. the off-axis distance of injection on mirror M_1.*

tion 5.5), we have measured the relation between the dominantly excited mode number and the off-axis injection distance. The experimental result for $N = 8$ is shown in Fig. 5.6, where the negative/positive square roots of the mode numbers refer to injection on the right/left side of the marker mode on mirror M_1. The linear fit was used to determine both the slope and the $\Delta x = 0$ point. Paraxial theory predicts that the mode number changes approximately quadratically with the ratio of the off-axis distance and the waist of the fundamental Gaussian mode w_0: $m \sim (\Delta r/w_0)^2$ [12]. The fitted curve shows that this paraxial dependence is not yet violated in our folded cavity; this is in accordance with the results of Laabs [57] for a two-mirror cavity.

5.5 Comparison with ray tracing

Since the Gouy phase is also a ray-optical property, it can be calculated by means of a ray-tracing program. We did this for a ray that is injected parallel to the optical axis from a certain off-axis distance Δr through the folded resonator, configured close to degeneracy N. The positions of the ray on the first (injection) mirror are calculated exactly for $n = 10^4$ round-trips. As shown in Herriot *et al.* [21] the hit points x_n on the mirror are given by

$$x_n = \Delta r \cos[n\theta(\Delta r)] , \tag{5.5}$$

where Δr is the off-axis distance of injection. This allows us to calculate the Gouy phase $\theta(\Delta r)$ from the 10^4 points x_n, with an accuracy of approximately 10^{-6} rad.

The results of calculations for an $N = 8$ and 9 three-mirror cavity are depicted in Fig. 5.7, which displays $\Delta\theta/2\pi$ as a function of the off-axis distance of injection, Δr. The calculations show that the Gouy phase is not a constant but increases with Δr. Furthermore, the Gouy phase changes much stronger for increasing displacements in the *xz*-principal plane than in the *y*-principal plane; we compare this now with the experimental results.
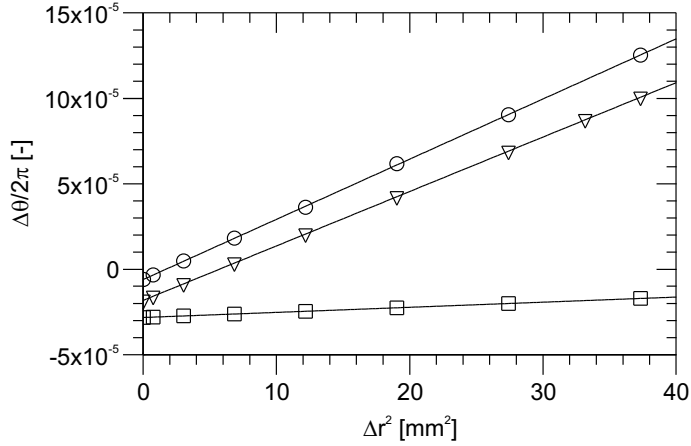
Figure 5.7: *Ray-tracing calculations of $\Delta\theta$ vs. the square of the off-axis distance (xz-principal plane) of injection for $N = 8$ (triangles) and 9 (circles) and in the y-principal plane for $N = 9$ (squares).*

For injection in the *xz*-principal plane (Δr becomes Δx) the calculated slope $\Delta\theta_m/(\Delta x)^2$ for $N = 8$ is 1.97×10^{-5} rad/mm^2. To compare this to the experiment we take the linear fit of the measured data for $N = 8$ (Fig. 5.5) which is converted from mode number to off-axis distance of injection, using Fig. 5.6. This results in an experimental slope $\Delta\theta_m/(\Delta x)^2 = 2.00 \times 10^{-5}$ rad/mm^2. The excellent agreement between theory and experiment validates our mapping from ray to wave dynamics.

To put these numbers in perspective, we consider the specific case of injection at $\Delta x = 5$ mm, which excites a group of modes around mode number $m = 1500$. From the slope given above, this produces a (nonparaxial) change of the Gouy phase $\Delta\theta_m$ by $\sim 5 \times 10^{-4}$ rad as compared to the paraxial values θ_0. Although this number is small, it can be measured relatively easily in our system because the shift in resonance frequency of a mode is proportional to $m\Delta\theta_m \approx 0.75$ rad $\approx 0.12\, \Delta v_{FSR}$ in the considered case. This is easily observable in our high-finesse cavity.

For a better understanding of the strength of the aberrations in the folded resonator, we have also studied a two-mirror cavity, both experimentally and theoretically. In this case, we choose two mirror radii of 1 m and a cavity length L of ~ 8 cm, which corresponds to a degeneracy near $N = 8$. Due to the absence of astigmatism, we observed a strong coupling between the horizontal and vertical modes, which made the measurement less accurate. Experimental results show that the change in $\Delta\theta_m/2\pi$ is less than 3×10^{-5} up to $m \approx 1000$. The calculation of the Gouy phase, which, in the present case, is more accurate than its measurement, shows a small increase of the Gouy phase for increasing mode numbers. The slope of the calculated Gouy phase as a function of the off-axis distance on the first mirror is 1.3×10^{-6} rad/mm^2, which is equivalent to $\Delta\theta_m/2\pi = 5 \times 10^{-6}$ for $m \approx 1000$.

5.6 Comparison with aberration theory

In a general optical system with a given object plane, the number of third-order aberrations depends on the symmetry of the system and is at most 20 [58]. For a rotationally symmetric system, like a cavity consisting of two spherical mirrors, the number of independent aberration coefficients is reduced to only 5, also known as the Seidel aberrations, being: spherical aberration, coma, astigmatism, curvature of field and distortion (see a.o., [14]). An aberration can be expressed in two ways: as a deviation from a reference wave front in the exit pupil (wave aberration) or as a displacement from the image point in the image plane (ray aberration). A ray-aberration is the spatial derivative of the corresponding wave-aberration; the wave aberrations are fourth-order and the ray-aberrations are third-order in the spatial coordinates (see a.o. [59]). In the literature, an aberration is usually indicated by the order of the ray-aberration.

The comparison of our experimental results with standard optical aberration theory is hampered by the fact that aberrations in a round-trip cavity, or in the equivalent periodic lens guide, are hardly discussed in the literature. Furthermore, our 3-mirror folded (not to be confused with the terminology "folded/unfolded" in the context of equivalent periodic lens guides [12]) resonator does not fall in the usual category of rotational symmetric systems, for which the standard Seidel aberrations apply. In this largely unchartered territory, we will rely on some general arguments, which are necessarily of a qualitative nature.

To link the observed nonparaxial behavior with aberration theory, we consider the two principal planes of the equivalent lensguide, one that is orthogonal to the folded axis (Fig. 5.8a) and one that contains the folded axis (Fig. 5.8b). In the former case (*y*-principal plane), the mirror symmetry, demonstrated in Fig. 5.8a, makes that the lowest nonvanishing aberrations are the usual third-order aberrations. In fact, we find the magnitude of the aberrations in the *y*-principal plane of the folded resonator to be of the same order for the folded resonator as for a regular two-mirror resonator. However, this symmetry is absent in the *xz*-principal plane. Fig. 5.8b shows how the folding mirror can be represented in corresponding lens guide by alternating forward- and backward-tilted lenses. The aberrations in the *xz*-principal plane are therefore potentially much stronger as they also contain second-order terms [60, 61].

However, due to the *periodic* nature of our (round-trip) optical system, one can show, that these second-order terms average out. To perform this averaging, we should add the aberrations over consecutive round-trips, preferably by expressing them in special "scaled variables" that are invariant under paraxial propagation [14]. For ray-aberrations, this rewrite comprises a multiplication with oscillating terms of the form $\cos(n\theta)$ and $\sin(n\theta)$ (see Eq. 5.5). This leads to the mentioned cancellation of second-order (ray-)aberrations. From the perspective of wave-aberrations, we have to add simply the folding-induced aberrations in the optical wavefront. As the associated wave aberrations are third-order in the ray coordinates and as these coordinates oscillate periodically, the odd-order wave aberrations are just as often positive as negative and will cancel as well. This leads us to the surprising conclusion that also in the *xz*-principal plane we are left with the usual third-order (Seidel) aberrations. The magnitude of these terms is observed to be about a factor 10 larger than in the *y*-principal plane (*cf.* Fig. 5.7). This increased magnitude results from the lenses being tilted in the *xz*-principal plane and is apparently caused by the off-axis aberrations of the individual lenses in Fig. 5.8b.

The observed linear dependence of Gouy phase on mode number, in the form $\theta_m \simeq a +$
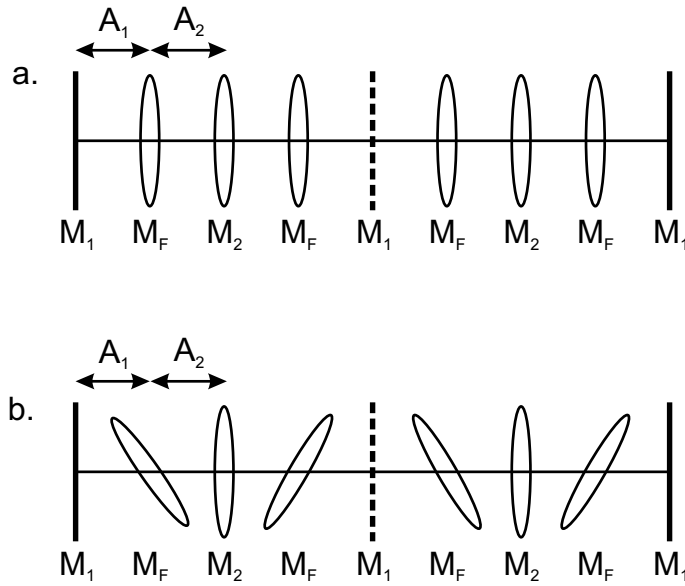
Figure 5.8: *The equivalent lens guide of a folded 3-mirror resonator in the xz-principal plane and the y-principal plane for two round-trips.*

bm, is consistent with this effectively third-order of the ray aberrations. To appreciate this statement, one should realize that the phase acquired by a transverse mode *m* (in comparison to mode $m = 0$) is $m\theta_m$, and that *m* depends quadratically on the off-axis distance Δr. This means that the nonparaxial term *bm* corresponds to a phase change that scales with the fourth power of Δr. Fourth-order changes in path length of the wave aberrations correspond to the Seidel aberrations.

The magnitude of the *individual* Seidel-aberrations of the lens guide in Fig. 5.8 can not be derived from our measurements or calculations. Only the *sum* of all Seidel coefficients is obtained, as they all exhibit the same scaling with ray coordinates after repetitive passage through the cavity. The magnitude of the unit of the aberrations is expressed as the phase shift divided by the off-axis distance of injection squared, being, *e.g.*, 2×10^{-5} rad/mm^2 for $N = 8$. We note that the observed increase in Gouy phase with the fourth-order off-axis distance is consistent with the sign and scaling found by Hercher [19].

5.7   Conclusions

We have demonstrated a very accurate method to measure the Gouy phase as a function of the mode number. For the folded three-mirror cavity, we found that the Gouy phase for the modes in the *xz*-principal plane changes is much stronger than its y-plane counterpart. A connection between the Gouy phase and aberration theory has been established. Effectively, the aberrations of a folded resonator behave as the Seidel aberrations, in spite of the lack of rotational symmetry. These results are supported by ray-tracing calculations; all calculations

are in very good agreement with the measurements.

5.8   Acknowledgement

CHAPTER 6

Connection between wave and ray approach of cavity aberrations

---

We connect the wave and ray description of spherical aberration in a cavity. The link we use is Fermat's principle in a frequency-degenerate cavity. In the ray picture, we consider periodically closed orbits beyond the paraxial limit and calculate the reduction in cavity length that is needed to compensate for the additional (nonparaxial) fourth-order terms. In the wave picture, we derive and discuss explicit expressions for the nonparaxial contribution to the Gouy phase. This Chapter combines and compares results from Chapter 4 and 5.

6.1 Introduction

The first analysis of frequency-degenerate Fabry-Perot cavity was based on a ray description. This analysis involved a calculation of the total path length $L_{\text{tot}}(\rho)$ of a closed orbit as a function of transverse amplitude ρ of the ray. Pioneering work was done by Hercher [19], Bradley and Mitchell [45], Arnaud [47], and Ramsay and Degnan [46]. We have generalized this analysis from the confocal resonator, $K/N = 1/2$, to an arbitrary K/N frequency-degeneracy, in Chapter 4.

Only recently, Visser *et al.* used a different approach based on wave optics. In their calculation, they benefited from the analogy between the paraxial wave-equation and the Schrödinger equation, using a quantum mechanical operator description for the evolution of the field profile [62]. Spherical aberration was included via a fourth-order term related to the mirror height profile. In this Chapter, we will extend this wave approach by including another term that was previously overlooked. In many cases this extra term, which is also fourth-order and related to the transverse momentum of the ray, dominates.

The challenge to connect the above ray and wave description has not yet been accomplished. We will do so in this Chapter. The key to success is the application of Fermat's principle in a frequency-degenerate cavity. For rays, this principle states that the realized closed orbit is the one that extremizes the total path length, making $dL_{\text{tot}}(\rho)/d\rho = 0$. To preserve the closed orbit beyond paraxiality, the cavity length should be reduced for increased transverse displacement. For waves, a similar requirement of "complete recovery after N round-trips" imposes frequency-degeneracy of the cavity eigenmodes. More precisely, it requires that the Gouy phase of the contributing modes differs by multiples of $2\pi/N$. We will derive an expression for the nonparaxial contribution to the Gouy phase and show that higher-order modes (again) require a reduction in cavity length to maintain the phase relation of the superposition after N round-trips. The comparison between the ray and wave result, finally provides for the necessary link between both pictures.

In Section 6.2, we review the ray description of Chapter 4 and use it in order to calculate the mentioned reduction in cavity length. In Section 6.3, we extend the standard wave description beyond the paraxial regime. We briefly review the wave description introduced in [62], and extend it by including the nonparaxial contribution of the transverse momentum of the ray. In Section 6.4, we compare the results from the ray and wave description by relating the transverse ray displacement to the mode number. We end with a concluding discussion in Section 6.5.

6.2 Ray description of spherical aberration

The general idea of this Section is as follows. We assume a closed orbit inside a symmetric two-mirror resonator with spherical aberration operated close to a $1/N$ frequency-degenerate cavity length. We stretch the closed orbit without changing the position of the hit points on the mirrors. Obviously, the angles of reflection on the mirror have to change to preserve the closed orbit. The only physical trajectories, where the angle of incidence on the mirrors equals the angle of reflection, are found by Fermat's principal.

First, we review the ray description of the total path length of a closed orbit as presented

in Chapter 4. The central concept in this ray description is the average path length of a closed orbit, where the nth hit point at one mirror is given by $x_n = \rho \sin(n\theta_0 + \phi_0)$ [49] with ρ the transverse amplitude, θ_0 the round-trip Gouy phase, and ϕ_0 an additional phase that determines the type of orbit (with extreme cases: the V-shaped and the bow-tie orbit). This total path length is (see Eq. 4.1 in Chapter 4)

$$\frac{1}{2N}L_{\text{tot}}(\rho) = L - B(L - L_{\text{res}})\frac{\rho^2}{R^2} - A\frac{\rho^4}{R^3} , \qquad (6.1)$$

where L is the on-axis cavity length and $L_{\text{res}} = R[1 - \cos(\theta_0/2)]$ is the paraxial resonance length (at $\rho \approx 0$) for exact $1/N$-degeneracy. For $(N \geq 3)$ the spherical aberration coefficient A and the detuning coefficient B are (see Eqs. 4.2 and 4.3 in Chapter 4)

$$A = \frac{1 + \cos(\theta_0/2)}{32\left[1 - \cos(\theta_0/2)\right]} = \frac{2R - L_{\text{res}}}{32L_{\text{res}}} \quad \text{and} \qquad (6.2)$$

$$B = \frac{1}{2}\left[\frac{1}{1 - \cos(\theta_0/2)}\right] = \frac{R}{2L_{\text{res}}} . \qquad (6.3)$$

Equation 6.1 describes the average length of a mathematically closed orbit, but this orbit does not necessarily fulfill the physical requirements of reflection angles. Special orbits are the ones that also fulfill the latter requirement, which is most compactly formulated via Fermat's principle $dL_{\text{tot}}(\rho)/d\rho = 0$. Taking the derivative of Eq. 6.1 and setting $dL_{\text{tot}}(\rho)/d\rho = 0$ we obtain

$$\Delta L \equiv L - L_{\text{res}} = -\frac{2A}{B}\frac{\rho^2}{R} = -\frac{z_0^2}{2RL}\frac{\rho^2}{R} , \qquad (6.4)$$

where $z_0 = \frac{1}{2}k_0 w_0^2 = k_0\gamma_0^2 = \frac{1}{2}\sqrt{2RL - L^2}$ is the Rayleigh-range, k_0 is the wavevector, and w_0 and γ_0 are two different measures for the fundamental beam waist. As both coefficients A and B in Eq. 6.4 are positive for stable resonators ($L < 2R$), off-axis (nonparaxial) rays require a cavity length reduction to satisfy Fermat's principle.

For completeness, we note that the above expressions for A and B do not hold for $N = 2$. For $N = 2$, the two extreme orbits, the V-shaped and a bow-tie orbit, have different coefficients A and B. This can easily be understood as the maximum transverse deviations x_n are ρ and $\rho/\sqrt{2}$ for the V-shaped ($\phi_0 = 0$) and the bow-tie ($\phi_0 = \theta_0/4$) orbit, respectively. Furthermore, the V-shaped orbit does not show spherical aberration, *i.e.*, $A = 0$, as the incident ray at the off-axis hit points is normal to the mirror surface. Hercher's result for the bow-tie orbit is

$$\frac{1}{2N}L_{\text{tot}}(x_n) = L - (L - L_{\text{res}})\frac{x_n^2}{R^2} - \frac{x_n^4}{4R^3} , \qquad (6.5)$$

where $x_n = \rho/\sqrt{2}$ is the maximum transverse deviation and ρ being the transverse amplitude.

For $N = 2$ there is also an exact solution of the form [63]

$$L_{\text{tot}}(\alpha) = 4R\left[2 - \frac{1}{\cos(\alpha/2)}\right] , \qquad (6.6)$$

where α is the angle of the diagonal ray in the bow-tie. The cavity length reduction, predicted by this exact solution is $\Delta L = -R\alpha^2/8$. As $\alpha \approx 2x_n/R$ in a confocal resonator, this result is consistent with the restriction $dL_{\text{tot}}(x_n)/dx_n = 0$, which yields $\Delta L = -x_n^2/(2R)$ when applied to Eq. 6.5.

6.3 Wave description of spherical aberration

The paraxial description of a symmetric two-mirror resonator of length L with mirror curvatures R (see Fig. 6.1) is centered around the concept of the round-trip Gouy phase

$$\theta_0(L) = 2\arccos(1 - L/R) . \tag{6.7}$$

Changes in the cavity length will modify this (paraxial) Gouy phase via the derivative

$$d\theta_0(L)/dL = \frac{2}{\sqrt{L(2R-L)}} = \frac{1}{z_0} . \tag{6.8}$$

In a 1D (planar) description of the cavity field, the phase delay of the m-th order Hermite-Gauss mode as compared to a plane wave is

$$\Psi_m = (m + \tfrac{1}{2})\theta_0 . \tag{6.9}$$
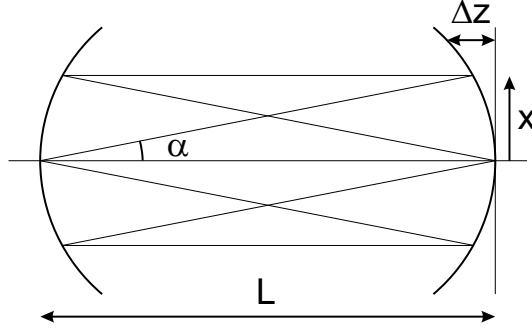
Figure 6.1: *Sketch of a symmetric two-mirror cavity of length L comprising two mirrors with radius of curvature R. The mirror curvature is characterized by the height profile Δz. The closed orbit is threefold frequency-degenerate (N = 3). The slope of the rays is characterized by the angle α.*

For larger beam displacements, *i.e.*, higher-order modes, an additional nonparaxial term contributes to the Gouy phase. Roughly speaking, the phase delay of m-th order Hermite-Gauss mode as compared to a plane wave can be separated in a linear and nonlinear contribution of the form (see Chapter 5)

$$\Psi_m \equiv \Psi_{\text{lin.}} + \Psi_{\text{nonlin.}} \approx am + bm^2 , \tag{6.10}$$

where $a = \theta_0(L)$ is the paraxial Gouy phase.

The nonparaxial term in Eq. 6.10 is a measure for the aberrations. It shows that a change in cavity length is needed to maintain frequency-degeneracy for higher-order modes also in the nonparaxial wave description. When the derivative $(\Psi_{m+1} - \Psi_{m-1})/2 = a + 2bm$ is fixed to a multiple of $2\pi/N$, degeneracy is fulfilled. The derivative $a + 2bm$ remains constant for

a higher-order mode m by lowering a (b is a higher-order correction). Using $a = \theta_0(L) = \theta_0(L_0) + [d\theta_0(L)/dL]\Delta L$, we thus obtain

$$\Delta L = \frac{-2bm}{d\theta_0(L)/dL} = -2bmz_0 \ . \tag{6.11}$$

We find again that the cavity length has to be reduced to maintain frequency-degeneracy within a set of higher-order modes. In the next Subsections, we will derive an explicit expression for $b > 0$ in terms of R and L, to further quantify this length reduction.

6.3.1 Effect of mirror shape (x^4-term)

Visser *et al.* [62] have given a wave description of two-mirror resonators, based on the mirror profile $\Delta z(x)$ shown in Fig. 6.1. Their description is essentially based on the expansion of the mirror profile $\Delta z(x)$ beyond the paraxial quadratic terms as

$$\Delta z = R - \sqrt{R^2 - x^2} \approx \frac{x^2}{2R} + \frac{x^4}{8R^3} \ , \tag{6.12}$$

where the fourth-order term acts as small perturbation. This term, describing the spherical aberration of the mirror, acts as the following perturbation on the potential in a Schrödinger-type equation

$$V_{\text{eff}}(x) = \frac{1}{16kR}(1 - g^2)\frac{x^4}{\gamma^4} \ , \tag{6.13}$$

where $g \equiv 1 - L/R$ (see Eq. (37) of Visser *et al.* [62]). For a fixed cavity length L, the perturbation slightly shifts the frequency of a mode with mode number m.

The (in-plane) 1D-version of Eq. (50) in Visser *et al.* [62] predicts a round-trip phase delay of

$$\Psi_m = \Psi_{\text{lin.}} + \Psi_{\text{nonlin.}} \approx 2\arccos\left(1 - \frac{L}{R}\right)(m + \tfrac{1}{2}) + \frac{L}{2kR(2R-L)}\left(\tfrac{3}{2}m^2 + \tfrac{3}{2}m + \tfrac{3}{4}\right) \ , \tag{6.14}$$

where the first terms combine Eqs. 6.7 and 6.9, and the second term quantifies the nonlinear contribution to the round-trip phase delay via

$$\Psi_{\text{nonlin.}} \approx b_x m^2 = \frac{3L}{4kR(2R-L)}m^2 \ , \tag{6.15}$$

assuming $m^2 \gg (m + \tfrac{1}{2})$. Note that we have included a subscript x to b_x to distinguish this mirror-based contribution from the momentum-based contribution b_p discussed in the next Subsection.

6.3.2 Effect of slope in rays (p^4-term)

The above description was based on a Taylor-expansion of the mirror height profile only. A more complete description is obtained if we also account for the higher-order terms in the Taylor-expansion of the transverse momentum

$$k_z = k_0\cos(\alpha) = \sqrt{k_0^2 - p^2} \approx k_0 - \left(\frac{p^2}{2k_0} + \frac{p^4}{8k_0^3}\right) , \tag{6.16}$$

where $p = k_0 \sin(\alpha)$ is the transverse momentum of the ray at angle α. The quadratic term in the expansion corresponds to the paraxial wavevector. The fourth-order term gives rise to an additional nonparaxial contribution. The perturbation on the potential associated with this contribution is [64]

$$W_{\text{eff}}(p) = \frac{1}{4kL} \frac{1-g}{1+g} \gamma^4 p^4 .$$ (6.17)

Straightforward calculus shows that the b_p coefficient derived for this momentum-based term is larger than the b_x coefficient derived above by a factor $2R/L$, making

$$b = b_x + b_p = \frac{3L}{4kR(2R-L)} \left(1 + \frac{2R}{L} \right) .$$ (6.18)

The existence of a p^4-term on top of a x^4-term is also touched upon in Section 8.5, where an analysis based on the effective index method gives exactly the same ratio $(2R/L)$ between these two terms. The importance of the fourth-order term in the Taylor-expansion of the momentum has been discussed in several other papers that go beyond the paraxial regime [65, 66].

6.4 Comparison of wave and ray description

In the two previous Sections, we have used both the ray and wave description to calculate the reduction in cavity length that is needed to retain frequency-degeneracy beyond the paraxial regime, *i.e.*, for large transverse amplitudes ρ, *c.q.*, modes with large mode number m. In the ray description, we obtained Eq. 6.4, which reads

$$\Delta L = -\frac{2A}{B} \frac{\rho^2}{R} = -\frac{z_0^2}{2RL} \frac{\rho^2}{R} .$$ (6.19)

In the wave description, we obtained Eq. 6.11, which reads

$$\Delta L = -2bmz_0 = \frac{-3L(2R+L)}{8kRz_0} m .$$ (6.20)

In order to compare these calculated length reductions ΔL, we need to relate the squared displacement amplitude ρ^2 to the mode number m. This relation is $\rho^2 = 2m\gamma^2$ [12], where the waist at the mirror is $\gamma^2 = \gamma_0^2[1 + (z/z_0)^2] = \gamma_0^2[LR/(2z_0^2)]$. Substitution of this relation in Eq. 6.19 yields

$$\Delta L = -\frac{z_0^2}{2RL} \frac{\rho^2}{R} = -\frac{z_0}{2kR} m .$$ (6.21)

A quantitative comparison of Eqs. 6.20 and 6.21 shows that the required length reductions are different for the ray and wave description. For a general cavity length

$$\frac{\Delta L_{\text{ray}}}{\Delta L_{\text{wave}}} = \frac{2R-L}{3(2R+L)} .$$ (6.22)

Only in the short cavity limit $L \ll R$, Eq. 6.20 becomes comparable to Eq. 6.21. In this limit, the ray result Eq. 6.20 yields

$$\Delta L = \frac{-3z_0}{2kR} m \; . \tag{6.23}$$

In the short cavity limit, the ray and wave description of spherical aberration are thus identical except for a prefactor.

6.5 Concluding discussion

To shed light on the difference between the ray and the wave descriptions of cavity aberrations, we have tried to determine their validity experimentally. Unfortunately, this attempt failed for two reasons. First of all, the relation between the measured phase delay θ_m and mode number m was not strictly linear, as was predicted by theory and demonstrated experimentally for a folded three-mirror resonator (see Ch. 5). Secondly, and more important, the relation depended strongly on the alignment of the cavity and the injection of the beam. Apparently, the mirror surface is nonspherical and contributes additional aberrations on top of the ones calculated in this Chapter.

In conclusion, we have presented an extension of the wave description of spherical aberration, introducing a term that was previously overlooked. Furthermore, we have tried to reconcile results from the ray model presented in Chapter 4 and wave models presented in Chapter 5 and ref. [62]. We could link both models using the cavity length reduction needed to preserve frequency-degeneracy beyond paraxiality. This attempt was successful only in the short cavity limit. This somewhat surprising result is not yet fully understood.

CHAPTER 7

Characterization of diamond-machined mirrors

Diamond-machining is used to fabricate the composite substrates elaborated on in Chapter 8 and 9. This technique causes a different type of irregularities than traditional grinding and polishing does. In this Chapter, the influence of the irregularities on the resonator dynamics will be investigated for a two-mirror cavity, where either one or both mirrors have been made by dielectric multi-layer coating of a diamond-machining produced substrate. Besides the tools discussed earlier in this Thesis, we also introduce polarization measurements to characterize the scattering.

7.1 Introduction

Precision machining dates back to World War 2, but substrates more or less acceptable for optical applications appeared only in the early 1970s [67]. State-of-the-art diamond-turned optics have a $\lambda/20$ peak-to-valley surface figure error and $0.2 - 0.4$ nm surface roughness [68]. Diamond-machining can be used to manufacture aspherical optics and offers the possibility to produce bifocal substrates, *i.e.*, substrates with a convex inner and a concave outer part, as used in Chapter 8 and 9. The convex inner part will also be denoted as "dimple". The surface of diamond-machined substrates shows periodic (circular) grooves due to the periodic movement of the diamond-chisel during machining. In this Chapter, we will investigate the effect of these grooves on the resonator dynamics of two conventional resonators, *i.e.*, without a dimple. The concave mirrors in the half-symmetric (flat/concave) and symmetric resonator (concave/concave) are, however, produced by diamond-machining, whereas the flat substrate is traditionally polished. The configurations in Chapter 8 and 9, comprising a bifocal mirror, are identical to the configurations investigated in this Chapter except for the central dimple inside the concave section.

This Chapter is organized as follows. The mirrors and setup are introduced in Section 7.2 and the mirror surface is interferometrically studied in Section 7.3. The cavity finesse and the losses deduced from the spectrum are discussed in Section 7.4. In Section 7.5, the influence of scattering on the polarization of the transmitted light will be demonstrated. We will end this Chapter with a conclusion.

7.2 Production of the mirrors

In an early stage of the project concerning the manufacturing of composite mirrors, we tried, in collaboration with Philips [69], to make the mirror substrates out of the polymers PMMA and Zeonex. The melting temperature, however, of both polymers is so low that the substrates deformed during the coating-procedure. Later, in collaboration with TNO [31], we moved to calcium fluoride (CaF_2) as the material out of which the substrates of our flat and concave mirrors have been made. Calcium fluoride is a crystal widely used for optical substrates, *e.g.*, in lithography systems, as it has a high transmission even at UV wavelengths as short as 175 nm [70]. The prime advantage of this material for our experiment is that it chips very fine during the diamond-machining procedure thus allowing for a low surface roughness. Furthermore, its melting temperature is very much higher than the temperature reached during the dielectric multi-layer coating process. This implies that the surface figure is maintained. Last but not least, CaF_2 is transparent at 800 nm. Drawbacks of CaF_2 are the low hardness and high coefficient of thermal expansion which make it less easy to work with than a standard substrate material as fused quarz.

The concave mirror is machined with a diamond chisel and has a radius of curvature $R = 14$ mm. The effective mirror diameter is $D = 2$ mm. For easy handling the substrates have a total diameter of 6 mm (see Fig. 7.1), of which the outer part is machined conically to prevent this part from scattering light back into the inner (concave) part via reflection by the other mirror of the cavity. For protection of the substrate, it is mounted in a metal ring. All substrates have been coated by LASEROPTIK [71] in the same coating run, with a stack of

24 layers of alternating Ta_2O_5 (refractive index 2.04) and SiO_2 (refractive index 1.46). The measured transmission of the coated flat substrate is $T = 8.3 \times 10^{-4}$ at 800 nm and assumed to be identical to the transmittance of other substrates coated in the same coating run. For accurate tuning of the cavity length, one mirror is placed on a translation stage (PI-M511). The resonator is scanned with a piezo (P-753.11C) to obtain a transmission spectrum. A lens ($f = 10$ cm) in front of the resonator mode-matches the input beam to the lowest-order mode of the cavity.
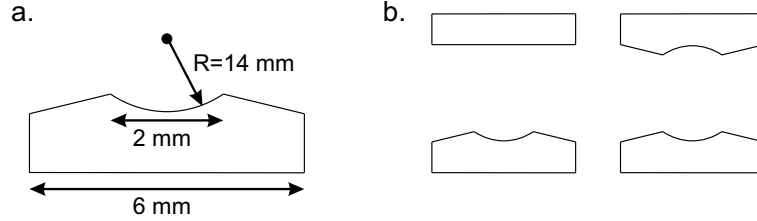

Figure 7.1: *(a) Sketch of the diamond-machined substrate, where the concave part is the actual mirror. The conical outer part prevents this part from reflecting light back into the inner part via reflection by the opposite mirror. (b) The half-symmetric and the symmetric cavity configuration.*

7.3   The mirror surface and scatter

The surface roughness of the bare substrate is measured with a WYKO interferometer at TNO [31] and found to be $\sigma \sim 2$ nm (RMS). We have to take into account that the roughness is measured over a limited area (100×100 μm^2), where the grooves are oriented predominantly in one direction. The total integrated scatter (TIS) and the surface roughness are related via TIS $= (4\pi\sigma/\lambda)^2$ [18]. Although this equation assumes randomly and not directionally distributed roughness, it gives a rough estimate of the TIS, being 1.0×10^{-3} in our case. Extra roughness introduced by the coating layers is neglected. From the measured transmittance and the calculated TIS we can calculate that the cavity finesse can be at most $F = \pi/(T + \text{TIS}) = 1500$.

The measurements with the WYKO interferometer do not only give us the surface roughness σ, but also the period of the grooves. The grooves formed by the diamond chisel resemble a somewhat irregular grating, having a period ranging from 10 to 25 μm. At a wavelength of 800 nm, such a period corresponds to scatter angles of $\alpha_s = 80 - 32$ mrad. Light scattered on the grooves will thus be displaced over $\Delta x = L\alpha_s = 0.4 - 0.16$ mm, per single-pass through a cavity length of $L = 5$ mm. Light scattered out of the lower-order modes can couple to higher-order modes with a 1D transverse mode number $m = (2\Delta x/w_0)^2 = 260 - 50$ [12], at a waist of $w_0 \sim 50$ μm. An alternative but equivalent calculation of the number of higher-order modes can be made in angular space. The beam angle of the fundamental mode in the far-field is $\alpha_0 = \lambda/(\pi w_0) = 5$ mrad [12]. Light scattered under an angle α_s can thus couple to modes with mode numbers $m = (\alpha_s/\alpha_0)^2 \approx 250 - 40$.

A first signature of scattering in our cavity is the appearance of Hercher fringes in the intensity profiles on the mirrors (Fig. 7.2a) close to frequency-degenerate points. Although
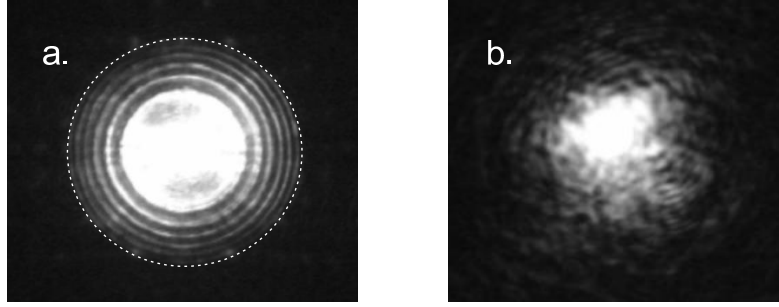
Figure 7.2: *(a) Image made with an imaging lens behind the cavity of Hercher fringes in the symmetric configuration close to a 4-fold frequency-degenerate cavity length ($\Delta L = 60\ \mu m$). The outer fringe (dashed circle) coincides with the radius (1 mm) of the mirror. (b) Intensity profile of a distorted TEM_{00} observed at a fixed cavity length close to 4-fold frequency-degenerate cavity length ($\Delta L = 100\ \mu m$).*

we inject only on-axis, fringes appear over the full mirror-aperture due to resonant trapping of scattered light (also see Chapter 4). A second signature of scattering is the mode coupling observed in the transmitted intensity profile of an injected TEM_{00}-mode as shown in Fig. 7.2b. The profile of the transmitted eigenmode is not a nice Gaussian TEM_{00}, but also shows the admixture of higher-order Gaussian modes (see Chapter 3). The cavity length is fixed to the resonance of the TEM_{00}-mode by manually tuning the piezo-voltage.

7.4 Spectra and imperfections

Typical transmission spectra of the symmetric and half-symmetric cavities are shown in Fig. 7.3, where the TEM_{00}-like mode is excited predominantly. Both spectra are stable over time and look similar to spectra from resonators using mirrors based upon traditionally polished substrates.

Figure 7.3: *Transmission spectra slightly away from $N = 4$ of (a) a half-symmetric ($L \approx 7.0$ mm) and (b) a symmetric resonator ($L \approx 4.1$ mm)*

We measured the finesse several times, after taking out one of the mirrors and realigning the cavity every attempt. The highest measured finesse is $F = 1280 \pm 50$. T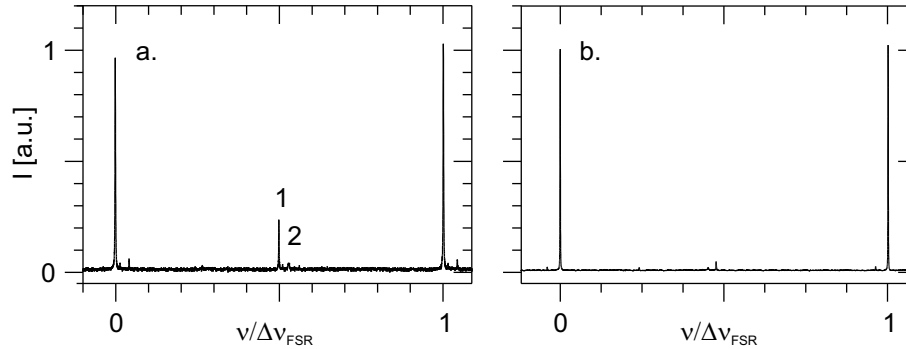his experimental finesse is in the order of the finesse estimated from the surface roughness. Using $F = \pi/(A + T)$ and $T = 8.4 \times 10^{-4}$ we calculate a loss $A = 1.6 \times 10^{-3}$, to be compared with the estimate of TIS$= 1.0 \times 10^{-3}$ as given above. This means that only $8.4 \times 10^{-4}/2.44 \times 10^{-3} \times 100\% \sim 34$ % of the light leaves the resonator via the mirrors, while the other 66 % is scattered away. From these numbers, we expect a peak transmission for the lowest order mode of $\eta^2 = [T/(A + T)]^2 = 12$ %, which agrees approximately with our experimental observation of $\eta^2 = 9$ %. This means that we are able to mode-match very well and inject most of the light into the TEM$_{00}$-mode.

An important experimental observation is that the resonance width and peak transmission depend strongly on both the alignment and the length detuning. Tilting the back-mirror over $\sim 0.1°$ can change the peak transmission by as much as a factor 10, and a length detuning of only $\Delta L \sim 0.6$ μm can already change the peak transmission η^2 by (relatively) 30 %. Although the loss increases in both cases, we are always able to predominantly excite the TEM$_{00}$-mode. The sensitivity to angular alignment can be easily understood as the waist of the fundamental mode on the mirror ($w_0 = 50$ μm for $L = 5$ mm) is just a few times bigger than the period of the grooves ($10 - 25$ μm) on the mirrors. The sensitivity to a length detuning over only $\Delta L \sim 0.6$ μm is very surprising, and not yet understood.

At degeneracy $N = 4$ and on-axis injection, the odd modes in the spectrum with ditto summed transverse mode numbers $m + n$ at $\nu/\Delta\nu_{\mathrm{FSR}} \sim 0.25$ and 0.75 are not excited due to proper (inversion-symmetric) alignment. Some even modes, other than the TEM$_{00}$ remain, however, *e.g.*, the two tiny modes (denoted 1 and 2) at $\nu/\Delta\nu_{\mathrm{FSR}} \sim 0.5$. From manual tuning of the piezo-amplifier we can identify these modes with a camera behind the resonator as the TEM$_{02}$ and TEM$_{20}$.

The lifted degeneracy of these modes allows us to quantify the astigmatism as one of the aberrations of the cavity. The measured spectral spacing $\Delta\nu/\Delta\nu_{\mathrm{FSR}} \sim 2\%$ can be converted into the deviation of the mirror radius ΔR compared to the average radius of curvature R. Substitution of 0.50 and 0.52 for $n + m = 2$ in $(\nu_{nm} - \nu_{00})/\Delta\nu_{\mathrm{FSR}} = (n + m)\theta_0/2\pi = (n + m)\arccos(\sqrt{1 - L/R})/\pi$ results in $\Delta R/R \sim 6$ %. This large value is likely to represent the relative difference in the "local curvature" on the probed mirror surface. A similar argument has been given to explain the observed astigmatism in "super-cavities" [56].

The mode coupling, mentioned earlier in relation to the mode profile, appears also in the spectra. Taking a closer look at the dominant resonances (not shown in detail here) we observe weakly excited higher-order modes that couple with the TEM$_{00}$-mode. Consequently, the lineshape of the resonances in the spectrum is not fully Lorentzian and the width and height vary close to frequency-degeneracy. As the lineshape of the resonances is distorted by mode coupling, it would have been better to determine the cavity finesse by a cavity ring-down experiment. This is, however, not a trivial experiment as the $1/e$-decay time is very short; we expect roughly $\tau = FL/(\pi c) \sim 0.1$ ns.

7.5 Polarization and scattering

In this last Section, we study the polarization of the light transmitted through a cavity, comprising again a flat and a concave mirror, but now with a polarizer behind the resonator. We inject vertically polarized light off-axis at an angle, as compared to the optical axis, in the 8-fold frequency-degenerate cavity ($L = 2$ mm). For a transmission axis of the polarizer parallel to the input polarization we clearly observe 8 hit points on the mirror as shown in Fig. 7.4a. When we rotate the polarizer over 90°, we still observe the hit points on the mirror as shown in Fig. 7.4b. This is surprising as intuitively one would expect that the polarization should be preserved inside the resonator, and the component perpendicular to the input polarization would be zero. In practice, the light behind the cavity contains, however, a surprisingly large component with a polarization perpendicular to the input polarization. More specifically, the intensity in the hit points is only $75\times$ weaker for polarization perpendicular to the input polarization than for the parallel component. This observation is not an artifact of our polarizer. Our Polarcor[TM] polarizer (Newport 05P109AR.16) is well-suited for this experiment: it has a specified acceptance angle as large as 15° (typical angles for our configuration are 2°) and the combination of the laser and the polarizer has a measured extinction ratio of 35000 : 1 for normal incidence.
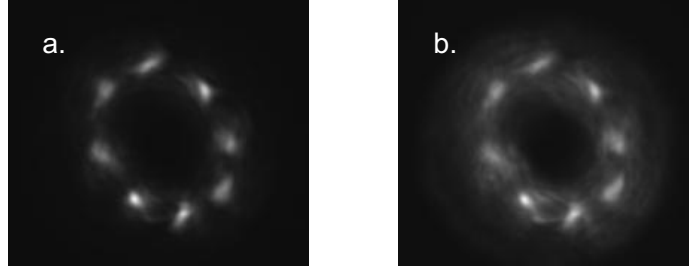
Figure 7.4: *Intensity profiles of a corkscrew-like ring mode on the mirror of a cavity comprising a flat and a concave mirror. The 8 hit points on the mirror show the 8-fold frequency-degeneracy of the resonator at a cavity length of $L = 2$ mm. The circle described by the hit points has a diameter of 0.46 mm. The transmission axis of the polarizer behind the cavity is (a) parallel and (b) perpendicular to the input polarization. The shutter time of the camera is much bigger than the scan duration through a free spectral range: $0.5\ s > 0.05\ s$.*

The observation discussed above might be related to other physics than scattering. The measured depolarization could result from a geometrical (or Berry) phase [72, 73], that quantifies the polarization rotation experienced by orbits that do not propagate in a single plane.

Taking a closer look at the intensity profiles, we observe furthermore that the intensity profile for perpendicular polarization has a relatively brighter "circular background". The origin of the light inbetween the hit points lies in the fact that light is scattered out of the hit points by surface roughness of the mirrors. This scattering-induced depolarization of the light has a different origin than the geometrical depolarization mentioned before and is reflected in the different ratios for the intensities in the hit points and the average throughput.

Cross-sections of the intensity profiles, show that the maximum intensity of the background normalized to the intensity in the hit points is 0.25 and 0.10 for perpendicular and parallel polarization, respectively. This means that for parallel polarization the light is more confined in the hit points, whereas for perpendicular polarization the light is spread more equally over the mirror.

7.6 Conclusion

We have demonstrated that a cavity comprising diamond-machined mirrors can achieve a finesse of $F = 1300$, comparable to the finesse ($F = 1 \times 10^3 - 1 \times 10^4$) achieved in standard Fabry-Perot resonators (dimensions ~ 1 cm and standard coating procedure). The alignment of a diamond-machined cavity is, however, more subtle due to the periodic grooves in the substrates made by the diamond chisel.

CHAPTER 8

Laguerre-Gaussian modes in a bifocal resonator

We investigate the eigenmodes of a cavity, composed of two mirrors, one of which is a bifocal mirror. As the bifocal mirror is rotationally symmetric, it favors a different mode family than traditional stable cavities based upon two monofocal mirrors. A numerical simulation based on an effective index is presented for a better understanding of the optical properties of this system.

8.1 Introduction

In ideal cavities with a rotationally-symmetric quadratic index (or gain) profile, there is considerable degeneracy and the eigenmodes combine to frequency-degenerate classes. Within each of these classes one is free to choose as basis either all Hermite-Gaussian (HG$_{mn}$) modes with fixed $n+m$ or all Laguerre-Gaussian (LG$_{lp}$) modes with fixed $2p+|l|$ [12, 74]. Here, m and n indicate the two transverse mode numbers, whereas l and p are the azimuthal and radial mode numbers, respectively. In practical resonators, any small deviation will lead to a preference of one basis over the other. The HG-modes are preferred if the rotational symmetry is broken, and x- and y-axes can be distinguished [12]. The LG-modes are preferred if the rotational symmetry is maintained, but the index profile is nonquadratic [75].

As an interesting example, a Vertical Cavity Surface Emitting Laser (VCSEL) [76,77] can show both cylindrical (LG) and rectangular (HG) modes in one system. The preferred mode-family is now determined by both the physical shape of the cavity and the gain profile in the amplifying medium. The tuning parameter to alter this profile is the injection current; the mode profiles are generally rectangular for low injection currents, but become cylindrical for high injection currents, where thermal lensing and carrier distribution play a more prominent role.

However, in almost any passive resonator the observable eigenmodes are the HG rather than the LG-modes as the rotational symmetry is apparently broken more strongly, by, *e.g.*, astigmatism, than the effective quadratic guiding corresponding to the focussing action of the mirrors [78]. In this Chapter, we will report on a stable cavity in which LG-modes are preferred. Our system is a composite cavity comprising mirrors that are rotationally symmetric, but the height profile consists of two piecewise quadratic parts and is thus nonquadratic as a whole. The system, described in this Chapter, is a first trial in a series of experiments to demonstrate chaos in a open optical resonator; it is equivalent to the geometry discussed by Aiello *et al.* [79] and in Chapter 9 of this thesis.

This Chapter is organized as follows: After introducing the setup, we will report and discuss the measured mode profiles. These profiles will be compared with standard (analytic) LG-modes that exist in paraxial resonators based upon mirrors with a single radius of curvature. A model, based on the concept of an effective index, will be introduced to investigate numerically the effect of the composite height profile. We will finish this Chapter with a concluding discussion.

8.2 Setup

The resonator contains a flat and a composite mirror, as shown in Fig. 8.1. Both substrates have been made out of calcium fluoride (CaF$_2$) and have been coated in the same run. The measured transmission of the mirrors used in this experiment is $T = 5 \times 10^{-5}$ at a wavelength of $\lambda = 800$ nm. The composite substrate has been diamond-machined. As the composite mirror comprises a convex center (also denoted as "dimple") and a concave annulus, it creates two resonators: a (radially) outer part, which is stable for cavity lengths $L < R = 14$ mm, and a (radially) inner part, which is always unstable. The dimple, in combination with the flat mirror, forms an unstable resonator and acts, in analogy with quantum mechanics, as a rota-

tionally symmetric potential barrier, surrounded by a ditto potential well. This rotational symmetry combined with the nonquadratic (composite) mirror profile imposes LG-eigenmodes.
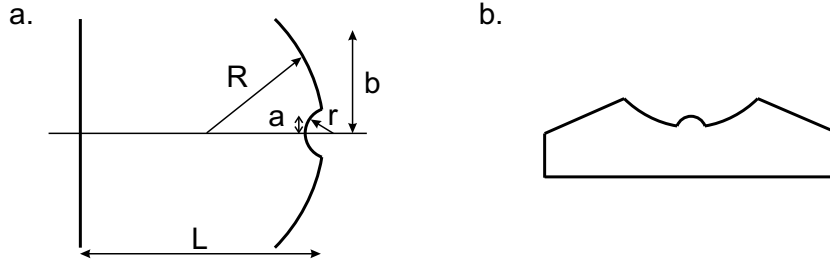

Figure 8.1: *(a) Our cavity configuration, operated at $L = 13.88$ mm, comprises a flat mirror and a bifocal mirror. The dimensions of the bifocal mirror are $R = 14$ mm, $r = -3$ mm, $a = 100$ μm, and $b = 1$ mm. (b) Sketch of the bifocal mirror, where the concave and convex inner part form the mirror. The conical outer part makes the handling of the mirror easier and prevents light to be scattered back into the cavity.*

In order to measure the profiles of the cavity eigenmodes, we use a $f = 10$ cm lens to inject a beam with a waist that is similar to the lowest-order mode of the outer cavity, off-axis under an angle with respect to the optical axis. This is to excite efficiently modes in the stable outer cavity. In order to measure the mode profiles on the bifocal mirror, a lens images the intensity profiles on a CCD-camera with linear intensity response (Apogee Alta U1) behind the cavity. The sub-wavelength control of the cavity length, which is needed to observe individual mode profiles, is obtained with a piezo-element. The cavity is typically operated at cavity lengths $L = 13.5 - 13.9$ mm, close to the instability point $L = R = 14$ mm. The absolute cavity length is calibrated with respect to the 3-fold frequency-degeneracy point ($L = 10.50$ mm). Such a frequency-degenerate point is easy to recognize spectrally and helps to pinpoint the cavity length accurately (few μm).

8.3 Experimental results

As discussed above, in ordinary resonators HG-modes are observed due to the almost unavoidable breaking of the rotational symmetry. We have checked this with a cavity identical to that described above, but without the central convex part. For operation under identical conditions this cavity favors indeed HG-modes. In contrast, the resonator of Fig. 8.1 shows a strong preference for the bifocal-mirror LG-modes. The preference for this mode-family originates apparently from the presence of the rotationally symmetric dimple on the composite mirror.

If we tune the cavity length to $L = 13.88$ mm, *i.e.*, close to instability of the outer cavity, we observe individual modes on the bifocal mirror with a clear rotational symmetry (see Fig. 8.2). The angle and position of injection in this experiment are fixed, and the cavity length is only changed within a free spectral range using the piezo-element. For each radial mode number p, ranging from 1 to 7, we observe LG-modes with various l-numbers. Note the intriguing smaller copies of the outer patterns, which will be discussed below.

75

The mode profiles, as shown in Fig. 8.2, can be resolved individually and are dominantly observed in a whole range of cavity lengths $L = 13.5 - 13.9$ mm close to the instability of the outer cavity. For shorter cavity lengths, *e.g.*, $L = 7.5$ mm, the rotational symmetry is still present in the intensity profiles; at this length, we do, however, no longer observe individual modes, as many modes are excited at the same time. The reason seems to be that for shorter cavity lengths, the number of available modes is much higher than for larger cavity lengths close to instability. This is related to the size of the waist of the fundamental mode on the outer part of the bifocal mirror, which is $w_0 = 177$ µm for $L = 13.8$ mm, but only $w_0 = 62$ µm for $L = 7.5$ mm. This means that the number of modes that fits inside the aperture of the mirror ($2b = 2$ mm in Fig. 8.1) is $(177/62)^2 = 8$ times lower close to instability than for the shorter cavity length.
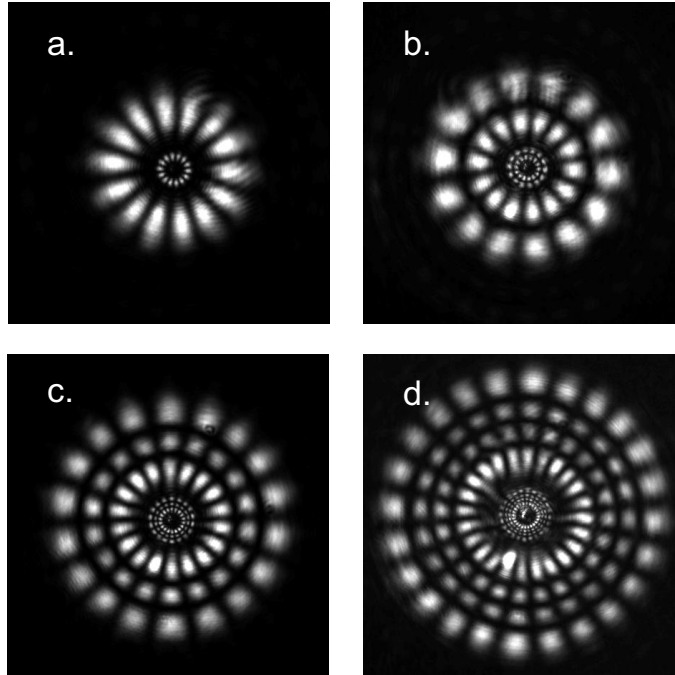
Figure 8.2: *Measured intensity profiles of modes on the bifocal mirror for "fixed cavity length" within a free spectral range. The half-symmetric resonator ($R = 14$ mm) is operated close to instability at a cavity length of $L = 13.88$ mm. The modes shown are (a) $LG_{7,0}$, (b) $LG_{7,1}$, (c) $LG_{9,2}$, and (d) $LG_{12,3}$. The area shown is 1.7×1.7 mm^2 on the bifocal mirror. Note the smaller copy of the intensity profile inside.*

An interesting feature of all experimental mode patterns is that inside the outer mode profile an identical but smaller copy of itself is observed. This inner pattern turns out to be a ghost-image. It results from a combined reflection on the concave side of the imaging lens behind the cavity (typical reflection $R = 1 - 4$ %) and the flat back-mirror of the cavity ($R \approx 100$ %). Imaging with a CCD directly behind the back-mirror of the cavity, *i.e.*, without imaging lens, did not show this copy. The rotationally-averaged intensity profiles shown in

Fig. 8.3 confirm this explanation. At first sight, it might seem strange that the inner image is roughly as intense ($50 - 100$ %) as the main image, whereas the expected power reflection is only $1 - 4$ %. The radius of the inner patterns is, however, about five times smaller than the original patterns, which means that the reflected power is concentrated in a 25 times smaller area. Combined with the intensity as compared to the main image, this corresponds to a power reflection of $2 - 4$ %, as expected.

8.4 Analytic LG-modes and comparison with experiment

For comparison of the experimental mode profiles with theory, we will now formally introduce the LG-modes [74]. These are solutions of the paraxial wave equation for a stable resonator comprising mirrors with a single radius of curvature (the central dimple will be taken into account in the next Section). The LG-mode profiles in radial coordinates are

$$E_{lp}(r,\phi) = E_0 \rho^l L_{lp}(\rho^2) e^{-\rho^2/2} e^{il\phi} \, , \tag{8.1}$$

where l and p are the azimuthal and radial mode numbers, and $\rho \equiv \sqrt{2}r/w_0$ is the dimensionless transverse position. For the fundamental mode we have $E_{00}(\rho) = E_0 \exp(-\rho^2/2) = E_0 \exp(-r^2/w_0^2)$, where w_0 is the waist of the fundamental mode. The Laguerre polynomials L_{lp} are simple expressions, for $p = 0$ to 2 they yield

$$L_{l0}(\rho^2) \quad = \quad 1 \, , \tag{8.2}$$
$$L_{l1}(\rho^2) \quad = \quad l+1-\rho^2 \, , \tag{8.3}$$
$$L_{l2}(\rho^2) \quad = \quad \tfrac{1}{2}(l+1)(l+2) - (l+2)\rho^2 + \tfrac{1}{2}\rho^4 \, . \tag{8.4}$$

Higher-order Laguerre polynomials can be found in mathematical handbooks [80].

The LG$_{7,1}$ and LG$_{12,3}$ modes derived from Eq. 8.1 are shown in Fig. 8.3a and c. The images of the calculated modes agree nicely with the measured intensity profiles shown in Fig. 8.2b and d. A more quantitative description and comparison can be made using a rotationally averaged intensity distribution, which is shown in Fig. 8.3b and d for both measured and calculated intensity profiles.

The measured intensity profiles are scaled such that the position of the minimum after the first lobe coincides with the corresponding zero in the calculated intensity profile. This scaling can also be used to pinpoint the waist of the fundamental mode and the exact cavity length. More specifically, the point $\rho = 1$ in the calculated profile corresponds to a radial distance $r = 125$ μm in the measured intensity profile, which results in the waist of the fundamental mode $w_0 = \sqrt{2}r/\rho = 177$ μm. This waist corresponds to a cavity length of $L = 13.8$ mm [12], which is in nice agreement with the cavity length determined previously.

8.5 Numerical calculation of modes in a bifocal resonator

Although the description of the standard LG-modes seems to be sufficient to qualitatively describe the experimental mode profiles, we still want to introduce here a model that can also take into account the presence of the dimple. This allows us to describe the influence of the
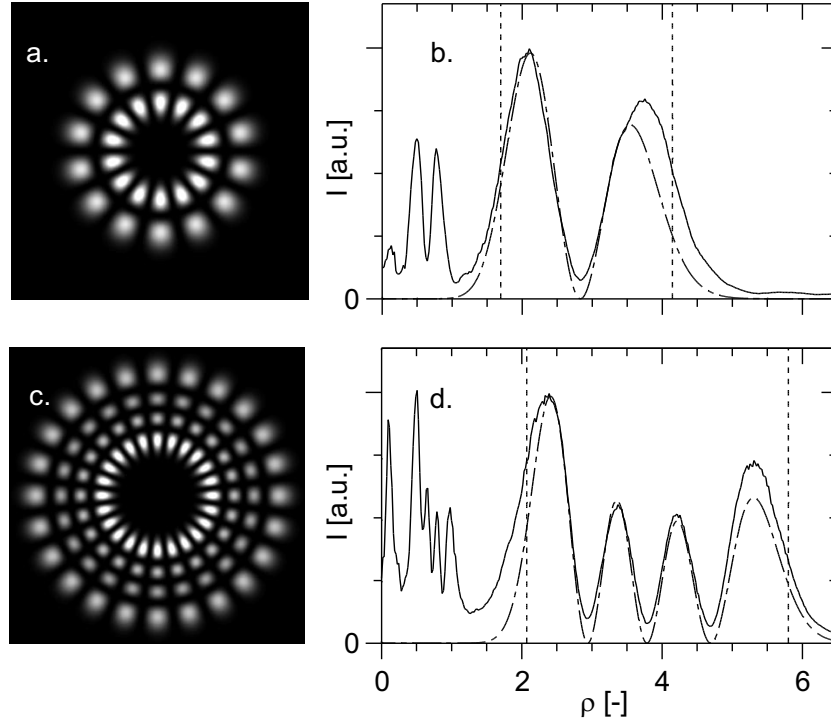
Figure 8.3: *Calculated intensity profiles of the (a) $LG_{7,1}$ and (c) $LG_{12,3}$ modes. The accompanying calculated (dot-dashed lines) and measured (solid lines) rotationally-averaged intensity profiles are shown in (b) and (d). Note the inner copy of the measured intensity profiles. The vertical dotted lines indicate the classical turning points of the modal ray. ρ is the dimensionless transverse position.*

dimple more quantitatively and offers more insight. Additionally, this model allows us to investigate the influence of spherical aberration on the mode profiles; by spherical aberration we mean the deviation of the actual wavefront from a spherical reference wavefront that solely depends on the position of a hit point on the mirror [14].

The transverse modes of the field in the resonator are dictated by the rotational symmetry of the cavity. This restricts the forward propagating electric field to cylindrical coordinates

$$E_{lp}(\rho, \phi, z, t) = \psi_{lp}(\rho, z) e^{i(k_z z - \omega t)} e^{il\phi} , \qquad (8.5)$$

where $\psi(\rho, z)$ is the slowly varying amplitude of the electric field, k_z the component of the wave vector in the propagation direction, ω the optical frequency, l the angular mode number, and $\rho = \sqrt{2}r/w_0$ is again the dimensionless transverse position.

The so-called effective-index model [81–83] assumes that the (transverse) waveguiding, by either a transverse variation of the electric permittivity ε or, effectively, by a mirror curvature, can be distributed over the length of the cavity and averaged over the axial coordinate. Although this model is strictly valid only if the transverse profile of the field does not change significantly during a full round-trip, we are confident that it will retain its essential features

also beyond this limitation by a simple rescaling in terms of an effective cavity length and an average field.

In the most simple version of the effective index model, the electric permittivity ε is assumed to have the form $\varepsilon = \varepsilon(\rho) = n(\rho)^2$ and consequently the amplitude of the field becomes independent of z and yields $\psi_{lp}(\rho, z) \sim h_{lp}(\rho)$. Application of the effective-index model to a plano-concave resonator means (in more physical terms) that the resonator is reduced to a planar cavity with a built-in radially varying effective index of the form

$$n(\rho) = n_0 \left(1 - \frac{\rho^2 w_0^2}{4RL} \right) , \tag{8.6}$$

with R the radius of curvature of the mirror. As stated by Hadley [82]; "the effective-index profile is determined by local changes in the Fabry-Perot resonance frequency (for rays that simply travel parallel to, but displaced from, the (z-)symmetry axis)".

Based on Eqs. 8.5 and 8.6, we can rewrite the scalar wave equation for a (slowly varying) amplitude of the field into a Schrödinger-type equation

$$(\nabla_\rho^2 - \rho^2) h_{lp}(\rho) = -2\tilde{\omega} h_{lp}(\rho) , \tag{8.7}$$

where

$$\nabla_\rho^2 = \frac{\partial^2}{\partial \rho^2} + \frac{1}{\rho} \frac{\partial}{\partial \rho} + \frac{1}{\rho^2} \frac{\partial^2}{\partial \phi^2} , \tag{8.8}$$

is the rescaled transverse Laplacian, $\tilde{\omega} = \Delta\omega/\omega_G = l + 2p + 1$ a dimensionless eigenfrequency, $\Delta\omega$ is the detuning as compared to an on-axis plane wave and $\omega_G = (c/2L)\theta_0$ is the natural frequency spacing, where θ_0 is the Gouy phase. The term $\frac{1}{\rho^2} \frac{\partial^2}{\partial \phi^2} = -l^2/\rho^2$ in Eq. 8.8 acts as a centrifugal potential, which forces the radial profile $h_{lp}(\rho)$ outwards for higher l.

We solve Eq. 8.7 with the so-called shooting method [84], where the integration proceeds from $\rho = \rho_1 = 0.8$, being the transition from the convex to the concave part of our bifocal mirror, to $\rho = \rho_2$, a position beyond the spatial extent of the mode. We start from $h = 0$ and $\partial h(\rho)/\partial\rho = 1$ and proceed stepwise to the edge using $\partial^2 h(\rho)/\partial\rho^2$ from Eq. 8.7. This iterative process is performed for 2000 consecutive transverse positions ρ. Doing so for various values of $\tilde{\omega}$ for a given l, we find $\tilde{\omega}$ that minimizes the field h at ρ_2 best.

For a more quantitative study of the influence of the dimple on the modes, we have included the dimple (radius $\rho = 0.8$) in our model, replacing ρ^2 in Eq. 8.7 by $R/r\rho^2 = -4\rho^2$, for $\rho < 0.8$. After including the dimple in our model, we can start the integration closer to the center *on* the dimple. We did so for modes with small l-values, like $l = 2$, as these relatively compact modes have the larger spatial extent that overlaps with the dimple and will be affected most. The effect of the dimple is, however, small; the eigenvalue $\tilde{\omega}$ and the position of the maximum change roughly 1 %, and the rising flank of the lobe in the intensity profile shows only a tiny bending point (not shown). The standard analytic LG-modes are thus sufficient to describe our measurements, as the centrifugal term (Eq. 8.8) in Eq. 8.7 still dominates over the potential arising from the dimple structure.

A first remark we want to make is the textbook [85] result that the classical turning points of the mode profiles can be found from Eq. 8.7 by solving $\rho^2 + l^2/\rho^2 - 2\tilde{\omega} = 0$, which results in $\rho^2 = \tilde{\omega} \pm \sqrt{\tilde{\omega}^2 - l^2}$. These points are indicated in Fig. 8.3 for both LG$_{7,1}$ and LG$_{12,3}$, and

coincide with the bending points on the flanks of the first and the last lobes in the intensity profiles.

The second remark is that the model offers the possibility to investigate the effect of aberrations on the mode profiles. As an example, we study spherical aberration, expanding the mirror height profile Δz beyond the quadratic term. Consequently, a fourth order term $-\alpha\rho^4$ has to be added to Eq. 8.7, where α indicates the strength of the aberration and equals $\alpha = 1/(8kR)\sqrt{L/R}$ (see Chapter 4). On second thought, not only the mirror height profile Δz, but also the intra cavity angles, *i.e.*, the transverse momentum of the ray k_z, should be expanded (see Chapter 6). The extra term in Eq. 8.7 is $-\beta\nabla_\rho^4$. The operator formalism of Visser *et al.* [62], discussed in Chapter 6, shows that $\beta = (2R/L)\alpha$ and $\langle\nabla_\rho^4\rangle = \langle\rho^4\rangle$. As a consequence, the second (momentum related) contribution to the spherical aberration is $2R/L$ larger than the one originating from the mirror height profile. The importance of the fourth-order term in the Taylor expansion has been discussed in several other papers that go beyond the paraxial regime [65, 66].

As a quantitative example, we study the strength of spherical aberration for our configuration, *i.e.*, $\alpha = 1.1 \times 10^{-6}$. Taking into account the momentum related contribution, the strength of the spherical aberration becomes $\alpha + \beta = \alpha(1+2R/L) \approx 3\alpha = 3.3 \times 10^{-6}$. This number is so small that even far off-axis, close to the edge of the mirror ($\rho = 8$), Eq. 8.7 is still dominated by the quadratic term ρ^2. The influence of spherical aberration on the mode profiles can thus be neglected.

8.6 Concluding discussion

In our system, the profile of the mirror is nonquadratic due to the presence of the central dimple. The dimple is needed to break the quadratic profile of the mirror, but is hardly visible in the mode profile. If we would have destroyed the quadratic profile in any other way, *e.g.*, by drilling a hole in the mirror, we probably would have observed almost identical LG-modes. The latter situation is roughly similar to a potential barrier of infinite height. The approximate mode profiles can be found from the effective-index model starting the integration just outside the dimple.

The discussed preference for a rectangular or cylindrical mode family is not limited to cavities but holds for waveguides [86] as well. To motivate this statement we mention that fibers with an elliptical core prefer a mode family similar to the Hermite-Gaussian (HG) modes in optical resonators [87], whereas fibers with a circular core favor a rotationally symmetric mode family [88]. The stepped (refractive) index of a circular core breaks in fact the quadratic guiding profile so strongly that the mode-profiles are influenced correspondingly and are quite different from the LG-modes. These modes are called LP-modes [89, 90].

In conclusion, we have demonstrated a passive resonator in which LG-modes are preferred, due to the rotational symmetric and nonquadratic profile of the mirror. The intensity profiles on the mirror nicely agree with standard (analytic) LG-modes, showing that the dimple does not yet influence the mode profiles noticeably. This we have checked with an effective-index model, which is also used to demonstrate that the effect of spherical aberration on the mode profiles is still negligible under our operating conditions.

CHAPTER 9

Combining a stable and an unstable resonator

We investigate a two-mirror resonator comprising two multi-mode cavities that are intrinsically coupled. The key element of this system is a mirror with a combined convex inner part and a concave shell. Tuning of the cavity length allows us to study the coupling inside a stable-unstable cavity combination as well as inside a stable-stable combination. The former configuration is expected to show the onset of chaos.

9.1 Introduction

In this Chapter, we present a preliminary experimental investigation of a novel type of open optical resonator that may show chaos. Wave chaos has been demonstrated in the microwave regime in closed billiards in 1990 [91]. In the optical regime, wave chaos is very hard to obtain with closed resonators since omnidirectional perfectly reflective coatings (as metals are in the microwave domain) do not exist. Furthermore, such closed resonators would be hard to access and adjust. On the contrary, a standard *open* resonator consisting of two high-reflectivity laser mirrors does not suffer from these problems, but such a configuration does not normally lead to chaos.

Two requirements have to be fulfilled for chaotic behavior in a resonator, be it closed or open. First, optical paths in a resonator have to be exponentially sensitive to the initial conditions and, secondly, the light has to be confined inside the cavity for a sufficiently long time, to produce mixing. A two-mirror unstable resonator offers the exponential sensitivity, but the rays escape the cavity after only a few round-trips so that mixing does not occur. A two-mirror stable resonator can confine the light, but is an imaging systems that does not possess the exponential sensitivity. To combine the "best of both worlds", we have designed the composite mirror shown on the right-hand sides of the two cavities shown in Fig. 9.2, below. This special composite mirror has a convex center and a concave outer part; it will also be denoted as a "bifocal" mirror as it contains two radii of curvature and thus two foci. While the unstable inner cavity provides the exponential sensitivity, the outer cavity collects the light leaving the unstable cavity and injects it back into the inner cavity, thus fulfilling the mixing requirement.

Numerical simulations help us to determine the proper configuration which might show chaos. *Wave* chaos for our configuration can, however, not be shown numerically, as in practice the wave equation can only be solved for small systems with a typical dimension a and wavenumber k, where $ka < 150$ [92, 93]. The experimental cavity, presented in this Chapter, corresponds to $ka \sim 8000$. Although our experiment deals with waves, the demonstration of *ray* chaos is important as ray chaos is a requirement for wave chaos, *i.e.*, when a resonator does not exhibit *ray* chaos, *wave* chaos will not occur either [42]. The presence of *ray* chaos in an open optical 2D-resonator has been predicted by Aiello *et al.* [79] based on calculations of the Lyapunov exponent. The Lyapunov exponent [94] is a measure for the exponential sensitivity to the initial conditions; it characterizes the mean rate of exponential divergence between two nearby orbits. The strip-resonator proposed by Aiello *et al.*, shown in Fig. 9.1, is a stable symmetrical two-mirror cavity in which a third two-side convex mirror is placed in the middle. For practical reasons this configuration has been slightly modified; the convex part has been combined with the concave outer mirror.

The most promising configuration to observe chaos does not only show a high Lyapunov exponent, but also a sufficient confinement of the rays inside the resonator. To allow sufficient time for chaos to develop, the ray should stay inside the resonator longer than the time associated with the Lyapunov exponent; $\tau_{\text{Lyapunov}} < \tau_{\text{escape}}$. Numerical simulations of the 2D cavity have been performed [95] for various cavity lengths and radii of curvature of the bifocal mirror. The most promising configuration, which will be introduced in Section 9.2, shows that it takes on average 1.5 round-trips [95] to show exponential divergence. The time a ray stays inside the resonator τ_{escape} is determined by the transmission loss due to the finite
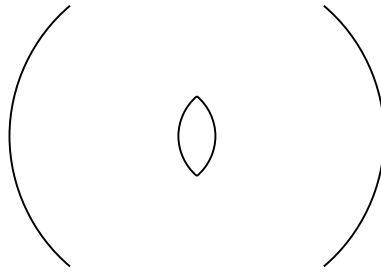
Figure 9.1: *Two-mirror cavity in which a third two-side convex mirror is placed in the middle. The inner mirror in combination with one of the outer mirrors forms an unstable resonator, whereas the combination of both outer mirrors forms a stable resonator.*

reflectivity of the mirrors and the escape or diffraction loss due to the finite transverse dimensions of the mirrors. The former is simply determined by the quality of the mirror coating, and will be discussed below. The latter is primarily determined by the aspect ratio of the resonator. Numerical simulations show that a square configuration ($L \sim 2b$) minimizes the escape of rays caused by the open nature of our cavity. Due to the ray character of the simulations only relative dimensions L/b are important. In contrast, when the wave character of light is taken into account, the absolute dimensions become important via the Fresnel number $b^2/\lambda L$, where b is the radius of the mirror, λ the wavelength, and L the cavity length.

The key characteristic of wave chaos is the repulsion between eigenfrequencies. To demonstrate this experimentally, it is necessary that resonances in the spectrum can be resolved, *i.e.*, the spectral width of a resonance should be small as compared to the average mode spacing, being the free spectral range divided by the number of modes. For confined modes, the spectral width is expressed by the cavity finesse $F = \pi/(1-R)$, which is fully determined by the reflectivity of the mirrors R. The number of "confined" modes in a stable resonator scales with the cavity dimensions and approximately equals the Fresnel number $N_F = b^2/\lambda L$. The eigenmodes can thus only be resolved when the Fresnel number is smaller than the finesse, which is realistically about 1000. This means that for a square cavity configuration and $\lambda = 800$ nm, the typical dimensions of the cavity should be in the order of $2b \approx L \approx 1$ mm.

The simulations provide only a simplified picture of reality. First of all, a realistic resonator is 3D and not 2D, as is assumed in the numerical simulations. In our experimental 3D-system, for instance, many (corkscrew-like) orbits exist that do not hit the dimple, *i.e.*, the convex central part of the bifocal mirror, at all. This means that in 3D the average number of round-trips needed to develop chaos will increase, as compared to the 2D-simulations. Furthermore, the experiment deals with waves, whereas interference effects are not taken into account in the numerical simulation. Therefore, although ray-simulations give us some insight, only an experiment can be conclusive on the existence of chaos.

To place our experiment in a broader historical perspective, we mention here some other experiments. One of the first experiments to describe the coupling of two resonators, is the coupling of two maritime clocks by Christian Huygens in 1662 [96]. He found that two nearby pendulum clocks swung with exactly the same frequency and 180 degrees out of phase. When he disturbed one pendulum the anti-phase state was restored within half an

hour. This simple experiment shows the essence of coupled systems. Examples are also found in the optical domain, *e.g.*, in ring-laser gyroscopes. In an ideal ring-laser, the two oppositely travelling waves are supposed to be uncoupled. Rotation of the resonator lets both waves experience a different path length and consequently different resonance frequency. This effect is known as the Sagnac-effect. If the intra-cavity light, however, experiences some backscattering (due to surface roughness and/or Fresnel reflection), coupling of the oppositely propagating waves is introduced [97] and the standing waves dominate at small rotation velocities. Also in optical systems with an active medium coupling can play a role. In dual VCSELs, two monolithic cavities are grown on top of each other and share a common mirror [98]. The degree of coupling is now determined by the quality of the transmission of the common mirror. Dual wavelength emission is generally observed.

In the system presented in this Chapter, both cavities are passive. Another difference as compared to other systems is the instability of the inner cavity. This accounts for the large coupling strength of both cavities. An uncoupled unstable resonator normally favors the lowest order modes, which is the least lossy, and operates (effectively) as a "single" mode-resonator. In our system the unstable resonator is, however, coupled to a stable resonator, which also supports the higher-order modes in the unstable cavity. Our system is thus a coupled multi-mode system, which makes it a very rich and intriguing system.

The general structure of this Chapter is as follows. In Section 9.2, the production method of the mirrors is discussed and both cavity configurations are introduced. A simple ray-tracing simulation of the cavity configurations, as presented in Section 9.3, pinpoints the most promising regimes. The experimental setup is discussed in Section 9.4. The rest of the Chapter is devoted to a study of the minimum requirements needed for chaos to be fulfilled. Questions that we will address experimentally are:

"Can we couple the inner and outer cavity?",

"How long does the light stay inside the cavity?",

"How often is the dimple hit?" and,

"Can the spectral resonances be resolved?".

These questions are answered on the basis of the two main methods at our disposal; spectral and spatial analysis. In Section 9.5, the experiments based on spectral information are introduced, while Section 9.6 presents and discusses the spatial intensity distributions on the mirror. All results are discussed in Section 9.7 and recommendations are made.

9.2 Substrates, mirrors and cavity configurations

The substrate for the composite mirror, with its concave outer part and convex inner part, can not be manufactured by traditional (polishing) methods. Diamond machining [67] does offer the possibility to produce such bifocal substrates, though. The substrates for the mirrors used in the experiment are made out of calcium fluoride (CaF_2). Calcium fluoride is a crystal widely used for optical substrates, *e.g.*, for lenses in lithography systems, as it has a high transmission at UV-wavelength, even below 175 nm [70]. The prime advantage of this material is that it chips very fine during the fabrication procedure so a low surface roughness ($\sigma_{RMS} \sim 2$ nm) can be achieved. Its melting temperature (1630 K) is much higher than the temperature reached during the high reflectivity coating process (~ 400 K); this implies that

the surface figure is maintained. Finally, it is transparent at 800 nm, which is the wavelength used in our experiment.

Two different pieces have been produced by TNO [31] according to our design; a concave and a bifocal one. The mirror substrates have been diamond machined with a chisel and the grooves on the substrate have a period ranging from $10 - 25$ μm. The concave mirror substrate has radii of curvature $R = 14$ mm and a nominal mirror radius $b = 1$ mm (see Fig. 9.2). The bifocal substrate has a radius of curvature $R = 14$ and $r = -3$ mm and a nominal mirror radius $b = 1$ mm and $a = 100$ μm, for the outer and inner part, respectively. Inspection of the composite mirror by an interferometer (WYKO-400) shows that the transition zone from the inner to the outer part is smaller than 15 μm and that the transition is smooth (step height$< \lambda /20$). We note that the inner and outer part of the composite mirror are automatically aligned and do not show tilt, as spheres always have a radius in common. For easy handling, the substrates have an outer radius of 3 mm, where the outer part with a radius r ranging from 1 to 3 mm, is machined conically to prevent this part from scattering light back into the resonator. Each diamond machined substrate, bifocal and simply concave, is mounted in a metal ring with an outer radius of 0.5 and 1 inch, respectively. We also possess a flat CaF_2-substrate with a diameter of 1 inch, which is not diamond machined but traditionally polished. All substrates are coated in the same coating run, with a stack of $12 \times 2 = 24$ layers of alternating Ta_2O_5 (refractive index 2.04) and SiO_2 (refractive index 1.46). The measured transmission of the mirrors after coating is 8×10^{-4}.
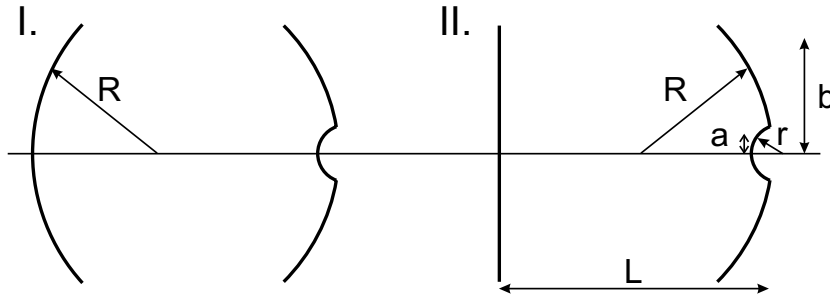

Figure 9.2: *Two cavity configurations, with an identical composite mirror on the right-hand side. The dimensions of the composite mirror are $R = 14$ mm, $r = -3$ mm, $a = 100$ μm, and b=1 mm. The left-hand mirror is either (I) concave with a radius of curvature $R = 14$ mm or (II) flat.*

Fig. 9.2 shows the two different cavity configurations that we have used; the dimple mirror in combination with the concave mirror (denoted in this Chapter as configuration I) and the dimple mirror in combination with the flat mirror (denoted as configuration II). The (radially) outer part of configuration I forms a resonator which is stable for all cavity lengths $L < 2R = 28$ mm. The stability of the inner cavity depends on the cavity length in a more complicated way and can be found from $0 \leq g_1 g_2 \leq 1$ [12], where $g_i = 1 - L/R_i$. Solving this equation for configuration I, where $R_1 = R = 14$ mm and $R_2 = r = -3$ mm, we find that the inner cavity is only stable for $11 < L < 14$ mm and thus unstable for $L < 11$ mm and $L > 14$ mm. This configuration has the advantage that we can explore the transition from a stable to an unstable inner resonator. Furthermore, we note that the magnification (equivalent

to the transverse mode stretching per round-trip) is limited to $M = 4.7$ for cavity lengths $L < 11$ mm (see Tab. 9.1).

When we replace the concave mirror by the flat one, we obtain configuration II which is equivalent to the geometry discussed by Aiello *et al.* [79]. It combines an outer part, which is stable for cavity lengths $L < R = 14$ mm, and an inner part, which is always unstable. Note that the magnification is already $M = 3$ for a cavity length of only $L = 1$ mm and increases with the cavity length, as shown in Tab. 9.2.

9.3 Ray-tracing the bifocal resonator

Extensive ray tracing simulations in ref. [95] have shown that ray-chaos is most likely found for $L \sim 2b$. In combination with the extra requirements for wave chaos, this condition becomes $L \sim 2b \lesssim 1$ mm [95]. In this Thesis a much simpler simulation is used to show how long the ray stays inside the resonator and how often the dimple is hit. The ray-tracing simulation, based on *ABCD*-matrix multiplication, calculates the path through the cavity for a given input position and injection angle on the bifocal mirror. A ray which hits the outer part of the mirror ($R = 14$ mm) experiences another *ABCD*-matrix than a ray that hits the inner part of the mirror ($r = -3$ mm).

To be able to perform some statistics, the path through the resonator is calculated for 51 input positions, equally spaced over the dimple (thus ranging from 0 to 100 μm), and 41 different angles (ranging from -0.01 to 0.01 rad) for every input position. These numbers are close to typical experimental values. The total number of injected rays is thus 2091. The number of round-trips is limited to 8000 (which would be equivalent to the unrealistically large cavity finesse $F = 2\pi \times 8000 \approx 50000$). From these data we calculate, for both configuration I and II, the probability distribution of the number of round-trips before escape from the resonator and of the number of dimple hits.

9.3.1 Configuration I

An overview of the simulations performed on a cavity I-configuration is shown in Tab. 9.1. It shows that outside the stable regime of the inner cavity, we hardly find stable orbits, except for the shorter cavity lengths. Only for very short cavity lengths, *e.g.*, $L = 1$ mm, most orbits stay inside the resonator for the maximized number of 8000 round-trips. This is also shown in more detail in Fig. 9.3a, where a probability distribution shows the number of rays vs. the number of round-trips before escape. The rays escaping earlier (less than 8000 round-trips) produce a (roughly) flat probability distribution. For the same cavity length, the average number of dimple hits is also substantial, 1548 out of 6694. The broad probability distribution shown in Fig. 9.3b indicates a variety of different orbits.

For $L = 12$ mm, the inner cavity of configuration I is stable and a ray remains on average inside the resonator for 4903 round-trips. We have to be careful with this number as rays can remain in the stable inner cavity without coupling to the outer cavity. Taking a closer look at the distribution of the number of round-trips a ray remains inside the cavity, we find that 60 % of the rays stay inside the resonator for all 8000 round-trips and that the other 40 % leave the cavity only after a few hits. The same division holds for the average number of dimple hits;

L [mm]	average # of round-trips	average # of dimple hits	N	M
1	6694	1548	8.3	2.6
2	1571	241	5.8	3.4
6	390	81	3.3	4.6
10	112	30	2.5	2.6
12	4903	4898	2.2	stable
15	80	12	1.9	-3.4

Table 9.1: *For six different lengths of a configuration I cavity, we have calculated both the average number of round-trips per ray before escape and the average number of dimple hits per ray. A total of $41 \times 51 = 2091$ different rays are traced through a configuration I-resonator, each over 8000 round-trips or less if the ray escapes at earlier time. The inner cavity is stable for $11 < L < 14$ mm. The numbers N and M are the degeneracy ($= 2\pi/Gouy$ phase) and the magnification of the inner cavity, respectively.*

60 % of the rays hit the dimple every round-trip, whereas 40 % hit the dimple only a few times. This confirms our statement that most rays stay inside the stable inner cavity and that most other rays are lost. The stable inner cavity will not show chaos as a stable resonator is not exponentially sensitive to the initial conditions.
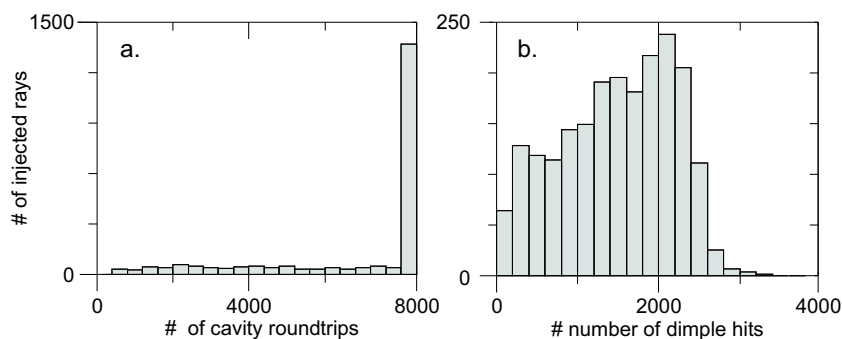

Figure 9.3: *Ray-tracing statistics for a configuration I resonator at a length of $L = 1$ mm with two concave mirrors ($R = 14$ mm), of which one has a central dimple ($r = -3$ mm). The two probability distributions show the number of rays (out of 2091) vs. (a) the number of round-trips before escaping and (b) the number of dimple hits.*

9.3.2 Configuration II

The statistics performed on configuration II is shown in Tab. 9.2. We again find that only for a very short cavity length a typical ray remains inside the cavity for a long time as well as a substantial number of dimple hits. Fig. 9.4 shows that for $L = 1$ mm only a fraction of the injected rays remain in the cavity for the full 8000 round-trips. Only for shorter cavity lengths, *e.g.*, $L = 0.5$ mm, almost all rays remain inside the cavity.

L [mm]	average # of round-trips	average # of dimple hits	N	M
0.5	7163	1477	16.5	2.2
1	2946	625	11.6	3.0
2	152	47	8.1	4.4
6	31	13	4.4	9.9

Table 9.2: *For four different cavity lengths of configuration II, we calculated both the average number of round-trips per ray before escape and the number of dimple hits per ray. A total of $41 \times 51 = 2091$ rays are traced through a configuration II-resonator, each over 8000 round-trips or less if the ray escapes at earlier time. The numbers N and M are the degeneracy ($=2\pi/Gouy$ phase) and the magnifications of the inner cavity, respectively.*
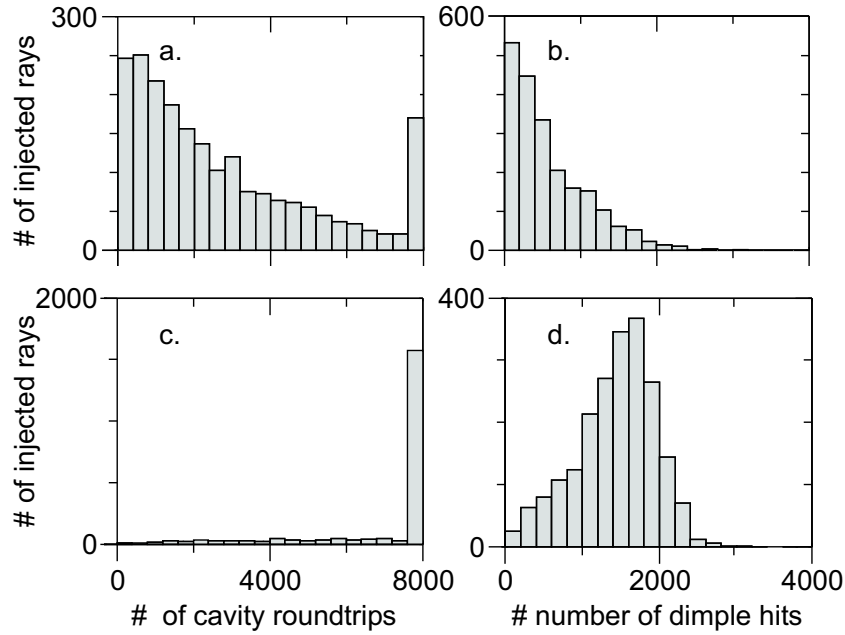

Figure 9.4: *Ray-tracing statistics for a configuration II-resonator at the cavity lengths $L = 1$ mm (upper figures) and $L = 0.5$ mm (lower figures). The probability distributions show the number of rays (out of 2091) vs. the number of round-trips before escaping (a) and (c) and vs. the number of dimple hits (b) and (d).*

9.4   The experimental setup

The two mirrors forming the cavity are mounted in stable top-actuated mounts (New Focus 9774 and 9775). A tunable Titanium Sapphire ring laser (Coherent 899-01), which is driven by a diode-pumped laser (Coherent Verdi) and operates at a wavelength of $\lambda = 800$ nm, is used to inject our cavity. A lens ($f = 10$ cm) in front of the cavity mode-matches the input beam to the lowest-order mode of the cavity. The cavity length is scanned with a piezo-element to obtain the transmission spectrum. Besides the spectral information also the intensity profile on the back-mirror is monitored with a CCD-camera behind the cavity.

For accurate tuning of the *relative* cavity length one mirror is placed on a translation stage (PI M-521). The *absolute* cavity length is found by using frequency-degenerate points of the stable cavity (see Chapter 5). These special points can be recognized easily, both spectrally and in the intensity profile on the mirror, as follows. At these N-fold frequency-degenerate points, spectral resonances overlap and form N clumps of modes, each spaced at $\Delta v_{FSR}/N$, where Δv_{FSR} is the free spectral range. Furthermore, for off-axis injection at an angle N spots appear in the intensity profile on the mirror. As every N-fold frequency-degenerate point belongs to a unique cavity length (for the given radii of curvature of the mirrors), the absolute cavity length can be determined very accurately, up to a few μm.

9.5   Fabry-Perot spectra

9.5.1   Coupling the inner and outer cavity

Coupling of the inner and the outer cavity is needed to reinject light into the unstable inner cavity, where chaos can develop. To check if coupling is feasible, we operate a configuration I-cavity in the transition from a stable to an unstable inner cavity and measure its transmission spectra. We operate the cavity around a length of $L = 14$ mm, where both inner and outer cavity are close to 2-fold frequency-degeneracy ($N \sim 2$). The injected beam is mode-matched to and injected in the fundamental mode of the inner cavity.

We start out with a cavity length slightly shorter than $L = 14$ mm, where the inner cavity is thus still dominantly stable. The spectrum at this position, shown in Fig. 9.5a, contains a small bias and some sharp resonances. The sharp resonances represent stable modes living in the inner cavity. This is confirmed by the intensity profile on the mirror where the power is dominantly localized on the dimple. The bias in the spectrum indicates the onset of the unstable regime.

Figures 9.5b-d show how the spectrum changes if we increase the cavity length such that the inner cavity becomes unstable. Let us discuss this sequence.

The first remark is that the closer we get to instability of the inner cavity the lower becomes the number of sharp resonances in the spectrum. We can explain this as higher order modes become unstable first and only the lower order modes remain.

A second remark concerns the two broad "clumps" per free spectral range, which become more pronounced the closer we come to instability. This is a clear demonstration of the increased coupling to the outer cavity. The two clumps actually consist out of many modes in the almost frequency-degenerate ($N = 2$) outer cavity; the even ($n + m$)-modes are located in one clump and the odd modes in the other.
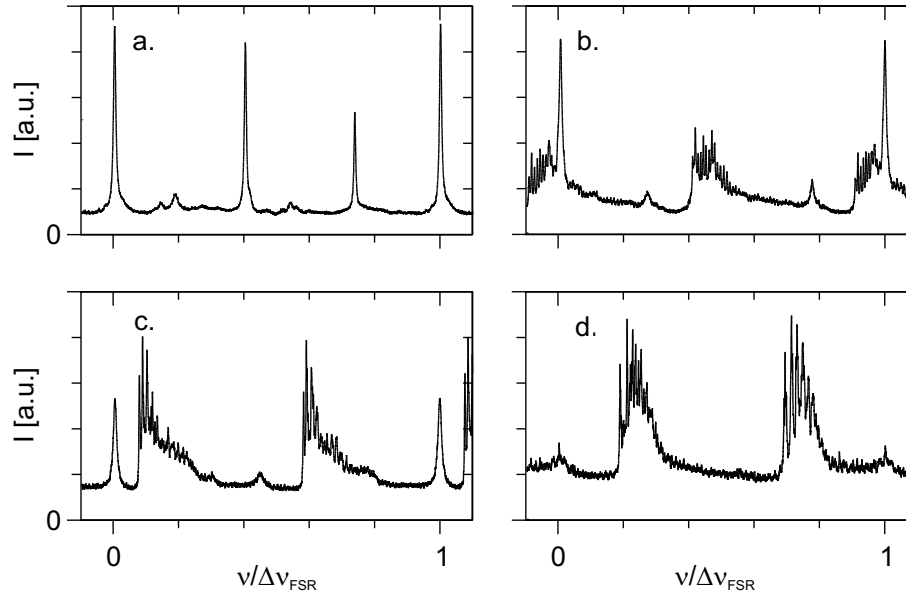
89

Figure 9.5: *Spectra in the transition from a stable to an unstable inner configuration II-cavity. In figure (a) the cavity is operated at L = 14 mm. The cavity length is increased stepwise in consecutive figures to: (b) ΔL = 0.11 mm, (c) ΔL = 0.24 mm and (d) ΔL = 0.4 mm.*

As a third remark, we want to stress that the bias becomes more dominant for a more unstable inner cavity. The bias indicates the presence of many spectrally broad modes, which can no longer be resolved. The origin of this spectral broadening could lie in the fact that these modes presumably encounter more losses, possibly due to the physical transition from the convex to the concave part of the mirror. On the other hand, this does not seem very likely as interferograms indicate that the transition is smooth. Another reason might be that the phases acquired by light in the inner and outer cavity are different so that they interfere destructively when they recombine.

At $L = 14.4$ mm, we are clearly in the regime where we inject in the inner cavity and couple to the outer cavity, since we dominantly excite modes in the outer cavity. This is confirmed by the intensity distribution on the mirror, which is now no longer localized on the dimple but also spread over the outer cavity. We conclude that we are able to couple the inner with the outer cavity, but are unable to spectrally resolve the excited modes.

9.5.2 Cavity finesse, average throughput and the number of hit points

It takes time for chaos to develop and a sufficient number of hits on the mirror, especially on the dimple, is needed. The number of hit points on the mirror can be deduced from the cavity finesse. However, as shown in the previous Section, for some configurations the resonances in the spectrum cannot be resolved and the number of hit points still remains unknown. Especially for this regime, we introduce here a new method to derive the *average*

number of hit points from the "spectrally-averaged" throughput. To test this method, we will first determine the number of hit points of an uncoupled *inner* resonator. Next, we will study an uncoupled *outer* cavity of which the spectral resonances can be resolved. Finally, the new method will be applied to a resonator of which the inner and outer cavity are coupled and the resonances cannot be resolved. The first experiment is performed on a configuration I-cavity, whereas the second and third experiment are performed on a configuration II-cavity.

In the first experiment, we inject a stable inner resonator with a beam mode-matched to the lowest order mode. The configuration I-cavity is operated at a cavity length $L = 13$ mm. The intensity profiles of the modes on the dimple are nice Hermite-Gaussian-modes, as expected for a stable resonator. During alignment of the cavity, the finesse was found to be very sensitive to the exact injection on and alignment of the mirrors. This we also observed in Chapter 7 and is possibly caused by the periodic structure of the roughness on the surface of the substrate. After optimizing the injection, a cavity finesse $F = 670$ is found. This makes the number of hit points on each mirror $F/2\pi = 107$.

In the second experiment, we consider an uncoupled stable outer cavity. We operate a configuration II-cavity at a cavity length $L = 6.6$ mm, which is close to the 4-fold frequency-degenerate point ($N \sim 4$). Off-axis injection at a proper angle excites a corkscrew-like ring-mode, which does not hit the dimple, but retraces its path in the outer cavity. These ring-modes (in the outer cavity) have a finesse of $F = 650$, making the number of hit points on each mirror $F/2\pi = 105$. All resonances can be resolved and have the same spectral width, which indicates that the modes experience identical losses.

We use this second spectrum to demonstrate the validity of our alternative method (see also Section 2.3) to determine the number of hit points. The measured average spectral throughput through one mirror (= average power in a FSR divided by the transmitted power behind first mirror) is 9.4 %. The rest of the light is transmitted by the opposite mirror (~ 10 %) or scattered out of the resonator (~ 80 %). We also know that for every hit on a mirror only 8×10^{-4} of the incident power is transmitted. It thus takes on average $9.4 \times 10^{-2}/8 \times 10^{-4} = 120$ hits per mirror before the light has leaked out. As this is comparable to the value $F/2\pi = 105$ obtained earlier, we conclude that the spectrally-averaged throughput provides us with the correct number of hit points and forms an alternative method for the number of hit points deduced from the cavity finesse.

To demonstrate that this new method can be of great benefit in situations where not all spectral resonances can be resolved, we perform a third experiment. We now inject light in a resonator with an unstable inner cavity, for which we chose a configuration II-cavity operated at a cavity length $L = 6.6$ mm. The unstable inner cavity magnifies the input beam and spreads the light over the outer cavity. The inner and outer cavity are now coupled but not all trajectories experience identical losses. This is reflected in the spectrum, which shows an offset, where the resonances cannot be resolved, and on top of that some sharp resolvable resonances. The highest measured cavity finesse of a sharp resonance is $F = 400$, suggesting that the number of hit points on each mirror is $F/2\pi = 65$ (for these modes). Application of our alternative method also reveals information about the modes in the spectral offset, which cannot be resolved in the spectrum. From the measured average spectral throughput of 1.1 %, we deduce an average number of hit points on a single mirror of only $1.1 \times 10^{-2}/8 \times 10^{-4} = 14$. The "average" mode thus hits the mirror a factor $4 - 5$ times less than the modes of which we can measure the cavity finesse directly. This shows once more that the various modes

91

experience different losses in a coupled resonator.

In the light of chaos, not only the number of hit points on the outer mirror but also the number of hits on the dimple is important. The ratio between the two is linked to the Gouy phase θ_0 of the outer cavity. The relation between the (integer) number of round-trips N (equivalent to the number of hit points on one mirror before the ray retraces its tracks) and the Gouy phase is given by $N = 2\pi/\theta_0$. For the above configuration the Gouy phase is $\theta_0 = 1.14$, and thus not a true fraction of 2π, but, naively speaking, the number of hit points on one mirror before the ray comes close to its initial position is $2\pi/\theta_0 \approx 5-6$. So if a ray is bounced out of the inner cavity into the outer cavity it takes roughly $5-6$ mirror hits before the ray is again injected into the inner cavity. For a total number of hit points of typically 14, the dimple will be hit only $2-3$ times.

We conclude by stating that our new method, based on a measurement of the average spectral throughput, reveals important information about the number of hit points for modes that cannot be spectrally resolved. We find that the average number of hit points on the mirror in the regime where the inner and outer cavity are coupled is typically only 14. The number of hit points on the dimple is even smaller ($2-3$ hits), and is very likely too small for chaos to develop.

9.5.3 Position of the injection beam

To check the influence of the position of the injection beam on the cavity dynamics we inject on various (off-axis) positions in one transverse plane. We did so for both a stable and an unstable inner cavity, and monitored both the spectrum and the intensity distribution on the back mirror.

Unstable inner cavity

We operate the configuration II-cavity at a cavity length $L = 2$ mm, for which the outer cavity is close to an 8-fold frequency-degenerate point ($N = 8$) and the inner cavity is unstable. For injection in the outer cavity at $\Delta x = 0.56$ mm relative to the mirror center, 8 clumps of modes are observed in the spectrum shown in Fig. 9.6a. The origin of these clumps lies in the fact that the spectrum is dominated by the frequency-degenerate outer cavity ($N = 8$). On the mirror, we indeed observe an ellipse of bright hit points in the outer cavity, bypassing the convex inner part. As the modes are degenerate, individual modes within each clump cannot be spectrally resolved and the cavity finesse cannot be determined. However, from the average spectral throughput we can deduce that the average number of hit points on one mirror for a typical mode is 70.

When we inject closer to the dimple, at $\Delta x = 0.38$ mm, we observe an elliptic ring-structure around the dimple. Fig. 9.6b shows the spectrum in which we still observe 8 clumps of modes, but the clumps are now broader and contain more structure. In each clump there is one sharp dominant resonance on the right side and many more modes with roughly identical peak transmission. The dimple clearly influences the modes in the outer cavity and partly breaks the degeneracy of the modes. The finesse of the sharp resonances is still $F = 670$, and the number of hit points on the mirror for this mode is thus $F/2\pi = 107$. The number of
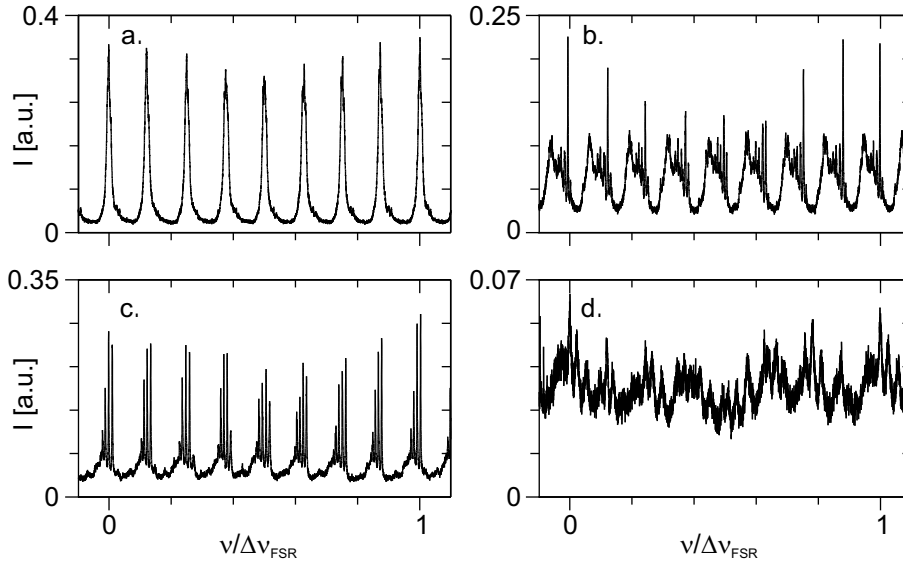
Figure 9.6: *Spectra for various positions of injection into a configuration II-cavity. The resonator is operated at a cavity length of $L = 2$ mm, where the inner cavity is unstable. The outer cavity is close to 8-fold frequency-degeneracy. The outer cavity is injected (a) $\Delta x = 0.56$ mm from the center of the mirror, (b) $\Delta x = 0.38$ mm, (c) $\Delta x = 0.30$ mm, and (d) $\Delta x = 0$ mm, respectively.*

mirror hits found from the average spectral throughput is 60. The discrepancy between these two numbers shows that some modes are more lossy than others.

Injection at $\Delta x = 0.30$ mm from the center of the mirror shows again a ring-structure around the dimple. Groups of modes are still observed in the spectrum Fig. 9.6c. In each clump we can now easily distinguish $4 - 6$ equally spaced modes. Taking a closer look at some of these resonances we observe a splitting of the modes. This might indicate that also other resonances are still degenerate and consists out of more modes. The finesse of such sharp resonances is $F = 620$, and the number of hit points on the mirror for these modes is thus $F/2\pi = 100$. The average number of hits on the mirror derived from the spectrally-average throughput is 50.

For on-axis injection of the inner cavity, at $\Delta x = 0$, the intensity distribution on the mirror shows that light is spread over both the inner and outer resonator, with a darker fringe in between. We observe an offset in the spectrum (Fig. 9.6d) with some finer structure on top of it. Most excited modes can not be resolved. The few sharp resonances in the spectrum that can be resolve yield $F/2\pi \approx 50$. The average number of hit points, found from the average transmitted power in the spectrum, is 28. As we are close to an 8-fold frequency-degeneracy, the number of hit points N in the outer cavity needed before a ray is reinjected into the inner cavity is $N = 8$. For a total number of hit points on the mirror of 28, the dimple is hit only $3 - 4$ times.

In summary, we have observed that already for injection at $\Delta x = 0.38$ mm away from the center of the cavity the influence of the inner cavity is felt; the losses increase and the

frequency-degeneracy in the spectrum is broken. As soon as a dominant part of the injected light hits the unstable inner cavity, resonances in the spectra are hard to resolve, which makes it difficult to deduce information from the spectrum. The number of dimple hits is again $3 - 4$.

Stable inner cavity

Next, the influence of the position of injection on the cavity dynamics is investigated for a cavity with both a stable inner and outer cavity. The configuration I-cavity is operated at a cavity length of $L = 12$ mm, where the inner cavity is close to a 4-fold frequency-degeneracy ($N = 4$).

First, we inject just outside the dimple and observe two bright spots on the left and right side of the dimple and a vague background. The spectrum for this position of injection (Fig. 9.7a) shows an offset and on top of that a quasi-periodic structure (~ 20-fold). When we inject on the dimple (Fig. 9.7b), the offset in the spectrum has disappeared and instead we observe 4 clumps of resonances in the spectrum, which indicate the 4-fold frequency-degeneracy of the inner cavity. The intensity profile on the mirror is indeed localized on the dimple and the light is thus confined to the stable inner resonator.

Injection on the other side of the dimple results in a spectrum with an offset and on top of that a 7-fold periodic structure, see Fig. 9.7c. On the mirror, we now observe 12 hit points on the concave part of the mirror and some hit points on the convex part, which cannot be pinpointed exactly, due to a limited imaging resolution. This intensity information (> 12 hit points) combined with the 7-fold structure in the spectrum indicates that the number of longitudinal round-trips that are needed before the ray returns on itself equals $N = 14$ [21]. This means that there must be $(14 - 12) = 2$ hits on the convex part of the mirror. The number of transverse "round-trips" K the orbit makes before closing cannot be deduced directly from our experimental observations. We know, however, that K should be an even integer to comply with the 7-fold spectral structure. A calculation of the overall Gouy phase $\theta_{\text{overall}} = 2\pi K/N$ sheds more light on this problem.

The overall Gouy phase depends on the number of hits on the inner and outer part of the bifocal mirror and is the weighted sum of the Gouy phase of the inner and outer cavity, which is in our case $\theta_{\text{overall}} = \theta_{\text{in}}/7 + (6\theta_{\text{out}})/7$. The Gouy phase of the inner cavity is roughly $\theta_{\text{in}} = 2\pi/4 = 1.57$, whereas the Gouy phase of the outer cavity $\theta_{\text{out}} = 2.95$ for the corresponding cavity length. This results in an overall Gouy phase $\theta_{\text{overall}} = 2.75$. The calculated overall Gouy phase should thus be equal to $2\pi K/14$, which means that $K = 6$.

The existence of this $K/N = 6/14$-point is surprising. For a cavity without dimple and a specific cavity length, one Gouy phase determines all cavity dynamics and $K/N = 6/14$ and $K/N = 3/7$ describe identical physics. The description of frequency-degenerate points in a bifocal cavity is, however, more complicated. For one specific Gouy phase (*e.g.*, $\theta_0 = 2\pi 3/7$), the sequence of hit points on both cavities can be different, which is expressed by $K/N = 6/14$ and $K/N = 3/7$. It is important to note that the orbit described by $K/N = 6/14$ cannot be described by two $K/N = 3/7$-orbits.

We conclude that for a coupled stable inner and outer cavity, an offset appears in the spectrum filled with modes that cannot be resolved. Also for coupled stable cavities, frequency-degenerate points exist, but the Gouy phase does not uniquely define the trajectory.
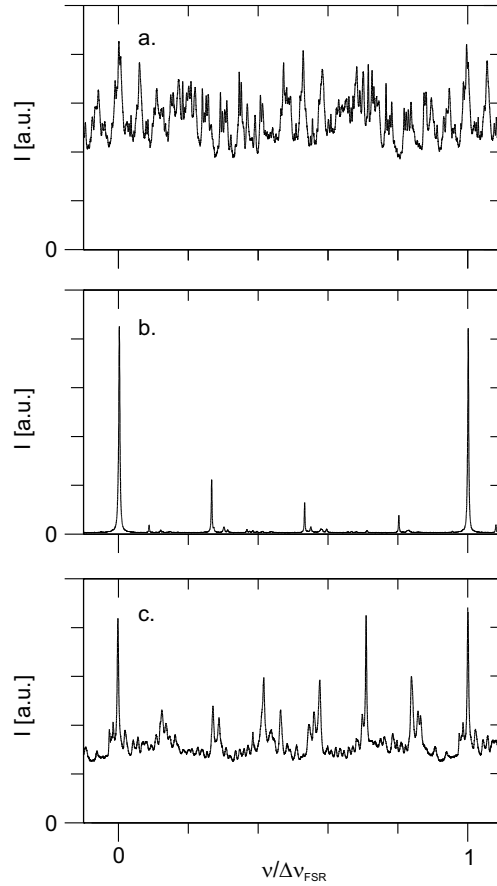
Figure 9.7: *Spectra for various positions of injection of a configuration I-cavity. The cavity is operated at a cavity length of L = 12 mm, where the stable inner cavity is close to 4-fold frequency-degeneracy. The position of injection as compared to the mirror center Δx is for (a) Δx = −0.12 mm, (b) Δx = 0 mm, and (c) ΔL = 0.17 mm, respectively. Note the (quasi-periodic) structure in both (a) and (c), where the rays hit both the inner and outer cavity.*

9.6 Transmission patterns

9.6.1 Speckle patterns

Important information can also be obtained from the transmission profiles. When we inject the unstable inner cavity, the light spreads out over the convex and concave part of the bifocal mirror. Close to frequency-degeneracy of the outer cavity, circular structures dominate the speckled pattern as shown in Fig. 9.8a. These circular structures are the Hercher fringes introduced in Chapter 4. We will concentrate, however, on the nondegenerate case as shown in Fig. 9.8b. The patterns can be observed best for fixed cavity length, *i.e.*, when the scanning
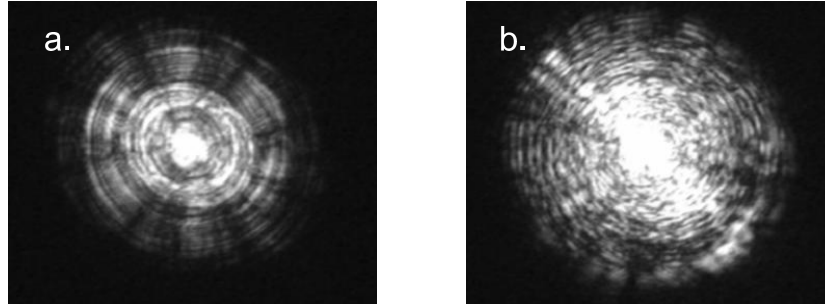
of the cavity length is stopped.

Figure 9.8: *Intensity profiles on the mirror of a configuration I-cavity for a fixed cavity length (no scanning) (a) operated at L = 14.3 mm, where the outer cavity is close to 2-fold frequency-degeneracy (N ≈ 2) and (b) away from a frequency-degenerate point at L = 17.3 mm. Close to frequency-degeneracy Hercher-fringes dominate the speckle pattern.*

We encounter the speckled patterns not only for short cavity lengths, but also for the longer ones. On first sight, the patterns appear to be random, but a closer look shows rotational symmetry. Such intensity profiles with a rotational symmetry were also observed for a similar, but uncoupled system, introduced in Chapter 8. We have demonstrated there that Laguerre-Gaussian (LG) eigenmodes form the natural basis of the uncoupled system. Similar speckled patterns were observed and associated with a (coupled) superposition of many excited LG-modes. The patterns in the coupled system, presented in this Chapter, have the same flavor.

The randomness and structure of the speckles in the patterns imply that many unperturbed LG-modes are involved. The speckle size or, equivalently, the spatial period can be attributed to the highest-order mode m involved. The connection between mode number m involved and the size of the speckles Λ_m is $m = (4w/\Lambda_m)^2$ [12] with w the waist of the fundamental mode. The typical size (FWHM) or correlation length of a speckle in the pattern is measured to be $20 - 50$ μm. For $w = 40$ μm we thus find that the highest-order mode involved has a mode number $m = 10$ to 60.

A polarizer behind the resonator gives more insight into the speckle patterns. The transmission axis parallel to the input polarization results in a typical speckle pattern as shown in Fig. 9.9a. We observe again some rotational symmetry in the patterns. Rotation of the output polarizer over $90°$ (transmission axis perpendicular to the input polarization) shows, to our surprise, that light is still transmitted through the polarizer. Obviously, the resonator changes the polarization of the light and acts as a depolarizer. Fig. 9.9b, with crossed polarizers, is different from Fig. 9.9a; the light is spread more homogeneously over the mirror and structure of the speckles is more grainy.

The difference in intensity distributions for both polarizations can be analyzed more quantitatively by averaging over many intensity realizations in a free spectral range. The comparison is then easier as we are less sensitive to vibrations that change the cavity length on a
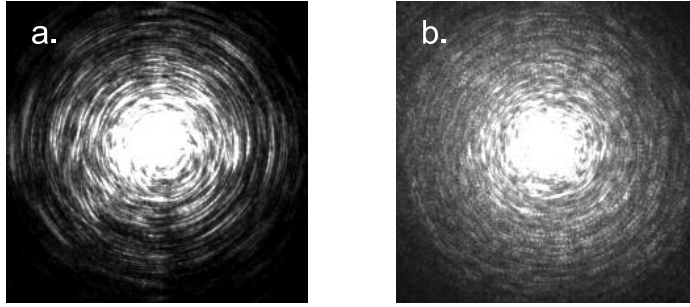
Figure 9.9: *Intensity profiles on the mirror behind a polarizer with its transmission axis (a) parallel and (b) perpendicular to the input polarization. The configuration II-cavity is operated in between two frequency-degenerate points at a cavity length $L = 1.8$ mm. The images correspond to an area of 1×1 mm^2 on the composite mirror. The dimple is overexposed.*

sub-wavelength scale over time. Disadvantage of this method is that the speckles are averaged out and that we loose intensity information on smaller length scales. We achieve the averaging by scanning the resonator with a piezo over a few wavelengths. Cross-sections of these averaged intensity patterns are shown in Fig. 9.10. The intensity is highest in the center of the dimple, where we inject, and decreases closer to the edges of the mirror. This decrease is strongest for the parallel case. The distribution for polarization perpendicular to the input polarization is more uniform. The ratio of these two polarized intensities decreases from 200 in the center to ~ 70 at $\rho = 0.5$ mm. 2D-images of the intensity distributions show that the total (area-integrated) transmitted power is 75 times stronger for the polarization parallel to the input polarization than for the perpendicular polarization. This ratio is also found from the spectra of both polarizations.

9.7 Discussion and recommendations

In this Chapter, we have presented a preliminary experimental investigation of a novel type of open optical resonator. This resonator has been shown to be able to couple the inner and outer cavity. The number of hit points in the inner (unstable) cavity was found to be limited to typically only $3 - 4$. For chaos to develop in our 3D-cavity more hits are probably needed.

Rays that remain solely within either the stable inner or outer cavity were observed to do so during about $60 - 110$ round-trips. This number is large enough to distinguish individual modes in the optical spectrum. In the coupled regime, where chaos might develop, the number of hit points, however, decreases drastically and resonances in the spectrum become hard to resolve. This makes it difficult to perform the statistics that is needed to show the presence of chaos in our experiment. The reason for the observed broadening might be that light in the inner and outer cavity acquire a different phase and interferes destructively.

Our first recommendation concerns the coupling of the inner and the outer cavity, which is up to now relatively modest. For coupled systems, it is obvious that the phase plays a
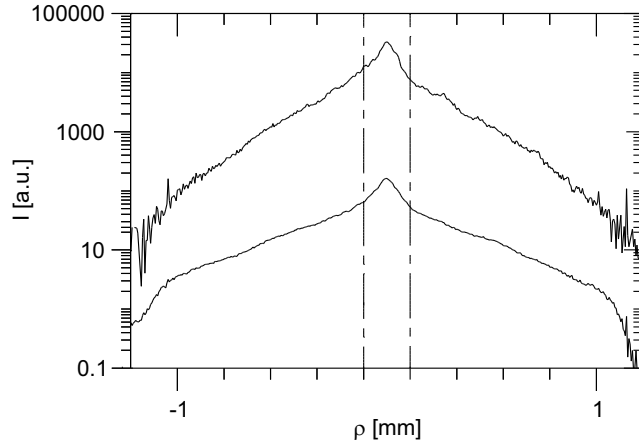
Figure 9.10: *Cross-sections of intensity profiles averaged over many realizations in a free spectral range. The upper and lower curve represent the intensity distributions observed behind a polarizer oriented parallel and perpendicular to the input polarization, respectively. The configuration II-cavity is operated at a length of L = 1.8 mm. The two dotted-dashed lines indicate the position of the dimple, ρ ranging from -0.1 to 0.1 mm.*

crucial role [12]. As our system is a coupled transverse *multi*-mode system, many phases are involved. To adapt the phase of the inner cavity to the outer cavity, we propose a bifocal mirror of which the dimple can be axially displaced on a sub-wavelength scale. Proper matching of the optical phases in the inner and outer cavity might increase the coupling between the two cavities.

Our second recommendation concerns the presence of corkscrew-like (ring)modes that live solely in the outer cavity. Although these modes do not contribute to chaos, they are still present in the spectrum and make it harder to resolve individual resonances. An azimuthal obscuration inside the outer cavity will block these ring-modes much more than the wanted 2D-modes that hit the dimple and contribute to chaos. With such an obscuration, the spectrum should contain less resonances but relatively more resonances that might demonstrate chaotic behavior. The proposed obscuration will also break the rotation symmetry of our cavity; a symmetry that could frustrate some types of chaos.

9.8   Acknowledgement

Bibliography

[1] J. M. Vaughan, *The Fabry-Perot interferometer* (Adam Hilger, Bristol, 1989).

[2] A. O'Keefe and D. A. G. Deacon, 'Cavity ring-down optical spectrometer for absorption measurements using pulsed laser sources', Rev. Sci. Instrum **59**, 2544–2551 (1988).

[3] G. Berden, R. Peeters, and G. Meijer, 'Cavity ring-down spectroscopy: Experimental schemes and applications', Int. Rev. Phys. Chem **19**, 565–607 (2000).

[4] S. Haroche and D. Kleppner, 'Cavity quantum electrodynamics', Phys. Today **42**, 24–30 (1989).

[5] D. W. Vernooy, A. Furusawa, N. P. Georgiades, V. S. Ilchenko, and H. J. Kimble, 'Cavity QED with high-Q whispering gallery modes', Phys. Rev. A **57**, R2293 (1998).

[6] D. K. Armani, T. J. Kippenberg, S. M. Spillane, and K. J. Vahala, 'Ultra-high-Q toroid microcavity on a chip', Nature **421**, 925 (2003).

[7] http://www.ligo.caltech.edu.

[8] http://www.cascina.virgo.infn.it.

[9] http://tamago.mtk.nao.ac.jp.

[10] D. Kleckner, W. Marshall, M. J. A. de Dood, K. N. Dinyari, B. J. Pors, W. T. M. Irvine, and D. Bouwmeester, 'High finesse opto-mechanical cavity with a movable thirty-micron-size mirror', Phys. Rev. Lett. **96**, 173091 (2006).

[11] W. Demtröder, *Laser-spektroskopie* (Springer-Verlag, Berlin, 1993).

[12] A. E. Siegman, *Lasers* (University Science Books, Sausalito, CA, 1986).

[13] E. D. Palik, H. Boukari, and R. W. Gammon, 'Experimental study of the effect of surface defects on the finesse and contrast of a Fabry-Perot interferometer', Appl. Opt. **35**, 38–50 (1996).

[14] M. Born and E. Wolf, *Principles of Optics* (Cambridge University Press, Cambridge, 1999).

[15] M. Bernardini, S. Braccini, C. Bradaschia, G. Cella, E. Cuoco, E. D'Ambrosio, V. Dattilo, R. de Salvo, A. di Virgilio, F. Fidecaro, A. Gaddi, A. Gennai, A. Giassi, A. Giazotto, P. L. Penna, M. Lyablin, G. Losurdo, M. Maggiore, S. Mancini, H. B. Pan, A. Pasqualetti, D. Passuello, R. Poggiani, P. Popolizio, D. Shabalin, A. Viceré, and

Z. Zhang, 'Plane parallel mirrors Fabry-Perot cavity to improve Virgo superattenuators', Phys. Rev. A **243**, 187–194 (1998).

[16] G. Rempe, R. J. Thompson, H. J. Kimble, and R. Lalezari, 'Measurement of ultralow losses in an optical interferometer', Opt. Lett **17**, 363–365 (1992).

[17] M. Hercher, 'Spherical mirror Fabry-Perot interferometer', Appl. Opt. **7**, 951–966 (1968).

[18] J. M. Bennet and L. Mattsson, *Introduction to Surface Roughness and Scattering* (Optical Society of America, Washington, D. C., 1999).

[19] M. Hercher, 'The spherical Fabry-Perot interferometer', in 'The Fabry-Perot Interferometer', (J. M. Vaughan, ed.), 184–212 (Adam Hilger, Bristol, 1989).

[20] D. J. Bradley and C. J. Mitchell, 'Comments on the spherical mirror Fabry-Perot interferometer', Appl. Opt **8**, 707–709 (1969).

[21] D. R. Herriot, H. Kogelnik, and R. Kompfner, 'Off-axis paths in spherical mirror interferometers', Appl. Opt. **3**, 523–526 (1964).

[22] C. J. Hood, H. J. Kimble, and J. Ye, 'Characterization of high-finesse mirrors: Loss, phase shifts, and mode structure in an optical cavity', Phys. Rev. A **64**, 033804 (2001).

[23] K. D. Skeldon, J. Mackintosh, M. von Gradowski, S. Thieux, and R. Lee, 'Qualification of supermirrors for ring-laser-gyros based on surface roughness and scatter measurements', J. Opt. Soc. Am. A **3**, 183–187 (2001).

[24] N. Uehara and K. Ueda, 'Accurate measurement of ultralow loss in a high-finesse Fabry-Perot-interferometer using the frequency-response functions', Appl. Phys. B **61**, 9–15 (1995).

[25] R. Mavaddat, D. E. McClelland, P. Hellos, and J. Y. Vinest, 'Dual recycling laser interferometer gravitational-wave detectors simulating the performance with imperfect mirrors', J. Opt. **26**, 145–149 (1995).

[26] S. Sato, S. Miyoki, M. Ohashi, M. K. Fujimoto, T. Yamazaki, M. Fukushima, A. Ueda, K. Ueda, K. Watanabe, K. Nakamura, K. Etoh, N. Kitajima, K. Ito, and I. Kataoka, 'Loss factors of mirrors for a gravitational wave antenna', Appl. Opt. **38**, 2880–2885 (1999).

[27] D. G. Blair, M. Notcutt, C. T. Taylor, E. K. Wong, C. Walsh, A. Leistner, J. Seckold, J. M. Mackowski, P. Ganau, C. Michel, and L. Pinard, 'Development of low-loss sapphire mirrors', Appl. Opt. **36**, 337–341 (1997).

[28] N. Uehara, A. Ueda, and K. Ueda, 'Ultralow-loss mirror of the parts-in-10^6 level at 1064 nm', Opt. Lett. **20**, 530–532 (1995).

[29] J. C. Stover, *Optical Scattering: Measurement and Analysis* (SPIE, Bellingham, 1995).

[30] E. L. Church, 'Fractal surface finish', Appl. Opt. **27**, 1518–1526 (1988).

[31] TNO Science and Industry, Business Unit Opto-Mechanical Instrumentation (OMI), Delft, The Netherlands.

[32] S. Jakobs, A. Duparre, and H. Truckenbrodt, 'Interfacial roughness and related scatter in ultraviolet optical coatings: experimental approach', Appl. Opt. **37**, 1180–1193 (1998).

[33] W. M. Bruno, J. A. Roth, P. E. Burke, W. B. Hewitt, R. E. Holmbeck, and D. G. Neal, 'Prediction of the bidirectional reflectance-distribution function from atomic-force and scanning-tunneling microscope measurements of interfacial roughness', Appl. Opt. **34**, 1229–1238 (1995).

[34] J. M. Elson, J. P. Rahn, and J. M. Bennett, 'Light-scattering from multilayer optics: comparison of theory and experiment', Appl. Opt. **19**, 669–679 (1980).

[35] J. Poirson, F. Breetanker, M. Vallet, and A. le Floch, 'Analytical and experimental study of ringing effects in a Fabry-Perot cavity. Application to the measurement of high finesses', J. Opt. Soc. Am. B **14**, 2811–2817 (1997).

[36] P. Domokos and H. Ritsch, 'Mechanical effects of light in optical resonators', J. Opt. Soc. Am. B **20**, 1098–1130 (2003).

[37] D. J. Heinzen, J. J. Childs, J. E. Thomas, and M. S. Feld, 'Enhanced and inhibited visible spontaneous emission by atoms in a confocal resonator', Phys. Rev. Lett. **58**, 1320–1323 (1987).

[38] J. C. Bergquist, W. M. Itano, and D. J. Wineland, 'Laser stabilization to a single ion', in 'Frontiers in Laser Spectroscopy', (T. W. Hänsch and M. Inguscio, eds.), 359–376 (North-Holland Publishing Co, Amsterdam, 1994).

[39] J. T. Hodges, J. P. Looney, and R. D. van Zee, 'Response of a ring-down cavity to an arbitrary excitation', J. Chem. Phys. **105**, 10278–10288 (1996).

[40] D. H. Lee, Y. Yoon, B. Kim, J. Y. Lee, Y. S. Yoo, and J. W. Hahn, 'Optimization of the mode matching in pulsed cavity ring-down spectroscopy by monitoring non-degenerate transverse mode beating', Appl. Phys. B **74**, 435–440 (2002).

[41] C. A. Schrama, D. Bouwmeester, G. Nienhuis, and J. P. Woerdman, 'Mode-dynamics in optical cavities', Phys. Rev. A **51**, 641–645 (1995).

[42] H. J. Stöckmann, *Quantum chaos, an introduction* (Cambridge University Press, Cambridge, 1999).

[43] E. Hecht, *Optics* (Addison Wesley, San Francisco, 2002).

[44] F. L. Pedrotti and L. S. Pedrotti, *Introduction to Optics* (Prentice Hall, New Jersey, 1993).

[45] D. J. Bradley and C. J. Mitchell, 'Characteristics of the defocused spherical Fabry-Perot interferometer as a quasi-linear dispersion instrument for high resolution spectroscopy of pulsed laser sources', Phil. Trans. A **263**, 209–223 (1968).

[46] I. A. Ramsay and J. J. Degnan, 'A ray analysis of optical resonators formed by two spherical mirrors', Appl. Opt. **9**, 385–398 (1970).

[47] J. A. Arnaud, 'Degenerate optical cavities. III: Effect of aberrations', Appl. Opt. **9**, 1192–1200 (1970).

[48] E. Merzbacher, *Quantum Mechanics* (John Wiley & Sons, New York, 1970).

[49] D. Herriot, H. Kogelnik, and R. Kompfer, 'Folded optical delay lines', Appl. Opt. **3**, 523–526 (1964).

[50] T. Klaassen, J. de Jong, M. P. van Exter, and J. P. Woerdman, 'Transverse mode coupling in an optical resonator', Opt. Lett. **30**, 1959–1961 (2005).

[51] P. Harihan, 'Interferometers', in 'Handbook of Optics', (M. Bass, ed.), 21.1 – 21.8 (McGraw-Hill, New-York, 1995).

[52] M. Françon, *Optical Interferometry* (Academic Press, New York, 1966).

[53] S. Tolansky, *An Introduction to Interferometry* (Longmans, Green and Co, London, 1955).

[54] B. Kells, 'LIGO-Caltech', Private communication.

[55] J. Dingjan, E. Altewischer, M. P. van Exter, and J. P. Woerdman, 'Experimental observation of wave chaos in a conventional optical resonator', Phys. Rev. Lett. **88**, 064101 (2002).

[56] N. Uehara and K. Ueda, 'Accurate measurement of the radius of curvature of a concave mirror and the power dependence in a high-finesse Fabry-Perot interferometer', Appl. Opt. **34**, 5611–5619 (1995).

[57] H. Laabs and A. T. Friberg, 'Nonparaxial eigenmodes of stable resonators', IEEE J. Quant. Elec. **35**, 198–207 (1999).

[58] H. A. Buchdahl, *An Introduction to Hamiltonian Optics* (Cambridge University Press, Cambridge, 1970).

[59] V. N. Mahajan, *Optical Imaging and Aberrations* (SPIE Press, Bellingham, 1998).

[60] D. L. Dickensheets, 'Imaging performance of off-axis planar diffractive lenses', J. Opt. Soc. Am. A **13**, 1849–1858 (1996).

[61] M. H. Dunn and A. I. Ferguson, 'Coma compensation in off-axis laser resonators', Opt. Comm. **20**, 214–219 (1977).

[62] J. Visser and G. Nienhuis, 'Spectrum of an optical resonator with spherical aberration', J. Opt. Soc. Am. A **22**, 2490–2497 (2005).

[63] J. Dingjan, *Multi-mode optical resonators and wave chaos*, Ph.D. thesis, Universiteit Leiden (1996).

[64] G. Nienhuis, 'Huygens Laboratorium, Universtiteit Leiden, The Netherlands', Private communication.

[65] M. Lax, W. H. Louisell, and W. B. McKnight, 'From Maxwell to paraxial wave optics', Phys. Rev. A **11**, 1365–1370 (1975).

[66] A. Wünsche, 'Transition from the paraxial approximation to exact solutions of the wave equation and application to Gaussian beams', J. Opt. Soc. Am. A **9**, 765–774 (1992).

[67] G. M. Sanger, 'Perspective on precision machining, polishing and optical requirements', in 'Contemporary methods of optical fabrication', volume 306, 46–51 (SPIE, San Diego, 1981).

[68] E. R. Marsh, B. P. John, J. A. Couey, J. Wang, R. D. Grejda, and R. R. Vallance, 'Predicting surface figure in diamond turned calcium fluoride using in-process force measurement', J. Vac. Sc. and Techn. B **23**, 84–89 (2005).

[69] Philips Research, Eindhoven, The Netherlands.

[70] J. W. Yan, K. Syoji, and J. Tamaki, 'Crystallographic effects in micro/nanomachining of single-crystal calcium fluoride', J. Vac. Sc. and Techn. B **22**, 46–51 (2004).

[71] LASEROPTIK, Garbsen, Germany.

[72] M. V. Berry, 'Quantal phase factors accompanying adiabatic changes', Proc. R. Soc. London A **392**, 54–57 (1984).

[73] J. Anandan, J. Christian, and K. Wanelik, 'Order Resource Letter GPP-1: Geometric phases in physics', Am. J. of Phys. **65**, 180–185 (1997).

[74] N. Hodgson and H. Weber, *Optical Resonators* (Springer, New York, 1997).

[75] A. W. Snyder and J. D. Love, *Optical Waveguide Theory* (Chapman and Hall, London, 1983).

[76] C. Degen, I. Fischer, and W. Elsäßer, 'Transverse modes in oxide confined VCSELs: Influence of pump profile, spatial hole burning, and thermal effects', Opt. Lett. **5**, 38–47 (1999).

[77] C. Degen, I. Fischer, W. Elsäßer, L. Fratta, P. Debernardi, G. P. Bava, M. Brunner, R. Hövel, M. Moser, and K. Gulden, 'Transverse modes in thermally detuned oxide-confined vertical-cavity surface-emitting lasers', Phys. Rev. A **63**, 023817 (2001).

[78] A. Yariv, *Quantum electronics* (John Wiley and Sons, New York, 1988), third edition.

[79] A. Aiello, M. P. van Exter, and J. P. Woerdman, 'Ray chaos in optical cavities based upon standard laser mirrors', Phys. Rev. E **68**, 046208 (2003).

[80] M. Abramowitz and I. Stegun, *Handbook of Mathematical Functions* (Dover, New York, 1974).

[81] N. J. van Druten, S. S. R. Oemrawsingh, Y. Lien, C. Serrat, M. P. van Exter, and J. P. Woerdman, 'Observation of transverse modes in a microchip laser with combined gain and index guiding', J. Opt. Soc. Am. B **18**, 1793–1804 (2001).

[82] G. R. Hadley, 'Effective-index model for vertical-cavity surface-emitting lasers', Opt. Lett. **20**, 1483–1485 (1995).

[83] C. Serrat, M. P. van Exter, N. J. van Druten, and J. P. Woerdman, 'Transverse mode formation in microlasers by combined gain- and index-guiding', IEEE J. Quant. Elec. **35**, 1314–1321 (1999).

[84] W. H. Press, S. A. Teukolsky, W. T. Vetterling, and B. P. Flannery, *Numerical Recipes* (Cambridge University Press, Cambridge, 1987).

[85] G. R. Fowles and G. L. Cassiday, *Analytical Mechanics* (Thomson Learning, Belmont, USA, 1999), sixt edition.

[86] J. D. Jackson, *Classical Electrodynamics* (Wiley, New York, 1998).

[87] S. B. Shaklan, 'Selective mode injection and observation for few-mode fiberoptics', Appl. Opt. **30**, 4379–4383 (1991).

[88] E. G. Neumann, *Single-mode fibers* (Springer-Verlag, Berlin, 1988).

[89] G. P. Agrawal, *Nonlinear fiber optics* (Academic Press, San Diego, 1989).

[90] J. T. Verdeyen, *Laser Electronics* (Prentice Hall, Upper Saddle River, New Jersey, 2000), third edition.

[91] H. J. Stöckmann and J. Stein, '"Quantum" chaos in billiards studied by microwave absorption', Phys. Rev. Lett. **64**, 2215 (1990).

[92] D. L. Kaufman, I. Kosztin, and K. Schulten, 'Expansion method for stationary states of quantum billiards', Am. J. of Phys. **67**, 133–141 (1999).

[93] B. W. Li, M. Robnik, and B. Hu, 'Relevance of chaos in numerical solutions of quantum billiards', Phys. Rev. E **57**, 4095–4105 (1998).

[94] F. Haake, *Quantum Signatures of Chaos* (Springer, Berlin, 1991).

[95] A. Aiello, unpublished.

[96] M. Bennett, M. F. Schatz, H. Rockwood, and K. Wiesenfeld, 'Huygens' clocks', Proc. Roy. Soc. A **458**, 563–579 (2002).

[97] R. J. C. Spreeuw, R. C. Neelen, N. J. van Druten, E. R. Eliel, and J. P. Woerdman, 'Mode coupling in a He-Ne ring laser with backscattering', Phys. Rev. A **42**, 43154324 (1990).

[98] P. Pellandini, R. P. Stanley, R. Houdré, U. Oesterle, M. Ilegems, and C. Weisbuch, 'Dual-wavelength laser emission from a coupled semiconductor microcavity', Appl. Phys. Lett. **71**, 864–866 (1997).

104

Samenvatting

In deze samenvatting wordt het idee van dit proefschrift uitgelegd zodanig dat het ook te begrijpen is voor mensen die minder ingevoerd zijn in de Natuurkunde. De titel van dit proefschrift luidt 'Imperfecte Fabry-Perot resonatoren'. Om het onderwerp van dit proefschrift te kunnen begrijpen, zal de titel stapsgewijs ontleed en uitgelegd worden. In paragraaf S.1 wordt de werking van een resonator verklaard. Een resonator of trilholte is een 'holte' waarin een golf kan 'trillen' en daarbij vanwege de opsluiting wordt versterkt. Om dit zo duidelijk mogelijk uit te leggen, maken we een vergelijking met geluid, voordat we ons richten op licht. In paragraaf S.2 zullen we ons beperken tot licht en de werking en de toepassing van de optische Fabry-Perot resonator nader uit de doeken doen. De verschillende soorten optische resonatoren worden geïntroduceerd in paragraaf S.3. Vervolgens maken we de stap van ideale resonatoren, d.w.z. resonatoren met perfecte spiegels, naar niet-ideale resonatoren. In paragraaf S.4 worden deze afwijkingen van de ideale spiegel en de consequenties voor een resonator besproken. Deze afwijkingen vormen de rode draad door dit proefschrift. In paragraaf S.5 wordt het begrip chaos verklaard en in paragraaf S.6 wordt de weerslag van mijn onderzoek besproken.

S.1   De resonator

Het woord 'resoneren' komt uit het Latijn en is opgebouwd uit de woorden *re* en *sonare*. Het betekent zoveel als 'terug geluid geven' of 'herklinken'. Je zou het ook vrij kunnen vertalen met 'meetrillen'. Een glas gaat niet alleen meetrillen als je er tegen aan tikt, maar ook als je luid genoeg op de juiste toonhoogte zingt. Het glas kan zelfs zo hard mee gaan trillen dat het stuk gaat. Ook als soldaten *in* de pas lopen kunnen resonanties optreden. Dit is de reden dat soldaten *uit* de pas gaan lopen als ze over een brug heen gaan. Anders kan de brug zo erg mee gaan trillen (dus resoneren), dat ze het kan begeven. In contrast met deze wat destructieve voorbeelden wordt resonantie ook in de praktijk gebruikt in sommige apparaten en instrumenten. Deze bevatten dan een aparte ruimte, ook wel 'resonator' genoemd, om de

resonanties te stimuleren en te controleren. Je kunt hierbij denken aan de klankkast van een gitaar, een orgelpijp of de box van de luidspreker.

Voordat we de vraag kunnen beantwoorden wanneer iets resoneert, moeten we iets meer weten over de eigenschappen van licht en geluid. Zowel licht als geluid zijn golven die zich voortbewegen. Een belangrijke eigenschap van een golf is, zoals aangegeven in figuur. S.1, de lengte van één periode, ook wel genaamd de golflengte. In de akoestiek bepaalt de golflengte de *toonhoogte*; hoge tonen hebben een kortere golflengte dan lage tonen. Dit is de reden dat een korte orgelpijp veel hogere tonen produceert dan een langere orgelpijp. In de optica bepaalt de golflengte de *kleur* van het licht. Blauw licht heeft een kortere golflengte dan rood licht. Behalve dat licht een trilling van een elektromagnetisch veld is, terwijl geluid een trilling is van de lucht, is er ook een belangrijk verschil in de golflengtes. Geluid heeft een golflengte in de orde van centimeters tot meters, terwijl licht een golflengte heeft van een fractie van een micrometer, een miljoenste deel van een meter. De golflengte van licht is hiermee ongeveer 100 keer kleiner dan de dikte van een mensenhaar!
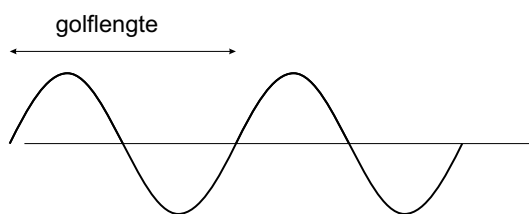

Figuur S.1: *Licht en geluid bestaan uit golven die zich voortbewegen. Typerend voor een golf is de lengte van één periode, ook wel genaamd de golflengte.*

Met deze kennis kunnen we de vraag beantwoorden wanneer licht of geluid in een resonator resoneert. Dit gebeurt als de halve golflengte, of een geheel aantal halve golflengtes, precies past in de resonator en dus gelijk is aan de lengte van de resonator. In het geval van een snaar is de halve golflengte dus gelijk aan de lengte van de snaar. Een golf beweegt zich voort en reflecteert (draait om) aan het einde van de snaar. Als de gereflecteerde golf precies hetzelfde is als de nieuwe golf aan het begin van de snaar (de golven 'passen' in de resonator) noemen we dit ook wel constructieve interferentie. Alle golven met dezelfde golflengte versterken elkaar. Dit is schematisch weergegeven in figuur S.2a. Als de golflengte niet past dan zullen meerdere golven elkaar uitdoven. Dit heet ook wel destructieve interferentie en is weergegeven in figuur S.2b.

We laten de vergelijking met de akoestiek nu definitief achter ons en richten ons op de resonantie van licht. Een optische resonator of Fabry-Perot resonator bestaat uit twee spiegels die parallel tegenover elkaar staan. Een voorbeeld hiervan is te zien in figuur S.3. Licht tussen de spiegels, aangegeven met een M, reflecteert elke keer als het één van de spiegels raakt en loopt dus heen en weer. Het licht wordt een tijdje opgeslagen. Deze resonator is vernoemd naar de heren Fabry en Perot, die deze resonator voor het eerst bouwden in 1899.

We weten ondertussen dat één bepaalde kleur licht resoneert, oftewel constructief interfereert, als één halve golflengte (of een geheel aantal halve golflengtes) gelijk is aan de afstand tussen de spiegels. Is dit niet het geval, dan treedt destructieve interferentie op en dooft het licht in de trilholte uit. Als we nu wit licht, dat bestaat uit alle kleuren, een resonator insturen,

106

a.   b.
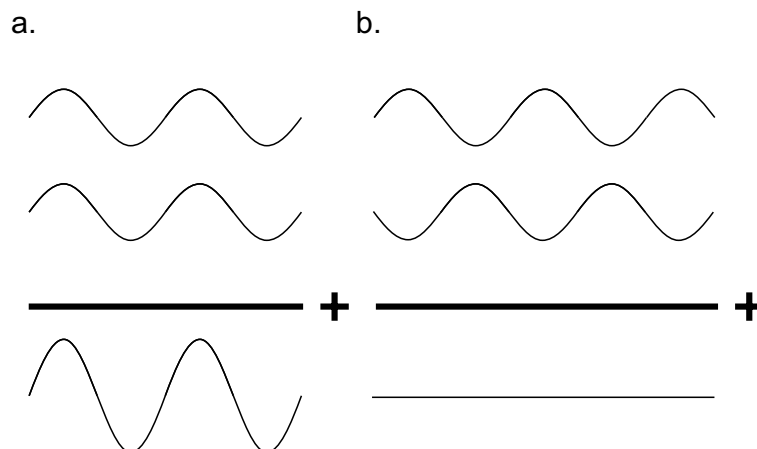
Figuur S.2: *Schematische weergave van interferentie, waarbij golven elkaar kunnen versterken of uitdoven. In figuur a zijn de twee golven niet verschoven ten opzichte van elkaar. Als twee golven elkaar tegenkomen mogen we ze optellen. Het resultaat is een golf met dezelfde golflengte maar met een twee keer zo grote uitwijking. De twee golven versterken elkaar dus, dit heet ook wel constructieve interferentie. In figuur b zijn de twee golven ten opzichte van elkaar geschoven zodat de pieken van de ene golf samenvallen met de dalen van de ander. Als deze golven elkaar tegenkomen en we tellen ze weer bij elkaar op dan doven ze elkaar uit. Dit heet ook wel destructieve interferentie.*

M   M

L
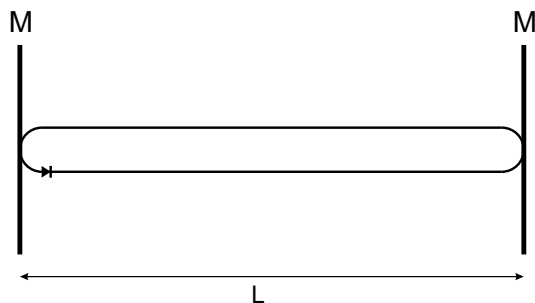
Figuur S.3: *Schematische weergave van een Fabry-Perot resonator, bestaande uit twee vlakke spiegels. De spiegels zijn aangeduid met een M en staan op een afstand L van elkaar. Doordat de spiegels reflecteren loopt het licht rond door de resonator en wordt het tijdelijk opgeslagen.*

zullen bepaalde kleuren (= specifieke golflengtes) precies passen in de resonator en andere niet. De kleuren die passen, overleven terwijl de andere kleuren uitdoven. Een resonator werkt dus als een filter voor de verschillende kleuren licht.

Bij resonantie van geluid kunnen we ons waarschijnlijk meer voorstellen, maar ook de resonantie van licht kennen we van nabij. Denk bijvoorbeeld aan een dun olielaagje op een plas water of anders een zeepbel. We zien in reflectie allerlei kleuren in de zeepbel of het olielaagje. We zien alleen die kleuren waarvoor geldt dat de dikte van het olielaagje of het zeepsop gelijk is aan een geheel aantal halve golflengtes. De andere kleuren passen niet precies en doven wederom uit. Eigenlijk zijn zowel het olielaagje als de zeepbel simpele voorbeelden van een optische resonator. Een belangrijk verschil met de resonatoren gebruikt in dit onderzoek is dat onze spiegels veel beter reflecteren dan de laagjes olie of zeepsop. Het laagje zeepsop reflecteert ongeveer 2 % van het invallende licht, terwijl een goede spiegel meer dan 99 % van het licht reflecteert. Het licht wordt tussen onze twee spiegels dus veel langer opgeslagen.

S.2   Werking van de optische resonator

De reden dat de optische resonator zoveel wordt gebruikt in experimenten en toepassingen ligt in zijn vermogen om kleuren te scheiden. Twee verschillende kleuren, bijvoorbeeld geel en oranje, die een golflengteverschil van 0.02 micrometer hebben, kun je makkelijk met het blote oog onderscheiden. Een optische resonator met goed reflecterende spiegels kan veel kleinere kleurverschillen zichtbaar maken, tot wel één miljoenste deel van een micrometer!

Hoe werkt dit precies? Een hoog kleurscheidend vermogen ontstaat doordat de resonator één specifieke golflengte doorlaat, maar golflengtes die een klein beetje langer of korter zijn niet. Hoe langer het licht rond loopt in de resonator, hoe kleiner het golflengtebereik dat doorgelaten wordt en des te groter dus het kleurscheidend vermogen (kleinere kleurverschillen kunnen zichtbaar gemaakt worden).

Om dit goed te kunnen begrijpen doen we een experiment. We beschijnen een optische resonator met twee verschillende kleuren licht, die bijna dezelfde golflengte hebben. Eén van beide golflengtes past precies in de resonator en de andere golflengte is net een beetje te lang om goed te passen. We kijken nu wat er gebeurt met beide golven na respectievelijk één, vijf en twintig rondgangen ten opzichte van de golf net na injectie. De verschuiving van de golf na een aantal rondgangen ten opzichte van de golf net na injectie, bepaalt of beide golven constructief of destructief interfereren (zie figuur S.2). We beginnen met de golflengte die precies past, zoals afgebeeld in figuur S.4a. We zien dat na één, vijf en twintig keer rondgaan door de resonator, de golf niet verplaatst ten opzichte van de golf net na injectie. We kunnen de golf net na injectie en de golf na twintig keer rondgaan dan ook optellen zoals we dat gedaan hebben in figuur S.2a. Het licht zal zichzelf dus versterken en constructief interfereren.

Nu bekijken we het licht dat een golflengte heeft dat net een beetje te lang is om te passen in de resonator. Dit is getekend in figuur S.4b. We zien dat hoe langer het licht rondloopt des te meer de golf verschuift ten opzichte van de golf vlak na injectie (de golf net na injectie is gestippeld). Na vijf rondgangen is de golf een klein beetje verschoven ten opzichte van de golf vlak na injectie. Het licht is echter zo weinig verschoven dat het nog
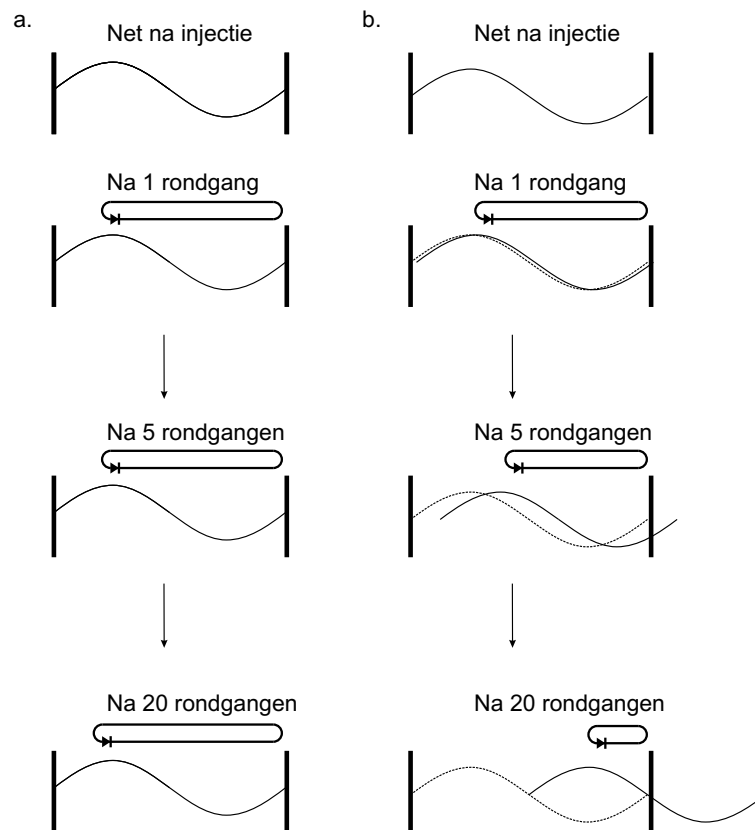
Figuur S.4: *Het kleurscheidend vermogen van een resonator is gebaseerd op het aantal keren dat het licht rondloopt tussen de spiegels. In figuur a (linker kolom) bekijken we licht dat precies past in de resonator. Ongeacht het aantal rondgangen blijft de golf op de dezelfde plek terugkomen, zodat het licht altijd constructief interfereert met zichzelf. In figuur b (rechter kolom) bekijken we licht met een golflengte die net niet past in de resonator. Na vijf rondgangen is het licht een klein beetje verschoven (doorgetrokken lijn) in vergelijking met het licht net na injectie (gestippelde lijn). Het licht zal echter nog steeds constructief interfereren. Na twintig rondgangen is het licht echter wel zoveel verschoven (doorgetrokken lijn) dat het destructief interfereert met zichzelf. Het licht zal uitdoven.*

steeds behoorlijk goed constructief interfereert. Na twintig rondgangen is het licht echter wel zo veel verschoven dat de pieken van de golf samenvallen met de dalen van de golf vlak na injectie. Deze situatie is ook weergegeven in figuur S.2b. De twee golven zullen elkaar dus uitdoven oftewel destructieve interferentie treedt op.

We hebben nu gezien dat licht dat precies past, constructief met zichzelf interfereert ongeacht het aantal rondgangen. Licht dat echter net niet past, interfereert een aantal rondgangen nog constructief, maar naarmate het aantal rondgangen toeneemt interfereert het destructief. Hiermee hebben we laten zien dat het kleurscheidend vermogen toeneemt met het aantal rondgangen. Het kleurscheidend vermogen wordt dus beter naarmate de reflectiviteit van de spiegels in de optische resonator toeneemt en het aantal rondgangen tussen de spiegels groter wordt. Dit is precies de reden dat het kleurscheidend vermogen van de resonator gebruikt in dit onderzoek veel beter is dan die van zeepsop of een olielaagje.

S.3 Stabiele en instabiele resonatoren

Nu we weten hoe een resonator werkt gaan we ook kijken welke soorten resonatoren bestaan. Je kunt ze indelen in twee groepen; de stabiele en de instabiele resonatoren. De stabiele resonator, afgebeeld in figuur S.5a, bestaat uit twee *holle* spiegels. Een lichtstraal die naar buiten loopt wordt door de vorm van de spiegel terug naar het midden geduwd. De instabiele resonator, afgebeeld in figuur S.5b, bestaat uit twee *bolle* spiegels. Een lichtstraal die naar buiten loopt wordt door de vorm van de spiegels alleen maar verder naar buiten geduwd. Lichtstralen in een instabiele resonator zullen de spiegels maar een paar keer raken voordat ze uit de resonator verdwijnen. Een instabiele resonator wordt dan ook gekenmerkt door zijn hoge verliezen. We zullen verderop in dit hoofdstuk dieper ingaan op de toepassing van de stabiele en instabiele resonator in dit onderzoek.
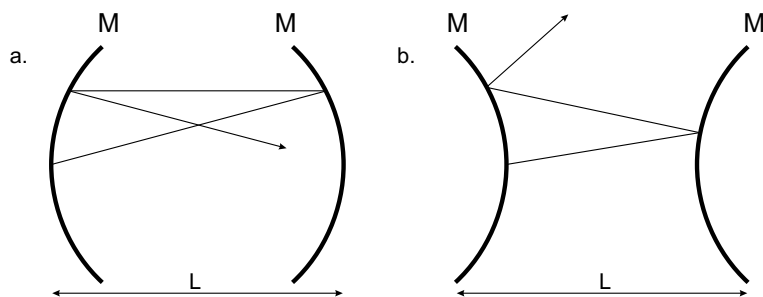

Figuur S.5: *Twee typen resonatoren: In figuur a zien we de stabiele resonator bestaande uit twee holle spiegels. Licht dat naar buiten loopt wordt door de vorm van de spiegels naar binnen geduwd. In figuur b zien we de instabiele resonator bestaande uit twee bolle spiegels. Licht dat naar buiten loopt zal alleen maar verder naar buiten worden geduwd. Dit type resonator vertoont dan ook veel verliezen.*

S.4 Spiegel imperfecties

Tot nu toe zijn we uitgegaan van ideale spiegels. Dit is in werkelijkheid niet het geval. Spiegels vertonen imperfecties op verschillende lengteschalen. De eerste soort imperfectie die we hier bespreken is 'oppervlakte ruwheid'. Dit zijn kleine hobbeltjes en putjes aan het oppervlak van de spiegel, die ontstaan tijdens het maken. De diameter van deze hobbeltjes en putjes is voor een gemiddelde spiegel $1 - 10$ micrometer en de hoogte is ca. 0.005 micrometer. Ook al is dit hoogteverschil zeer klein, het is toch een honderdste deel van een optische golflengte. Dit betekent dat op de positie van zo'n hobbeltje de resonator een heel klein beetje korter is. Als het licht vaak genoeg rondgaat, interfereert het licht niet meer constructief. Dit betekent dat het kleurscheidend vermogen van de resonator vermindert. Verder wordt het licht een beetje verstrooid als het een bolletje of een putje raakt. Dit veroorzaakt extra verliezen, die het kleurscheidend vermogen eveneens verslechteren.

De tweede soort imperfecties zijn de zogeheten 'aberraties'. Dit zijn afwijkingen van de ideale ruwe vorm van een spiegel. Een spiegel met een ideale vorm laat alle lichtstralen door één punt gaan, zoals te zien in figuur S.6a. Dit betekent dat een voorwerp scherp wordt afgebeeld. Afwijkingen van de ideale vorm van een spiegel zorgen ervoor dat lichtstralen die verder naar buiten toe op de spiegel vallen op een andere positie worden afgebeeld dan lichtstralen die meer naar binnen op de spiegel vallen. Dit is weergegeven in figuur S.6b. Het niet samenvallen van deze lichtstralen veroorzaakt bij afbeelding onscherpte. Afwijkingen van de ideale vorm ontstaan doordat een spiegel in het productieproces een sferische vorm krijgt, dus de vorm van een deel van een bol. Deze vorm wordt echter toch vaak gebruikt omdat die makkelijk te vervaardigen is.
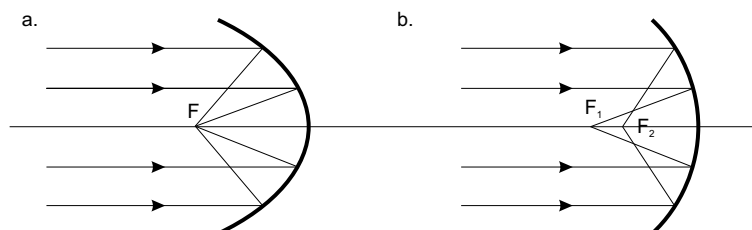
Figuur S.6: *Demonstratie van het begrip aberratie. De spiegel in figuur a heeft een ideale vorm. Deze vorm heet ook wel 'parabolisch'. De parabolische spiegel zorgt ervoor dat de verschillende evenwijdige lichtstralen netjes in het punt F samenkomen. Dit betekent dat een voorwerp (buiten de tekening) scherp wordt afgebeeld. In figuur b zien we een spiegel zoals die ook gebruikt wordt in optische resonatoren. De vorm van zo'n spiegel heet ook wel 'sferisch'. Lichtstralen die de spiegel meer aan de buitenkant raken, komen na reflectie dichter bij de spiegel bij elkaar (punt F_2) dan lichtstralen die de spiegel meer in het midden raken. Deze komen samen in een punt verder van de spiegel (punt F_1). Dit heeft tot gevolg dat als je iets afbeeldt met een sferisch spiegel het beeld een beetje uitgesmeerd wordt en daardoor onscherp is.*

S.5   Chaos

We hebben al een heleboel basiskennis, maar we moeten nog één ding weten voordat verklaard kan worden wat het initiële doel van deze promotie was, namelijk: "Wat is chaos?" Chaos associëren we vaak met een toestand van ongeordendheid, wanorde of zelfs ordeloosheid. In de Natuurkunde is dit maar ten dele waar en spreken we liever over deterministische chaos. Om dit begrip duidelijk te maken gaan we biljarten. Ons biljart lijkt op een café-biljart. Het enige verschil is dat de bal veel vaker rond moeten kunnen gaan dan in een café-biljart mogelijk is. We nemen daarom een laken waarop de ballen nauwelijks afremmen.

We beginnen ons experiment met een rechthoekige biljarttafel. Zo'n biljart is een voorbeeld van een niet-chaotisch systeem. Het spel dat we spelen gaat als volgt: We stoten een bal af in een bepaalde richting en houden bij hoe de bal over het biljart rolt. Als de eerste bal is uitgerold, stoten we een tweede bal vanaf dezelfde startpositie, onder een net iets andere hoek. Wederom houden we bij hoe de bal over de tafel loopt.

We herhalen deze stoot-experimenten met een ander (aangepast) biljart, waarbij we een cirkelvormig stuk uit de hoek van eenzelfde rechthoekig biljart hebben gezaagd. De vorm van dit aangepaste biljart is wel chaotisch en is te zien in figuur S.7b. Vervolgens vergelijken we de resultaten in het niet-chaotische en het chaotische biljart. Het verschil tussen de twee afgelegde paden in het niet-chaotisch biljart ontwikkelt zich maar langzaam. Na drie keer de band raken is het verschil in paden nog erg beperkt, zoals te zien is een figuur S.7a. Als we nu kijken naar het verschil van de paden in het chaotische biljart zien we dat de twee ballen, zodra ze het bolle stuk hebben geraakt, een heel andere kant opgaan. Het kleine verschil bij het aanstoten heeft al zeer drastische gevolgen na drie ketsen.

Deze gevoeligheid voor de begincondities is hét kenmerk van chaotische systemen. Identieke begincondities leveren weliswaar precies hetzelfde eindresultaat op, maar een kleine afwijking aan het begin levert een totaal ander resultaat op.
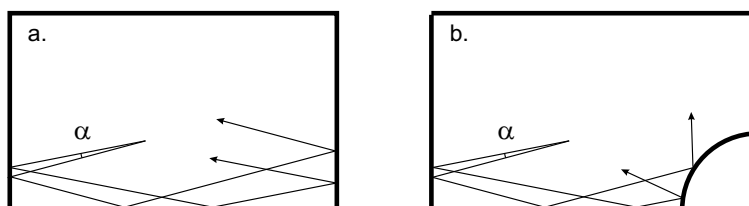

Figuur S.7: *Demonstratie van het verschil tussen een niet-chaotisch (figuur a) en een chaotisch biljart (figuur b). In het biljart zijn twee paden afgebeeld van biljartballen die met een klein verschil in hoek (hoek α) zijn afgestoten. Na een aantal keer de band geraakt te hebben, zijn de twee paden in het niet-chaotische biljart nog bijna hetzelfde. In het chaotische biljart daarentegen is dit niet het geval. De twee paden van de twee gespeelde ballen gaan een heel andere kant op nadat het bolle stuk is geraakt. Het kleine verschil bij het aanstoten in een chaotisch biljart heeft dus grote gevolgen voor het verdere verloop van de ballen.*

Om chaos experimenteel te kunnen laten zien, moet je aan twee voorwaarden voldoen. Ten eerste heb je een systeem nodig dat exponentieel gevoelig is, oftewel een systeem waarin een kleine verandering aan het begin sterk toeneemt. En ten tweede heeft chaos tijd nodig

om zich te kunnen ontwikkelen en moet de verblijftijd in het systeem voldoende zijn.

S.6   Dit proefschrift

We gaan terug naar onze optische resonator en denken weer even aan de twee hoofdgroepen van resonatoren; de stabiele en de instabiele resonator. De instabiele resonator zorgt ervoor dat twee lichtstralen die op bijna dezelfde positie invallen op de spiegel een heel andere kant op gaan. Een instabiele resonator is dus zeer gevoelig voor een kleine verandering aan het begin. Nadeel is echter dat het licht maar heel kort opgeslagen blijft. Dit is niet het geval in een stabiele resonator, waarin het licht heel lang opgeslagen kan blijven. Een combinatie van een instabiele en een stabiele resonator lijkt dus een systeem op te leveren dat aan beide voorwaarden voor chaos voldoet. Zo'n systeem is weergegeven in figuur S.8.
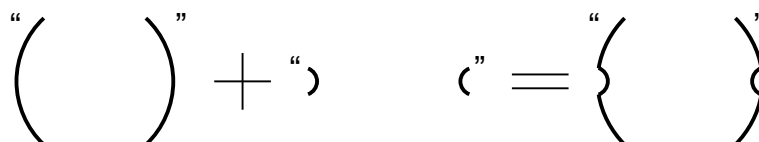
Figuur S.8: *Schematische weergave van een chaotische resonator opgebouwd uit een stabiele resonator aan de buitenkant en een instabiele resonator in het midden. Het instabiele deel zorgt voor de exponentiële gevoeligheid voor de begincondities en de stabiele buitenkant zorgt ervoor dat chaos voldoende tijd krijgt om zich te ontwikkelen.*

Het uitgangspunt van deze promotie was dan ook het systeem dat bestaat uit een combinatie van beide resonatoren. De benodigde spiegels hebben echter een vorm die niet makkelijk te maken is. Het heeft dan ook lang geduurd om het juiste materiaal en de juiste productiemethode te vinden, die niet enkel de juiste vorm van de spiegel opleverde, maar ook een voldoende lage oppervlakte-ruwheid had.

De combinatie van een stabiele en een instabiele resonator is niet veel bestudeerd. Als je gaat meten, kunnen er ten gevolge van spiegel imperfecties dus allerlei effecten optreden die niets met chaos te maken hebben. We hebben er dan ook voor gekozen eerst het gedrag van imperfecties in een stabiele resonator te bestuderen.

Het effect van ruwheid en aberraties op de resonanties van een optische resonator is bestudeerd in de hoofdstukken 2-6. In deze hoofdstukken is ook gemeten hoe lang het licht opgeslagen blijft in de resonator. Dit is vergeleken met het ideale geval, waarbij enkel de reflectiviteit van de spiegels wordt meegenomen en de imperfecties van de spiegels worden verwaarloosd. De gemeten verblijftijd van het licht in de experimentele resonator is natuurlijk korter dan in het ideale geval. Het verschil in de gemeten en de ideale tijd is een goede maat om de imperfecties te kunnen karakteriseren.

Tijdens het doen van de metingen, zoals beschreven in de eerste vier hoofdstukken, zijn we bezig geweest om, samen met een aantal bedrijven, de speciale hoogreflecterende spiegels te maken uit figuur S.8. Dit bleek lastiger dan gedacht en het lukte eigenlijk pas een jaar geleden. Het onderzoek dat gedaan is aan resonatoren met deze speciale spiegels is beschreven in de hoofdstukken 7-9. Chaos hebben we niet direct kunnen aantonen, maar wel een boel spannende fysica.

List of Publications

- T. Klaassen, A. Hoogeboom, M. P. van Exter, and J. P. Woerdman, *Gouy phase of non-paraxial eigenmodes in a folded resonator*, J. Opt. Soc. Am. A **21**, 1689-1693 (2004).

- T. Klaassen, J. de Jong, M. P. van Exter, and J. P. Woerdman, *Transverse mode coupling in an optical resonator*, Opt. Lett. **30**, 1959-1961 (2005).

- T. Klaassen, A. Hoogeboom, M. P. van Exter, and J. P. Woerdman, *Resonant trapping of scattered light in a degenerate resonator*, Opt. Comm. **260**, 365-371 (2006).

- T. Klaassen, M. P. van Exter, and J. P. Woerdman, *Characterization of scattering in an optical resonator*, in preparation.

- T. Klaassen, M. P. van Exter, J. Visser, and G. Nienhuis, *Connection between wave and ray approach of cavity aberrations*, in preparation.

- T. Klaassen, M. P. van Exter, and J. P. Woerdman, *Characterization of diamond-machined mirrors*, in preparation.

Curriculum Vitae

van Thijs Klaassen, geboren te Grave op 3 mei 1978.

Ik heb in 1996 mijn VWO-diploma behaald op het Dominicus College te Nijmegen. Daarna ben ik Technische Natuurkunde gaan studeren in Delft. Na afronding van mijn propaedeuse en doctoraal I, heb ik gekozen voor de afstudeerrichting Optica in de gelijk-namige vakgroep, geleid door prof. dr. ir. J. J. M. Braat. Als invulling van mijn vakkenpakket heb ik drie maanden stage gelopen bij Océ Printing Systems in München. Hier werd mij duidelijk hoe leuk het is om zelfstandig onderzoek te doen. Ook mijn afstuderen heb ik in het bedrijfsleven gedaan en wel bij het Natuurkundig Laboratorium van Philips in Eindhoven. Het doel van mijn afstuderen was om een oplossing te vinden voor de (ongewenste) Moiré patronen die kunnen optreden bij het maken van foto's met een digitale camera. Op dit onderwerp ben ik in 2002 afgestudeerd bij prof. dr. H. P. Urbach. Naast mijn studie heb ik twee jaar Natuurkunde gedoceerd op het St.-Maartenscollege, een middelbare school in Voorburg.

Enthousiast geworden door het doen van onderzoek, ben ik in 2002 als onderzoeker in dienst getreden van de stichting Fundamenteel Onderzoek der Materie (FOM). Ik heb mijn onderzoek gedaan aan de Universiteit Leiden in de vakgroep "Quantum Optics & Quantum Information" onder leiding van prof. dr. J. P. Woerdman en begeleid door dr. M. P. van Exter. Het onderwerp betreft het chaotisch gedrag van licht in optische resonatoren. Dit proefschrift bevat de resultaten van dit onderzoek.

Mijn bijdrage aan het onderwijs bestond in mijn eerste jaar uit het verzorgen van het werkcollege bij het vak Quantum Mechanica II. De laatste drie jaren van mijn promotieon-derzoek ben ik werkcollege-assistent geweest bij het vak Optica. Daarnaast heb ik drie stu-denten begeleid in de verschillende fases van hun opleiding en de presentaties verzorgd voor potentiële natuurkunde studenten op de open dagen van de Universiteit Leiden.

Tijdens mijn promotieonderzoek ben ik twee jaar voorzitter geweest van de Centrale On-dernemingsraad (COR) van mijn werkgever FOM. De laatste jaren van mijn promotie ben ik actief geweest als bestuurslid van de Nederlandse Klim en Bergsport Vereniging (NKBV).

Nawoord

Een promotie doet veel mensen denken aan een lange en eenzame weg. De weg naar het proefschrift is inderdaad vier jaar lang, maar de momenten van eenzaamheid zijn met de steun en ondersteuning van mensen om mij heen tot een minimum beperkt gebleven. Een woord van dank aan degenen die hiervoor gezorgd hebben, is dan ook op zijn plaats.

Als eerste wil ik Koos Benning en Ewie de Kuiper bedanken. Hun vakmanschap heeft er altijd voor gezorgd dat mechanische problemen van korte duur waren. Woorden die hen typeren zijn precisie en maatwerk. Daarnaast wil ik hun collega's van de mechanische werkplaats bedanken voor de klussen tussendoor en de gezelligheid. Voor de broodnodige ondersteuning op het gebied van netwerk, computers en elektronica wil ik René Overgauw en Arno van Amersfoort bedanken. Zij stonden altijd voor me klaar en waren bereid hun grote expertise te delen.

Mijn collega's en de studenten, die meegeholpen hebben aan mijn onderzoek, bedank ik voor hun inbreng, de genoten gezelligheid en de vele discussies aan de koffietafel. In het bijzonder wil ik hierbij Erwin Altewischer, Jorrit Visser en Arthur Hoogeboom noemen. De laatste periode van mijn promotie heb ik als zeer stimulerend ervaren, mede dankzij de nieuwe mensen in de groep. Daarnaast waren de espresso's met Alexander Wirtz altijd een erg goed begin van de dag.

Buiten mijn werk ben ik eveneens een grote groep mensen erkentelijk. Voor de nodige afleiding en verbreding tijdens mijn promotie zorgde het voorzitterschap van de Centrale Ondernemingsraad (COR) van mijn werkgever, de stichting Fundamenteel Onderzoek der Materie (FOM). Ik bedank alle COR-leden voor de goede sfeer en het resultaat. In het bijzonder wil ik hierbij Leo Wiggers noemen voor het delen van zijn ervaring, inzicht en de vruchtbare samenwerking. Deze prettige samenwerking heb ik ook ervaren in het bestuur van de Nederlandse Klim en Bergsport Vereniging (NKBV). Ondanks de roerige periode die we hebben doorgemaakt, heb ik ook hier veel geleerd en een prettige tijd gehad.

Tenslotte wil ik de mensen bedanken die er simpelweg altijd voor mij zijn; mijn familie en vrienden. Met hen is het mogelijk om van alles en nog wat te ondernemen, mooie gesprekken te voeren of simpelweg biertjes te drinken. Een bijzondere plaats hierin heeft Joris de Boer.